

TECHNISCHE  
UNIVERSITÄT  
DRESDEN

---

# High Magnetic Field Properties of Fe - Pnictide Thin Films

Dissertation  
zur Erlangung des akademischen Grades  
Doktor der Naturwissenschaften  
Doktor rerum naturalium  
vorgelegt  
der Fakultät Mathematik und Naturwissenschaften  
der Technischen Universität Dresden

von

Fritz Kurth  
geboren am 26.05.1984 in Annaberg-Buchholz

Fakultät Mathematik und Naturwissenschaften  
Technische Universität Dresden  
Dresden 2015

Eingereicht am 13.07.2015

Verteidigt am 20.11.2015

1. Gutachter: Prof. Dr. Ludwig Schultz
2. Gutachter: Prof. Dr. Paul Seidel
3. Gutachter: Prof. Dr. Kazumasa Iida

# Abstract

The recent discovery of high-temperature superconductivity in Fe-based materials triggered worldwide efforts to investigate their fundamental properties. Despite a lot of similarities to cuprates and  $\text{MgB}_2$ , important differences like near isotropic behaviour in contrast to cuprates and the peculiar pairing symmetry of the order parameter (OP) have been reported. The OP symmetry of Fe-based superconductors (FBS) was theoretically predicted to be of so-called  $s_{\pm}$  state prior to various experimental works. Still, most of the experimental results favour the  $s_{\pm}$  scenario; however, definitive evidence has not yet been reported. Although no clear understanding of the superconducting mechanisms yet exists, potential applications such as high-field magnets and Josephson devices have been explored. Indeed, a lot of reports about FBS tapes, wires, and even SQUIDs have been published to this date.

In this thesis, the feasibility of high-field magnet applications of FBS is addressed by studying their transport properties, involving doped  $\text{BaFe}_2\text{As}_2$  (Ba-122) and  $\text{LnFeAs}(\text{O},\text{F})$  [ $\text{Ln}=\text{Sm}$  and  $\text{Nd}$ ]. Particularly, it is important to study physical properties in a sample form (i.e. thin films) that is close to the conditions found in applications. However, the realisation of epitaxial FBS thin films is not an easy undertaking. Recent success in growing epitaxial FBS thin films opens a new avenue to delve into transport critical current measurements. The information obtained through this research will be useful for exploring high-field magnet applications.

This thesis consists of 7 chapters:

Chapter 1 describes the motivation of this study, the basic background of superconductivity, and a brief summary of the thin film growth of FBS. Chapter 2 describes experimental methods employed in this study. Chapter 3 reports on the fabrication of Co-doped Ba-122 thin films on various substrates. Particular emphasis lies on the discovery of fluoride substrates to be beneficial for epitaxy without compromising superconducting properties. It is worth mentioning, that a world record  $T_c$  of 28 K for Co-doped Ba-122 thin films is reported here.

Chapter 4 describes high-field transport properties (up to dc 35 T) of epitaxial P-doped Ba-122 thin films prepared by MBE. Among the FBS, P-doped Ba-122 shows very high transport critical current densities, although the  $T_c$  is lower than for  $\text{LnFeAs}(\text{O},\text{F})$  [ $\text{Ln}=\text{Sm}$  and  $\text{Nd}$ ]. Additionally, the film is microstructurally clean. These high  $J_c$  values are due to a high vortex line energy.

Chapter 5 deals with transport properties of epitaxial  $\text{SmFeAs}(\text{O},\text{F})$  thin films. In the course of this work, a dc 45 T magnet has been used within collaboration with the Na-

tional High Magnetic Field Laboratory at Tallahassee, FL, USA. SmFeAs(O,F) thin films have been prepared by molecular beam epitaxy (MBE). The investigated film shows a very high transport critical current density ( $J_c$ ) of over  $10^5$  A/cm<sup>2</sup> at 45 T and 4.2 K for both main crystallographic directions, which features favourable for high-field magnet applications. Additionally, by investigating the pinning properties, a dimensional crossover between the superconducting coherence length and the FeAs interlayer distance at 30-40 K was observed.

Chapter 6 reports on high-field transport properties of NdFeAs(O,F) thin films prepared by MBE. In this case, the transition from Abrikosov to Josephson vortices was observed around 20-30 K. Additionally, the angular  $J_c$  data were scaled with the anisotropic Ginzburg-Landau approach. The obtained parameters at given temperature are observed to increase with decreasing temperature, which is different from Co-doped Ba-122. Chapter 7 summarises this work.

Die kürzliche Entdeckung von Hochtemperatur-Supraleitung in Fe-basierten Materialien löste weltweite Bemühungen aus, deren grundlegende Eigenschaften zu untersuchen. Neben vielen Gemeinsamkeiten mit den Kupraten und MgB<sub>2</sub> sind wichtige Unterschiede wie nahezu isotropes Verhalten (im Gegensatz zu den Kupraten) und eine auffällige Paarungssymmetrie des Ordnungsparameters (OP) berichtet worden. Die OP-Symmetrie der Fe-basierten Supraleiter (FBS) wurde theoretisch als  $s\pm$  berechnet, noch bevor experimentelle Versuche unternommen wurden. Derzeit favorisieren experimentelle Ergebnisse das  $s\pm$ -Szenario, dennoch gibt es noch keine definitiven Nachweise. Obwohl noch kein komplettes Verständnis des supraleitenden Mechanismus existiert, wurden schon potentielle Anwendungen wie Josephson-Elemente und Hochfeldmagnete erforscht. In der Tat erschienen zahlreiche Veröffentlichungen über supraleitende Kabel, Bänder und auch SQUIDs. Diese Arbeit befasst sich mit der Durchführbarkeit von Hochfeld-Anwendungen durch die Untersuchung der Transporteigenschaften von FBS, namentlich Ba-122 und  $LnFeAs(O,F)$  [ $Ln=Sm$  und  $Nd$ ]. Es ist von großer Wichtigkeit, die physikalischen Eigenschaften in einer Probenform zu untersuchen, die der Form in Anwendungen nahekommt (z.B. Dünnschichten), um dieselben Rahmenbedingungen vorgeben zu können. Es ist jedoch nicht einfach, epitaktische FBS Dünnschichten zu realisieren. Kürzlich gewonnene Erkenntnisse in der Herstellung von epitaktischen FBS-Dünnschichten ermöglichen nun ein tieferes Eindringen in die Transporteigenschaften. Die in diesen Untersuchungen gewonnenen Informationen stellen somit wichtige Argumente in der Diskussion um Hochfeld-Anwendungen dar. Diese Arbeit besteht aus sieben Kapiteln:



Kapitel 1 beinhaltet die Motivation dieser Arbeit, die Grundlagen der Supraleitung und eine kurze Zusammenstellung der bisherigen Arbeiten zur Dünnschichtherstellung von FBS. Kapitel 2 beschreibt experimentelle Methoden, die im Zuge dieser Arbeit verwendet wurden. Kapitel 3 berichtet von der Herstellung Co-dotierter Ba-122 Dünnschichten (Co-Ba-122) auf verschiedenen Fluoridsubstraten. Dabei wurde Augenmerk darauf gelegt, neben einem verbesserten epitaktischen Wachstum der Dünnschichten die supraleitenden Eigenschaften nicht zu beeinträchtigen. Anzumerken ist, dass in diesem Rahmen  $T_c$ -Rekord-Werte von 28 K in Co-Ba-122 erzielt werden konnten.

Kapitel 4 beschreibt die Hochfeld-Transporteigenschaften epitaktisch gewachsener P-dotierter Ba-122 Dünnschichten, die durch MBE hergestellt wurden. Unter den FBS zeigt P-dotiertes Ba-122 enorm hohe kritische Transport-Stromdichten, obwohl das  $T_c$  niedriger ist als bei  $LnFeAs(O,F)$  [ $Ln=Sm$  und  $Nd$ ]. Der Grund dafür konnte in der hohen Flusslinienkern-Energie des P-dotierten Ba-122 ermittelt werden.

Kapitel 5 behandelt Transporteigenschaften von epitaktisch gewachsenen  $SmFeAs(O,F)$ -Dünnschichten. In diesem Zusammenhang wurde ein dc-45 T-Hochfeldmagnet in Zusammenarbeit mit dem National High Magnetic Field Laboratory in Tallahassee, Florida, USA, genutzt.  $SmFeAs(O,F)$ -Dünnschichten wurden mit dem Molekularstrahl-Verfahren (MBE) hergestellt. Die Schichten zeigen sehr hohe kritische Transport-Stromdichten ( $J_c$ ) von über  $10^5$  A/cm<sup>2</sup> bei 45 T und 4.2 K für beide kristallographische Hauptrichtungen, parallel zur  $c$ -Achse und in der  $ab$ -Ebene. Diese Ergebnisse sehen sehr verheißungsvoll für eine Verwendung in Hochfeld-Anwendungen aus. Zusätzlich konnte durch die Untersuchung der Pinning-Eigenschaften ein Dimensionsübergang zwischen supraleitender Kohärenzlänge und FeAs-Ebenenabstand im Bereich 30-40 K beobachtet werden.

Kapitel 6 berichtet über die Hochfeld-Transporteigenschaften von  $NdFeAs(O,F)$ -Dünnschichten, die mithilfe des MBE-Verfahrens hergestellt wurden. In diesem Falle konnte ein Übergang von Abrikosov- zu Josephson-Flusslinien im Temperaturbereich 20-30 K beobachtet werden. Zusätzlich konnte die winkelabhängige kritische Stromdichte mit dem anisotropen Ginzburg-Landau-Ansatz skaliert werden. Die erhaltenen Parameter für verschiedene Temperaturen steigen mit fallender Temperatur. Dieses Verhalten ist gegensätzlich zu dem in Co-dotiertem Ba-122 gefundenen. Kapitel 7 gibt eine Zusammenfassung dieser Arbeit.



# Contents

<b>List of Figures</b>	<b>ix</b>
<b>List of Tables</b>	<b>xiii</b>
<b>1 Introduction</b>	<b>1</b>
1.1 Motivation . . . . .	1
1.2 Background (superconductivity and Fe pnictides) . . . . .	4
1.2.1 Fundamentals of superconductivity . . . . .	4
1.2.2 Type - II superconductors: Pinning . . . . .	5
1.2.3 Superconductivity in Fe pnictides . . . . .	9
1.3 Growth mechanisms of thin films . . . . .	14
1.4 Thin film growth of Fe-pnictides . . . . .	15
<b>2 Experimental</b>	<b>19</b>
2.1 Pulsed laser deposition (PLD) . . . . .	19
2.2 Molecular beam epitaxy (MBE) . . . . .	20
2.3 Reflection high energy electron diffraction (RHEED) . . . . .	22
2.4 Structural characterisation by X-ray diffraction . . . . .	24
2.5 Transport measurements . . . . .	26
2.6 Transmission electron microscopy (TEM) . . . . .	27
<b>3 Versatile substrates for Fe-based superconducting thin films</b>	<b>29</b>
3.1 Scientific problems . . . . .	29
3.2 Employing fluoride substrates . . . . .	31
3.3 Structural properties of Co-doped Ba-122 . . . . .	32
3.4 Superconducting properties of Co-doped Ba-122 grown on fluoride substrates	34
3.5 Summary of the chapter . . . . .	39

<b>4</b>	<b>Unusually high critical current in clean P-doped BaFe<sub>2</sub>As<sub>2</sub> single crystalline thin films</b>	<b>41</b>
4.1	Scientific merit of P-doped Ba-122 . . . . .	41
4.2	MBE process of P-doped Ba-122 . . . . .	42
4.3	Structural properties and microstructure of P-doped Ba-122 . . . . .	43
4.4	Superconducting properties of P-doped Ba-122 . . . . .	46
4.5	Summary of the chapter . . . . .	54
<b>5</b>	<b>SmFeAs(O,F): a candidate for high-field magnet applications</b>	<b>57</b>
5.1	Scientific problems . . . . .	57
5.2	MBE process for SmFeAs(O,F) . . . . .	58
5.3	Structural properties and microstructure of SmFeAs(O,F) . . . . .	60
5.4	Superconducting properties of SmFeAs(O,F) . . . . .	61
5.5	Summary of the chapter . . . . .	69
<b>6</b>	<b>Transport properties of NdFeAs(O,F) in high magnetic fields</b>	<b>71</b>
6.1	Scientific merit of NdFeAs(O,F) . . . . .	71
6.2	MBE process of NdFeAs(O,F) . . . . .	71
6.3	Structural analysis of NdFeAs(O,F) by XRD . . . . .	73
6.4	Superconducting properties of NdFeAs(O,F) . . . . .	74
6.5	Summary of the chapter . . . . .	81
<b>7</b>	<b>Summary</b>	<b>83</b>
	<b>Bibliography</b>	<b>87</b>
	<b>List of publications</b>	<b>105</b>

# List of Figures

1.1	Chronological development of the critical temperature for superconductors	2
1.2	Pairing mechanism for Cooper pairs . . . . .	4
1.3	Energy gap for unconventional superconductors . . . . .	6
1.4	Difference in the magnetic behaviour for type I and type II superconductors.	7
1.5	Artificial pinning centres in superconductors . . . . .	10
1.6	Crystal structures for 1111 and 122 Fe-based superconductors . . . . .	11
1.7	Phase diagram of the Ba-122 system. . . . .	13
1.8	Layer growth modes for thin films . . . . .	15
2.1	PLD chamber . . . . .	20
2.2	MBE chamber . . . . .	21
2.3	Front view of the MBE chamber . . . . .	22
2.4	Top view into the MBE chamber . . . . .	22
2.5	RHEED scheme. . . . .	23
2.6	Modes of RHEED diffraction mechanisms . . . . .	24
2.7	X-ray device . . . . .	25
2.8	Schematic pole figure . . . . .	26
2.9	Hybrid magnet in Tallahassee, USA. . . . .	27
3.1	RHEED images of the in-situ growth of the Ba-122 phases . . . . .	30
3.2	$\theta - 2\theta$ scans for the Ba-122 thin films . . . . .	31
3.3	Pole figure for the films grown on the fluoride substrates . . . . .	33
3.4	$\phi$ -scans of the (103) reflection of Ba-122 grown on $\text{CaF}_2$ , $\text{SrF}_2$ and $\text{BaF}_2$ . .	35
3.5	HRTEM pictures of Co-doped Ba-122 thin film grown on $\text{CaF}_2$ . . . . .	36
3.6	TEM pictures of Co-doped Ba-122 thin films grown on $\text{BaF}_2$ and $\text{CaF}_2$ substrates . . . . .	37
3.7	Resistance measured curves at the superconducting transition . . . . .	38
3.8	$J_c$ of Co-doped Ba-122 thin films grown on $\text{CaF}_2$ . . . . .	39
3.9	Phase diagram of Co-doped Ba-122 on different substrates . . . . .	40

4.1	Structural measurement data for Sample A . . . . .	44
4.2	Structural measurement data for Sample B . . . . .	45
4.3	TEM picture of sample A . . . . .	46
4.4	TEM picture of sample B . . . . .	47
4.5	Resistive measurement of different P-doped Ba-122 thin films. . . . .	47
4.6	Field dependence of the resistive measurements . . . . .	48
4.7	Temperature dependence of the upper critical field . . . . .	49
4.8	Self-field $J_c$ of the P-doped Ba-122 thin film in comparison to other materials having comparable $T_c$ . . . . .	50
4.9	Field dependence of the $J_c$ of P-doped Ba-122. . . . .	51
4.10	Blatter scaling of the angle dependence of $J_c$ and the temperature depend- ence of resulting $\gamma$ values . . . . .	52
4.11	Doping dependence of the vortex core energy . . . . .	55
4.12	Pinning force density of the P-doped Ba-122 thin films A and B . . . . .	55
5.1	Structural properties of SmFeAs(O,F) . . . . .	59
5.2	Microstructural analyses by TEM . . . . .	60
5.3	Laser cutting procedure and the result . . . . .	61
5.4	In-field resistivity ( $\rho$ ) measurements of SmFeAs(O,F) film up to 45 T and the analyses of the activation energy of the pinning potential ( $U_0$ ) . . . . .	62
5.5	Upper critical field . . . . .	63
5.6	In-field critical current density ( $J_c$ ) performance of SmFeAs(O,F) thin film at 4.2 K. . . . .	63
5.7	Magnetic field dependence of $J_c$ at different temperatures . . . . .	64
5.8	General effect of intrinsic and extrinsic pinning on the field dependence of $J_c$ . . . . .	65
5.9	Field and orientation dependence of $J_c$ . . . . .	67
6.1	Growth of NdFeAs(O,F) thin films by MBE . . . . .	72
6.2	AFM picture of the Nd-1111 surface . . . . .	73
6.3	$R(T)$ and structural characterisation of the Nd-1111 thin film . . . . .	74
6.4	Magnetisation measurement of the Nd-1111 thin film . . . . .	75
6.5	Resistive measurement in dependence of the applied magnetic field. . . . .	76
6.6	$H_{c2}$ of the Nd-1111 thin film. . . . .	77
6.7	Arrhenius plot . . . . .	78
6.8	Field dependence of $J_c$ at 4.2 K for the Nd-1111 thin film . . . . .	78
6.9	Field dependence of $F_p$ at various temperatures in both main directions . . . . .	79
6.10	Angle dependence of $J_c$ at various temperatures . . . . .	80

6.11 Ginzburg Landau scaling of the  $J_c$  . . . . . 81





# List of Tables

1.1	Comparison of cuprates and FBS. . . . .	3
1.2	Literature data for type I superconductors (elemental superconductors). . .	9
1.3	Literature data for type II superconductors . . . . .	9
1.4	Lattice structure properties of various superconductors . . . . .	10
3.1	Deposition temperature and layer thickness of the Co-doped Ba-122 thin films. . . . .	32
3.2	Lattice parameters and misfit data of the Ba-122 on different substrates. .	33
4.1	Growth parameters of P-doped Ba-122 thin films prepared by MBE . . . .	42
4.2	Structural data and superconducting properties for films A and B . . . . .	43



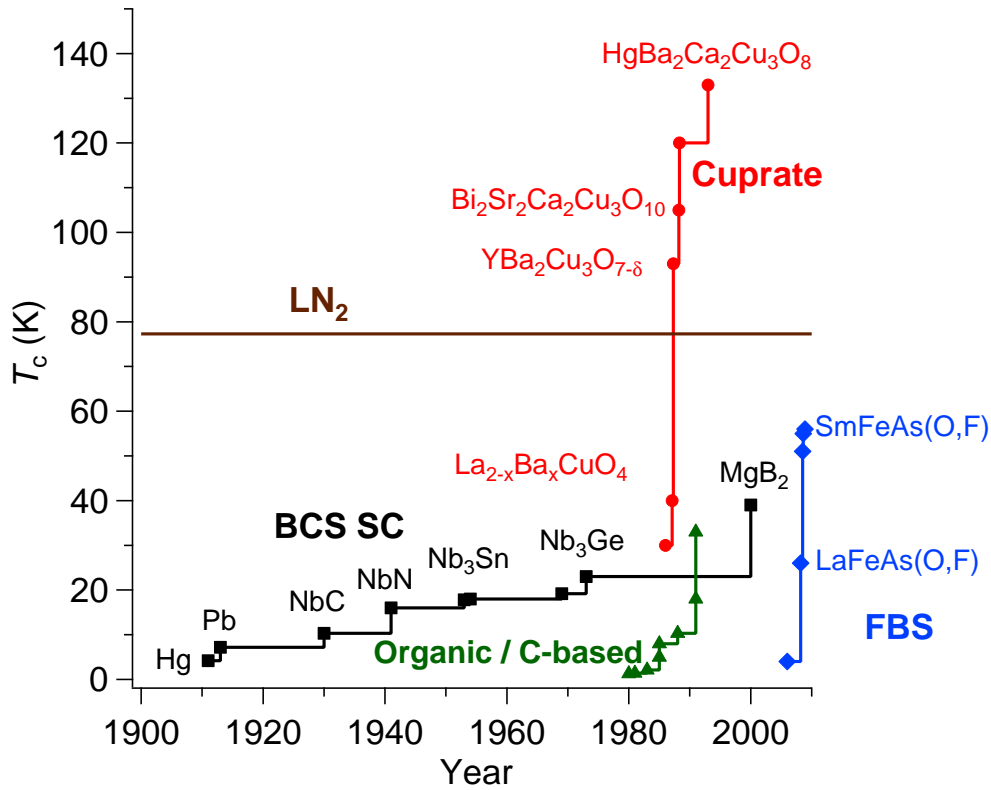
# 1 Introduction

## 1.1 Motivation

Over the last 100 years, superconductivity and its phenomena have inspired scientists all over the world. Since the first discovery of superconductivity in mercury in 1911, new materials, new methods and new applications appeared that influence our daily life tremendously. Figure 1.1 presents a chronological overview of the development of superconductivity regarding the superconducting transition temperature  $T_c$  for various materials. A slow progress in rising  $T_c$  of the so-called BCS (Bardeen-Cooper-Schrieffer) superconductors has led to a fading interest in superconductivity. This situation was changed dramatically by the discovery of organic superconductors, followed by cuprates [1]. Particularly, those Cu-based superconductors have suddenly increased the  $T_c$  record value above the prominent border of 77.3 K (i.e. the boiling point of nitrogen at ambient pressure). Such a high  $T_c$  cannot be explained by the conventional phonon mediated mechanism (i.e. BCS theory). Additionally, a cheap coolant, like liquid nitrogen, rather than the notoriously high-priced liquid helium can be used for reaching the superconducting state. Hence, not only scientists but also the public have been interested in this new material class.

In 2000, Nagamatsu *et al.* [2] reported findings of superconductivity in  $\text{MgB}_2$ , which presents the highest  $T_c$  (39 K) among the BCS superconductors so far. This material shows unique properties: (i) two band ( $\sigma$  and  $\pi$  bands) superconductivity and (ii) a relatively large coherence length unlike high- $T_c$  cuprates.  $\text{MgB}_2$  can be cooled by liquid hydrogen in order to obtain the superconducting state. Additionally, thanks to the recent development of cryocooler technology, various applications implementing  $\text{MgB}_2$  have been proposed and demonstrated.

After their discovery in 2006 [3], the Fe-based superconductors (FBS) again triggered great interest in the condensed matter physics community, in 2008, due not only to new superconductivity but also the fact that one of the constituent elements is Fe. It was believed that magnetic Fe destroys superconductivity. This, therefore, could provide new physics of the pairing mechanism, which is still under debate for this new material class [4].


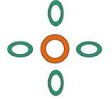


**Figure 1.1:** Chronological development of the critical temperature for superconductors. The brown line marks the boiling temperature for liquid N<sub>2</sub>, which is a threshold of great importance for applications.

Within a few weeks after the first report, other FBS were discovered with  $T_c$  up to 55 K in SmFeAs(O,F), a member of the so-called oxypnictides. From the point of applications, FBS offer very interesting properties such as high upper critical fields ( $H_{c2}$ ) and a low anisotropy at low temperatures, which indicates that this material class may not only be suitable but also favourable for high-field magnet applications.

It has been reported that FBS have a lot of similarities with cuprates. From the point of history, both FBS and cuprates have been discovered during the research of magnetic semiconductors and ferroelectric materials, respectively (see Table 1.1). In other words, both materials are by-products of different research areas. The degree of freedom for material designing is quite high for both cases, since a lot of different compounds have been reported. The ground state of the mother compounds is antiferromagnetic; whereas, the cuprates are Mott insulators, the FBS are metals. A possible pairing mechanism is spin fluctuation for both materials. For FBS, it has been reported that orbital fluctuation is also responsible for Cooper pairing.

**Table 1.1:** Comparison of cuprates and FBS.

	<b>Cuprates</b>	<b>FBS</b>
<b>History of discovery</b>	During the research of ferroelectric materials (1986) Ba-doped $\text{La}_2\text{CuO}_4$ ( $T_c=35$ K)	During the research of magnetic semiconductors (2008) $\text{LaFePO}$ ( $T_c=6$ K), $\text{LaFeAs(O,F)}$ ( $T_c=26$ K)
<b>Degree of freedom for material designing</b>	<b>High</b> $\text{HgBa}_2\text{Ca}_2\text{Cu}_3\text{O}_8$ ( $T_c=135$ K), $\text{Bi}_2\text{Sr}_2\text{Ca}_2\text{Cu}_3\text{O}_{10}$ ( $T_c=110$ K), ( <i>LRE</i> ) $\text{Ba}_2\text{Cu}_3\text{O}_7$ ( <i>LRE</i> =Nd, $T_c=95$ K), etc.	<b>High</b> $\text{LnFeAs(O,F)}$ ( $\text{Ln}=\text{Sm}$ , $T_c=55$ K), (Ba,K) $\text{Fe}_2\text{As}_2$ ( $T_c=38$ K), $\text{LiFeAs}$ ( $T_c=18$ K), $\text{FeSe}$ ( $T_c=8$ K) etc.
<b>Relationship between magnetism</b>	Parent compound: Mott insulator	Parent compound: Antiferromagnetic metal
<b>Glue</b>	Spin fluctuations?	Spin or Orbital fluctuations?
<b>Structure of the order parameter</b>	<i>d</i> -wave, single-band 	<i>s</i> -wave (sign-change) multi-band 

The pairing symmetry for cuprates is *d*-wave whereas for FBS most materials are believed to be *s* $\pm$ -wave. As shown in Table 1.1, there are similarities between both material classes; however, distinct differences do exist. These observations have led to the publication of more than 15000 papers since the discovery of FBS in 2006. Reviews summarise the investigations for various aspects [5–14]. Whenever new materials are discovered, it is of high interest to explore possible applications. In order to address this issue, the focus will mainly be on transport properties using thin films. Thanks to their dimensionality, epitaxial thin films are favourable for electronic device applications and investigating transport as well as optical properties. Recent success in fabricating epitaxial FBS thin films opens a new horizon for investigating their intrinsic properties as well as exploring possible superconducting applications.

This thesis reports on a novel possibility for the epitaxial growth of Co-doped Ba-122 thin films on fluoride substrates (Chapter 3) as well as on the high-field transport properties of P-doped Ba-122 (Chapter 4),  $\text{SmFeAs(O,F)}$  (Chapter 5), and  $\text{NdFeAs(O,F)}$  (Chapter 6). In the following, references which are displayed in bold digits mark own results.

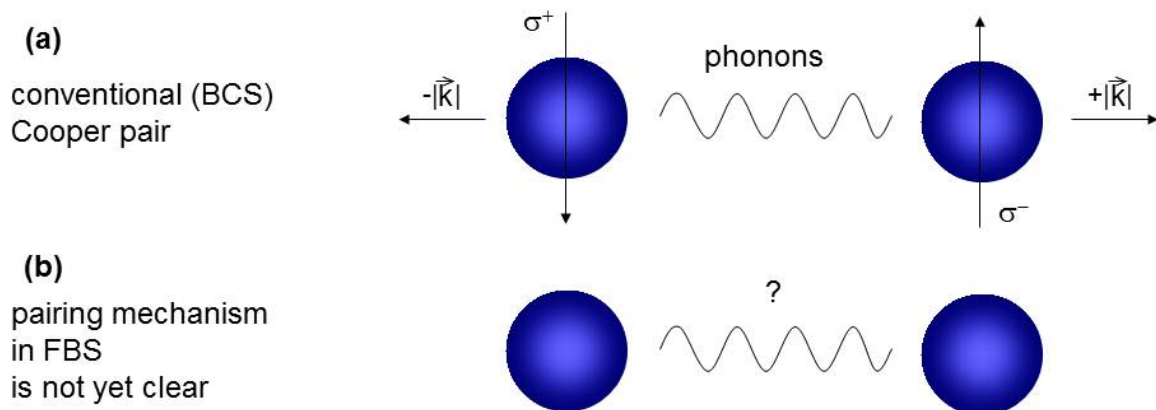
## 1.2 Background (superconductivity and Fe pnictides)

### 1.2.1 Fundamentals of superconductivity

When Heike Kamerlingh Onnes and his student Gilles Holst conducted temperature dependent resistance measurements on Hg, they observed zero resistance below 4.2 K. This resistivity drop was defined as the superconducting transition temperature,  $T_c$ . The capability to transfer energy without losses was a great achievement, and therefore Onnes immediately tried to make a superconducting magnet in order to generate large magnetic fields. However, this idea has soon turned out to be difficult, since Hg is a type I superconductor.

In 1933, Walther Meißner and Robert Ochsenfeld discovered a perfect diamagnetic behaviour of materials in the superconducting state, today known as the Meißner-Ochsenfeld effect, which arises independent from the thermodynamic way in the  $(B, T)$ -phase diagram. Due to shielding currents, the applied magnetic field gets pushed out of the material when entering the superconducting state in the field cooling process. The third basic feature of superconductivity is the Josephson effect, which was predicted by Brian David Josephson in 1962. He calculated the tunnelling current of Cooper pairs through a barrier between two superconductors [15].

In 1957, John Bardeen, Leon Neil Cooper and John Robert Schrieffer theoretically described the superconducting state as a quantum effect presenting the so-called BCS theory [15–17]. Cooling a BCS superconductor below  $T_c$  leads to the creation of so-called Cooper pairs consisting of two electrons which have opposite spin, identical norm as well as opposite momentum.



**Figure 1.2:** Schematic illustration of the pairing mechanism of the Cooper pairs for (a) conventional and (b) unconventional superconductors.

The interplay between both electrons is formed by quantified lattice oscillations, phonons. The total electrical charge and spins are  $2e$  and zero, respectively; therefore, the Cooper pair can be treated as a boson that does not obey the Pauli principle. Thus, it is much more likely that all bosons can be described by one macroscopic wave function which means that they belong to the same quantum state, obtaining a quantum stability. Hence, it is not possible that Cooper pairs occupy quantum states other than the one described by the macroscopic wave function. In this way, the electrons cannot interact with the crystal lattice which would lead to a forbidden change of their momentum resulting in the capability of frictionless mobility.

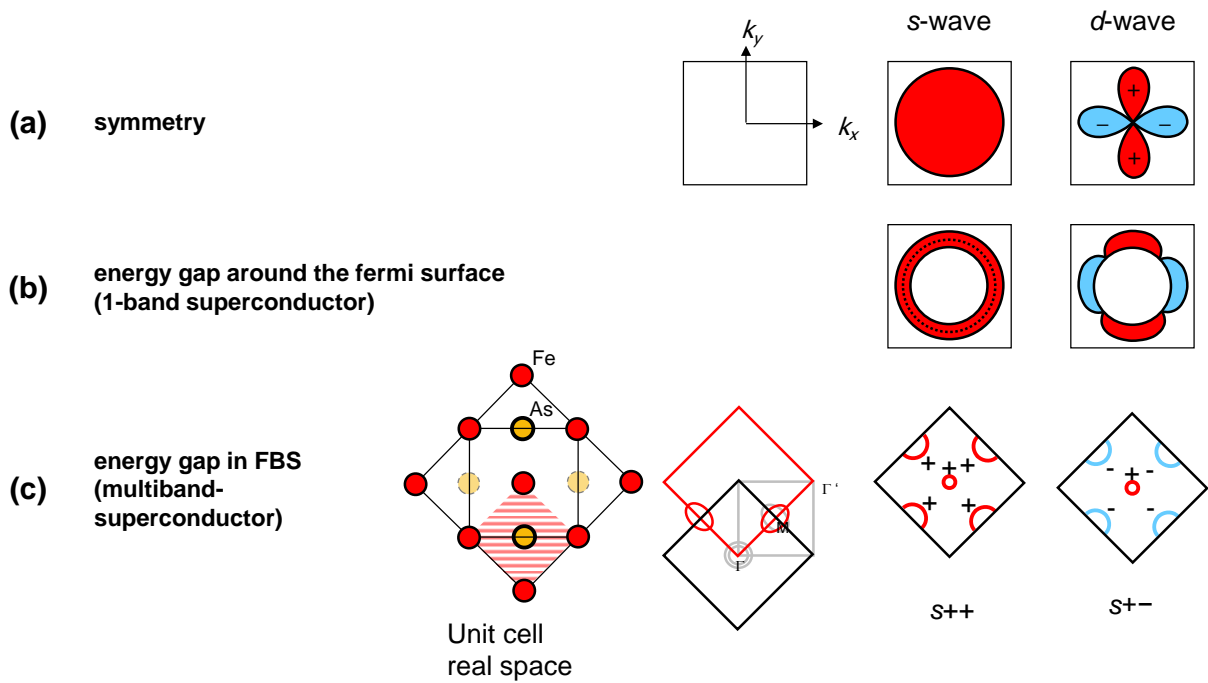
When entering the superconducting state, an energy gap is formed around the Fermi surface. For conventional superconductors, the shape of the energy gap is isotropic, which means it is formed in a symmetric way in the  $\vec{k}$  space. This is called *s*-wave symmetry. In contrast, for unconventional superconductors, the energy gap is not isotropic, the wave symmetry for the superconductor is changed. One example is the *d*-wave symmetry for cuprates (see Fig. 1.3). For FBS, the fact of multiband superconductivity adds, which means that the electrons that form the Cooper pairs originate from different conduction bands. There are five different energy bands at the Fermi level (three hole bands and two electron bands) [18, 19].

In case of FBS, the kind of the coupling has still not been clarified (see Fig. 1.2). Besides phonons, there might be spin fluctuations as well as orbital fluctuations causing the coupling between the Cooper electrons. The high superconducting transition temperature cannot be explained by a phononic coupling (i.e. BCS theory); therefore, spin and/or orbital fluctuation can be assumed [20]. This kind of coupling mechanism is a central subject for current investigations and is discussed controversially.

## 1.2.2 Type - II superconductors: Pinning

According to their in-field behaviour, macroscopic superconductors can be divided into type I and type II. The criterion for this classification originates from the Ginzburg-Landau theory [17]. The ratio of the London penetration depth,  $\lambda$ , of the magnetic field into the superconductor and the coherence length of the Cooper pairs,  $\xi_{GL}$ , which is a measure for the spatial dimension of the Cooper pair in the superconductor, is called Ginzburg-Landau parameter:

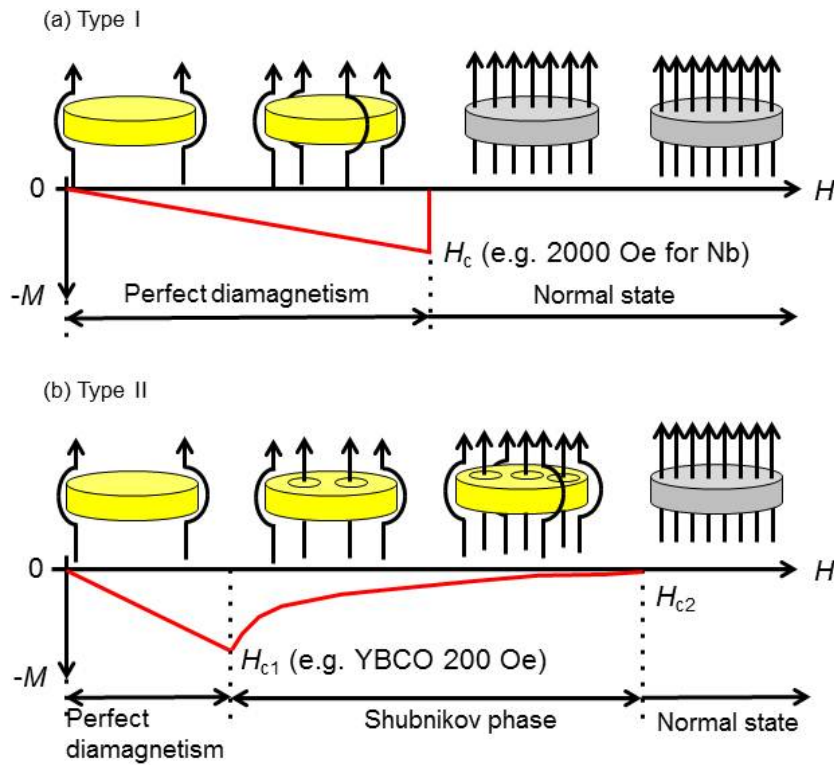
$$\kappa = \frac{\lambda}{\xi_{GL}} \quad (1.1)$$



**Figure 1.3:** Deformations of the energy gap for unconventional superconductors in the reciprocal space, when assuming a sphere-like Fermi surface (here 2-dimensional). (a) Symmetry of the Fermi surface in  $\vec{k}$  space (b) When entering the superconducting state an energy gap is forming (red and blue area) around the Fermi surface. (c) Fermi surface for multiband superconductivity.



If  $\kappa < \frac{1}{\sqrt{2}}$ , it is referred to as type I superconductor. If the opposite relation holds (i.e.  $\kappa > \frac{1}{\sqrt{2}}$ ), it is referred to as type II superconductor. The thermodynamic phase diagram of the type II superconductors implies the Shubnikov phase which lies above the lower critical field,  $H_{c1}$ , in which quantized flux lines penetrate the superconductor completely. By increasing the external magnetic field, an increasing number of fluxoids enters the superconductor until the superconductor is filled by fluxoids at the upper critical field,  $H_{c2}$ . For type II superconductors - and in difference to type I superconductors - the field behaviour is unequal: in the Shubnikov-phase the material does not show ideal diamagnetism anymore. The  $H_{c2}$  marks the transition from the superconducting to the normal state in the material (shown in Fig. 1.4). In case of anisotropic behaviour of the  $H_{c2}$ , the respective  $\gamma_{H_{c2}} = H_{c2\parallel ab}/H_{c2\parallel c}$  is defined as the ratio of the values in  $H\parallel ab$  and  $H\parallel c$  direction. FBS are extreme type II superconductors.



**Figure 1.4:** Difference in the magnetic behaviour for type I and type II superconductors. (a) Type I superconductors show a perfect diamagnetism up to a certain field strength, the flux is repelled completely. At  $H_c$ , superconductivity is destroyed and the flux can penetrate the superconductor freely. The given example is valid for very clean Nb. (b) Type II superconductors show a perfect diamagnetism up to a certain field strength, the so-called  $H_{c1}$ . For higher fields the magnetic field can partially penetrate the superconductor without destroying superconductivity, i.e. the Shubnikov phase. At  $H_{c2}$  superconductivity collapses.

Other very important material parameters, especially for power applications, are the critical current density,  $J_c$ , and the irreversibility field,  $H_{\text{irr}}$ . The superconductivity still survives at  $H_{\text{irr}}$ , however,  $J_c$  is zero. Applying a voltage to the material in the superconducting state produces a supercurrent (i.e. no measurable losses), which has a certain upper limit. If no external field is applied, the superconductor is exposed to the field created by its own current. In this case the maximum supercurrent density is the so-called self-field  $J_c$ . With increasing externally applied field  $J_c$  decreases. Comparable to the  $H_{c2}$ , in case of anisotropic behaviour the  $\gamma_J = J_{c\parallel ab}/J_{c\parallel c}$  is defined as the ratio of the values in  $H\parallel ab$  and  $H\parallel c$  direction.  $\gamma$  values that are evaluated from the anisotropic Ginzburg-Landau scaling are defined as  $\gamma_{J_c G_i}$  [21]. In this work,  $J_c$  will be investigated for different materials.

Whilst type I superconductors repel externally applied magnetic fields to the surface of the material, type II superconductors can partially be penetrated by magnetic flux. Applying an electrical current to the unpinned superconductor would cause the flux lines to move due to the so-called Lorentz force, and therefore result in an electrical resistance. Cooper pairs will break and have to form again. To prevent the movement of the flux lines, these have to be pinned. Defects in the crystal structure, small angle grain boundaries, chemical impurities or even variations in the homogeneity of the material can be used to provide a local stabilisation of the penetrating flux lines. Figure 1.5 shows a sketch of the dimensionality of artificial and natural pinning centres [22]. Tables 1.2 and 1.3 provide literature values of  $\xi$ ,  $\lambda$ ,  $T_c$  and  $H_c$  for type I and type II superconductors.  $H_c$  is much larger whereby  $\xi$  is much smaller for type II superconductors. The desired diameter of the effective pinning centres, to provide the maximum of the pinning potential  $U_0$ , should be as large as the coherence length  $\xi$ ; a larger defect will become an obstacle for the supercurrent path. For materials, intrinsic and extrinsic pinning should be distinguished. In case of intrinsic pinning, a superconducting layer itself works as a strong pinning centre, whereby extrinsic pinning is caused by normal precipitates, twin boundaries, and defects which are introduced extrinsically [23]. The extrinsic pinning is familiar in conventional superconductors. For high- $T_c$  materials, small defects such as globular defects can become pinning centres, because the coherence length is about one order of magnitude shorter compared to conventional superconductors [24].

The Lorentz force increases with increasing applied current and field. The pinning provides a localised pinning force density  $F_p = H \times J_c$ , which is a measure for the stability of the field dependence of the  $J_c$ . Usually, this pinning force density is strongly microstructure dependent and can show anisotropic behaviour.

**Table 1.2:** Literature data for type I superconductors (elemental superconductors) [17].

	$\xi_{GL}$ (nm)	$\lambda$ (nm)	$T_c$ (K)	$\mu_0 H_{c1}$ (T) at 0 K
Al	1600	50	1.2	0.01
Pb	83	39	7.2	0.08
Sn	230	51	3.7	0.03

**Table 1.3:** Literature data for type II superconductors. Because of there anisotropic crystal structure the values  $\xi_{ab}$  and  $\lambda_{ab}$  are given for the  $ab$  plane [11, 14, 25–27]. The  $H_{c2}$  values refer to the direction with the respective lower values.

	$\xi_{ab}$ (nm)	$\lambda_{ab}$ (nm)	$T_c$ (K)	$\mu_0 H_{c2}$ (T) at 0 K
Nb <sub>3</sub> Sn	11	200	18	25
YBCO	2.2	120	92	> 100
MgB <sub>2</sub>	10	85	39	14
Ba-122	3	200	25	60
Sm-1111	2.5	200	55	> 100
Fe(Se,Te)	1.5	500	16	55

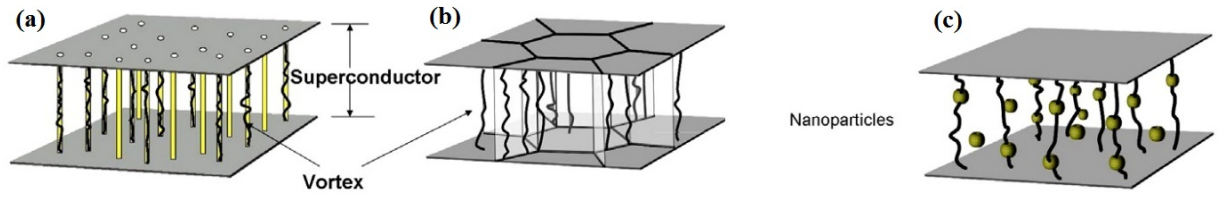
### 1.2.3 Superconductivity in Fe pnictides

In February 2008, Kamihara *et al.* reported superconductivity in F-doped LaFeAsO [4], initiating worldwide efforts to investigate these new FBS. Shortly after this discovery, many Fe-based superconducting compounds were discovered. Different families of the Fe-based superconductors can be distinguished [28], such as FeSe (“11”), LiFeAs (“111”), SrFe<sub>2</sub>As<sub>2</sub> (“122”), LaFeAsO (“1111”), and Sr<sub>3</sub>Sc<sub>2</sub>O<sub>5</sub>Fe<sub>2</sub>As<sub>2</sub> (“32522”).

Every family exhibits a tetragonal symmetry of the crystal structure at room temperature. An atomic layer existing of Fe atoms along the tetrahedrally ordered bonds to the phosphorous-, arsenic-, selenium- or tellurium anions, which are shifted upwards and downwards to the Fe layers. Therefore, the chessboard like shapes are characteristic of those new systems. Schematic illustrations of the crystal structures of the “122” and the “1111” systems are shown in Fig. 1.6. Table 1.4 summarises the structural parameter for the mother compounds of Ba-122, SmFeAsO, and NdFeAsO studied in this thesis.

It was believed that “magnetic Fe” destroys the superconductivity, since it causes the Cooper pairs to “spin flip”. Hence, it was very unlikely that new superconductors with high  $T_c$  containing Fe would be discovered. As shown in Table 1.1, the pairing mechanism is assumed to be similar to the cuprates, because of the antiferromagnetism in the undoped compounds below the structural transition temperature where the structure changes from tetragonal to orthorhombic [29–32].

For Fe pnictides studied in this thesis, superconductivity is induced by chemical doping.



**Figure 1.5:** Artificial pinning centres in superconductors: (a) Linear defects: Screw dislocations or columnar defects. (b) Planar defects: Small angle grain boundaries or antiphase boundaries usually at the surface of large particles. (c) Point defects: Nanoparticles. This sketch is taken from Ref. [22].

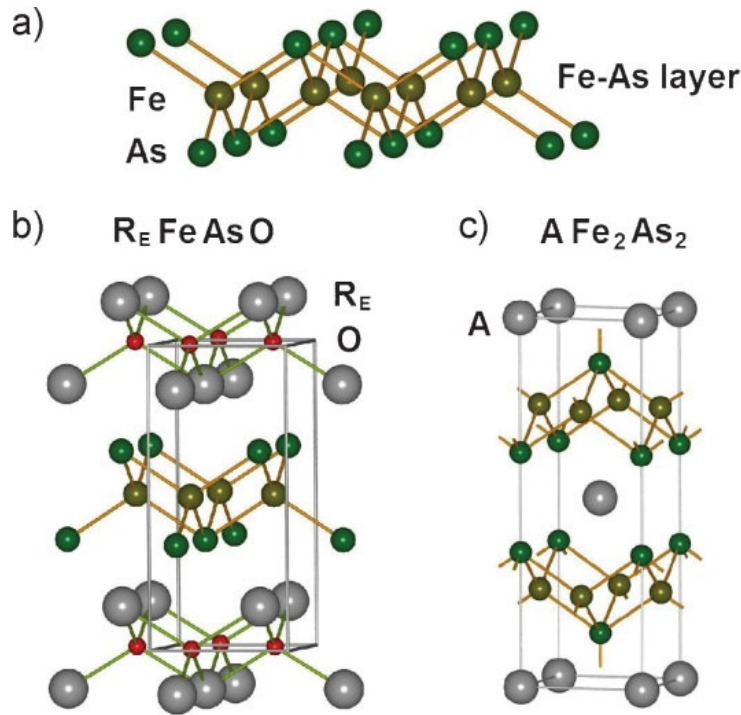
**Table 1.4:** Lattice structure properties of the Ba-122 [34, 35], the Sm-1111 [36], and the Nd-1111 [37] systems at room temperature.

Structural parameters			
	BaFe <sub>2</sub> As <sub>2</sub>	SmFeAsO	NdFeAsO
crystal system		tetragonal	
space group	I4/ <i>mmm</i>	P4/ <i>nmm</i>	P4/ <i>nmm</i>
lattice parameter <i>a, b</i>	3.963 Å	3.933 Å	3.963 Å
lattice parameter <i>c</i>	13.017 Å	8.495 Å	8.573 Å

There are three different kinds of doping, which will be explained below. Figure 1.7a shows the chemical-substitution phase diagram of BaFe<sub>2</sub>As<sub>2</sub> for hole doping (K), electron doping (Co), and isovalent doping (P).

**Hole doping.** For hole doping foreign atoms are implemented into the system, reducing the number of electronic charge carriers. The parent compound behaves antiferromagnetically with a Néel temperature ( $T_N$ ) of 140 K. As can be seen in Fig. 1.7a, for all cases  $T_N$  was reduced by chemical doping. Hole doping can be obtained by a partial substitution of Ba<sup>2+</sup> with K<sup>+</sup>. As a result, charge carriers (i.e. holes) are injected into the system and superconductivity appears at a K concentration of 16 % in Ba<sub>1-x</sub>K<sub>x</sub>Fe<sub>2</sub>As<sub>2</sub>. The maximum  $T_c$  of 38 K was obtained at  $x = 40\%$  [38]. K-doped Ba-122 shows the highest  $T_c$  in the Ba-122 family.

**Electron doping.** For electron doping two methods have been reported: one is that Fe<sup>2+</sup> is partially substituted by Co<sup>3+</sup> (or Ni<sup>4+</sup>). The other method is the partial substitution of Ba<sup>2+</sup> with La<sup>3+</sup> [39]. The former is so-called “direct doping” and the latter is “indirect doping”. In the case of Co doping, superconductivity appears at a doping level of 4 % [40]. For this concentration, superconductivity coexists with antiferromagnetism.



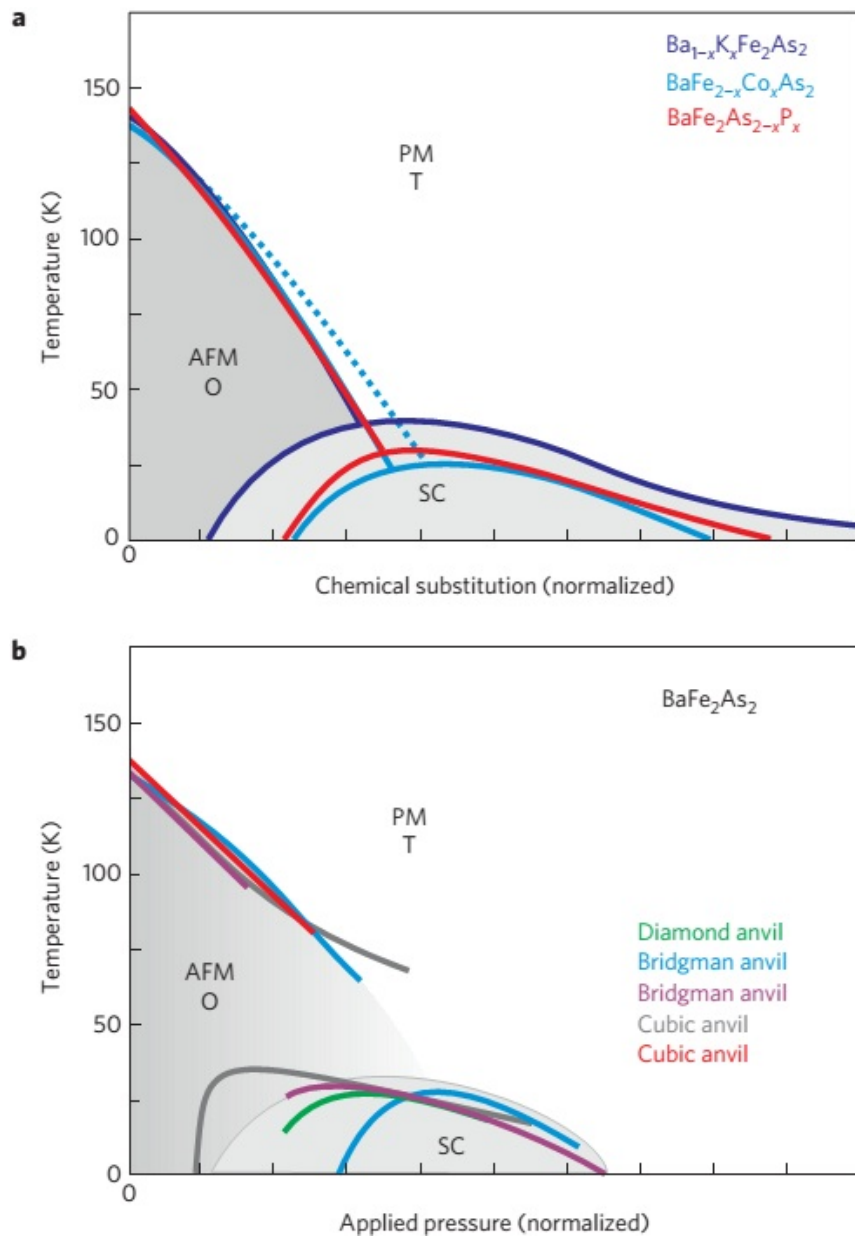
**Figure 1.6:** (a) Fe - As layer structure, (b) 1111 - layer structure ( $R_E$  = rare earth elements), and (c) 122 - layer structure ( $A$  = alkali earth elements) [33].

Further increasing the Co concentration up to around 7% rises  $T_c$  to around 23 K without any sign of antiferromagnetism. Finally, superconductivity vanishes at higher doping levels ( $x > 17\%$ ) [41]. In Chapter 3, the detailed fabrication, structural, and transport properties of Co-doped Ba-122 thin films will be described.

Similarly, electron doping has been achieved in “1111” systems by a partial substitution of O to F. This is the so-called “indirect doping”. “Direct doping”, in which the Fe site is partially substituted by Co or Ni, has also been reported [40, 42]. “Direct doping” always leads to a lower  $T_c$  for FBS, which is probably due to scattering. In Chapters 5 and 6, structural and transport properties of MBE-processed SmFeAs(O,F) and NdFeAs(O,F) thin films will be described.

**Isovalent doping.** For isovalent doping, atoms are implemented into the material without change of the charge carrier concentration. For Ba-122 this kind of doping has been done by a partial substitution of Fe with Ru [43], or As with P [44]. The ionic radius of  $As^{3-}$  is about 0.12 nm, whereas the corresponding value of  $P^{3-}$  is 0.106 nm. Hence, one can expect a lattice distortion by isovalent doping that can induce superconductivity. P-doped Ba-122 prepared by MBE is structurally and electro-magnetically investigated in Chapter 4.

Doping, as described above, is not the only way to induce superconductivity. Other parameters like strain have significant influence on the superconducting properties of materials. For instance, an inhomogeneous distribution of doping elements in the superconducting matrix can enhance the flux pinning force or induce strain and therefore superconductivity. Soon after the discovery of the Ba-122 systems, Kimber *et al.* reported that external pressure can play a similar role like chemical doping [45]. Figure 1.7b shows the phase diagram of  $\text{BaFe}_2\text{As}_2$  as a function of externally applied pressure. The  $T_N$  is decreasing with pressure. Superconductivity appears above a certain pressure level. This strain induced superconductivity was also observed in thin films [46].



**Figure 1.7:** (a) Chemical-substitution phase diagram of the BaFe<sub>2</sub>As<sub>2</sub> system, [28] shown for K [47], Co [40] and P [44] substitutions, with the amount of chemical substitution ( $x$ ). The dotted line indicates the structural transition between tetragonal (T) and orthorhombic (O) crystallographic phases observed for Co substitution, which is coincident with the paramagnetic (PM) to antiferromagnetic transition in the parent compound BaFe<sub>2</sub>As<sub>2</sub> [40]. (b) Phase diagram for BaFe<sub>2</sub>As<sub>2</sub> as a function of external pressure applied under various levels of hydrostaticity [44, 48–51]. The pressure axis for both diagrams is normalised to overlap the descent of the antiferromagnetic transitions for each experiment for simplified comparison.

## 1.3 Growth mechanisms of thin films

Five growth mechanisms can be responsible for the formation of thin films [52–55]. The most important processes describing the growth of the film on the substrate surface are mechanical adhesion, chemical adsorption, and adsorption because of van der Waals forces [56]. Therefore, the ratios between the surface energy of the substrate,  $E_S$ , the surface energy of the film,  $E_O$ , and the border surface energy between layer and substrate,  $E_G$ , are crucial. These energies, on the other hand, depend on parameters like growth temperature, saturation of the crystalline phase, and lattice misfit between the surface of the substrate and the layer. The five different growth mechanisms are:

1. Frank-van-der-Merwe growth (Layer growth: Fig. 1.8(a)): The substrate energy is higher than the sum of the interface energy,  $E_G$ , and the surface energy of the layer,  $E_O$ . The condensing atoms are more strongly bound to the substrate than to each other; thereby, the growth of the first layer of the thin film has to be finished before a second layer can grow. This mode has been observed for the growth of Ag deposited on W substrates [57], or Ge deposited on Si substrates [58].

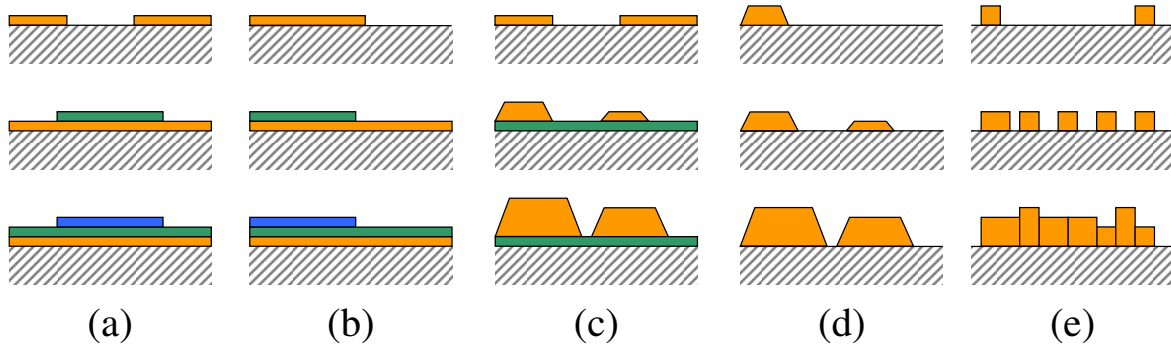
2. Step-by-step growth (Fig. 1.8(b)): Step-like growth of the layers. The sum of the surface energy of the layer and the interface energy is smaller than the surface energy of the substrate. In this regard the bottom layer does not have to be closed before the second layer can start growing. This growth mode usually occurs for slightly miscut substrates, where atoms nucleate at the surface steps of the crystal. During the growth process the steps grow expanding in in-plane direction.

3. Stranski-Krastanow growth (mixed growth: Fig. 1.8(c)): Because of internal and external factors, after initial layer growth (Frank-van-der-Merwe growth), the layer will continue to grow with the island growth mode (Vollmer-Weber growth).

4. Vollmer-Weber growth (island growth: Fig. 1.8(d)): The surface energy of the substrate is smaller than the interface energy and the surface energy. The interplay between the particles is stronger compared to the interaction of the particles to the substrate surface. Hence, small clusters will nucleate on the substrate surface growing into islands. This will lead to the formation of holes with a certain size that can reach down to the substrate surface. "11" belongs to this growth mode [59].



5. Columnar growth (Fig. 1.8(e)): The mobility of the atoms at the substrate surface is very small. The islands will not coalesce; instead, they will form brittle column like grains.



**Figure 1.8:** Schematic view of the different layer growth modes: (a) Layer growth, (b) Step-by-step growth, (c) Stranski-Krastanow growth, (d) Island growth, and (e) Columnar growth.

## 1.4 Thin film growth of Fe-pnictides

Single crystals have been commonly used for fundamental studies. However, it is not always possible to implement single crystals for such purposes, due to difficulties of single crystal growth for several reasons (e.g. thermodynamical instability). Thin films are often grown under non-equilibrium conditions. Therefore, thermodynamically unstable phases can be obtained. In FBS, most of the fundamental research has been conducted by using single crystals, except for “1111” [60]. Unlike single crystals, “1111” single crystalline thin films have been fabricated by molecular beam epitaxy (MBE), enabling the study of transport properties. Additionally, thin films also offer a unique opportunity for investigating the uniaxial pressure dependence of superconducting properties, since either contraction or expansion can be induced into the film by the lattice misfit within a critical thickness of stress relaxation. Furthermore, epitaxial thin films are favourable for electronic device applications and to investigate transport as well as optical properties thanks to their geometry. In this subsection, a brief history of FBS thin films is given.

**1111 compound.** In 2008, Hiramatsu *et al.* succeeded in the preparation of the iron oxypnictide LaFeAsO with perfect *c*-axis and in-plane alignment by pulsed laser deposition (PLD). Although the PLD target contained F, it seemed that the target stoichiometry was hardly transferred to the substrate. Soon after this report, Backen *et al.* reported on the

successful preparation of superconducting LaFeAs(O,F) thin films on LaAlO<sub>3</sub> (LAO) and MgO substrates using a two-step process which involved a room temperature deposition followed by postannealing [61]. The resultant films showed epitaxial growth with an onset  $T_c$  of 11 K; however, zero resistance was not observed. After the optimisation of the growth process, the superconducting properties improved: a  $T_{c,onset}$  of around 28 K with a  $T_{c,0}$  of around 20 K. However, the film showed a weak-link behaviour and, hence, a rather low  $J_c$  in the order of  $10^3$  A/cm<sup>2</sup> at low temperatures [62]. Fully epitaxial superconducting LaFeAs(O,F) thin film fabrication has been conducted after further optimisation of the processing conditions [60]. Nevertheless, this method is not suitable for fabricating superlattices and stack type junctions.

Kawaguchi *et al.* prepared epitaxial NdFeAs(O,F) (Nd-1111) thin films by MBE on GaAs substrates, achieving high  $T_c$  values of about 48 K with the help of an artificially deposited NdOF cap layer on top of the NdFeAsO for the supply of F [63]. The same technique was also implemented for LaFeAs(O,F) [64]. Later, Uemura *et al.* prepared NdFeAs(O,F) epitaxial thin films on various substrates [65]. Among them, the film grown on CaF<sub>2</sub> exhibited high  $T_{c,onset}$  and  $T_{c,0}$  values of about 56 K and 52 K, respectively.

Almost the same technique has been implemented by Ueda *et al.* for epitaxial growth of SmFeAs(O,F) on various substrates [66–68]. The resultant films on CaF<sub>2</sub> achieved a record  $T_{c,onset}$  and  $T_{c,0}$  of 57.8 K and 56.4 K, respectively. A clear correlation between  $T_{c,onset}$  and the epitaxial strain has been reported: the less epitaxial strain, the higher the  $T_{c,onset}$ .

**122 compound.** The “122” is the most investigated compound among the Fe-Arsenides. The first epitaxial thin film was Co-doped Sr-122, which has been grown by Hiramatsu *et al.*, using PLD [69]. The thin film showed a  $T_{c,onset}$  of 20 K and a  $T_{c,0}$  of 15 K with rather low  $J_c$  values of about 20 kA/cm<sup>2</sup> at 4.2 K. The  $H_{c2}$  anisotropy at low temperatures was found to be close to 1 [70]. Nevertheless, Co-doped Ba-122 was found to be more stable in air or water vapor [71]. Other advantages were found in the higher crystallinity with an atomically flat surface and in the sharper superconducting transition width of  $\Delta T_c = 1.1 - 1.3$  K. The  $J_c$  showed high values of 1-4 MA/cm<sup>2</sup> on (La,Sr)(Al,Ta)O<sub>3</sub> (LSAT) and MgO substrates probably due to the enhancement of the pinning performance, as well as crystallinity [72, 73]. The group of Tokyo Institute of Technology has used a Nd:YAG laser with the 2<sup>nd</sup> harmonic ( $\lambda = 532$  nm) for the deposition of “122” and “1111”.

Epitaxial Co-doped Ba-122 thin films on SrTiO<sub>3</sub> (STO), LSAT, YAlO<sub>3</sub> (YAO) and LAO substrates were deposited by PLD using a KrF excimer laser ( $\lambda = 248$  nm) was found by Iida *et al.* A strong correlation between the  $c/a$  ratio and the  $T_{c,onset}$  was reported [74]. Later, other techniques for the deposition of Co-doped Ba-122 thin films were developed. Lee *et al.* have reported that employing STO or BaTiO<sub>3</sub> template layers yields high

crystalline quality as well as  $J_c$  values [75]. BaFeO<sub>3</sub> nano-pillars were embedded in the Co-doped Ba-122 matrices. As a result, a huge  $c$ -axis peak in the angular dependent  $J_c$  was observed.

Thersleff *et al.* reported on the use of Fe as a buffer layer on MgO [76]. As a result, high crystallinity and very good reproducibility were achieved without compromising the superconducting properties. Detailed TEM investigations revealed that bcc Fe directly bonds to the FeAs tetrahedron in Ba-122.

Soon thereafter, the optimised thickness of this Fe layer was found to be 15 nm, and the superconducting properties improved strongly, exhibiting self-field  $J_c$  values of 0.45 MA/cm<sup>2</sup> at 12 K, compared to the films grown without Fe-buffer layer [77, 78]. We investigated in the electronic phase diagram of As-deficient thin films grown on Fe-buffered MgO achieving a high  $T_{c,90}$  value of 27.9 K [79]. Implementing Fe-buffer layers offered a lot of opportunities: demonstrating a first FBS-coated conductor [80], multilayers [81], and inducing superconductivity in parent Ba-122 thin films by strain [46]. In 2013, Lee *et al.* showed the possibility to grow artificially engineered undoped Ba-122/Co-doped Ba-122 compositionally modulated superlattices producing  $ab$ -aligned nanoparticle arrays, that result in very large  $J_c$  and  $H_{irr}$  enhancements over a wide angular range [82].

K-doped  $Ae122$  ( $Ae = Sr, Ba$ ) shows the highest  $T_c$  of around 38 K in the 122 family. The preparation of thin films in this case was found to be very difficult because of the high reactivity and volatility of potassium. Lee *et al.* reported on the preparation of K-doped Ba-122 thin films by a two-step process similar to that used for LaFeAs(O,F) described above. The films show a high  $T_{c,onset}$  of 40 K and a  $T_{c,0}$  of 37.5 K [83]. K-doped Ba-122 films have also been grown by MBE [84], applying a low temperature growth which results in  $T_{c,onset}$  and  $T_{c,0}$  of 38.3 K and 35.5 K, for  $Ae = Ba$ . For  $Ae = Sr$ , the films exhibit values of  $T_{c,onset} = 33.2$  K and  $T_{c,0} = 30.0$  K. However, the K-doped Ba-122 thin films degrade at ambient atmosphere. Therefore, a coating for protection against air is necessary.

In 2012, Adachi *et al.* reported on the growth of P-doped Ba-122 thin films on MgO substrates using PLD. They achieved  $T_{c,onset}$  and  $T_{c,0}$  values of 26.5 K and 24 K, respectively [85]. They also obtained high self-field  $J_c$  values of 3.5 MA/cm<sup>2</sup> at 4.2 K. The first deposition of P-doped Ba-122 with the use of MBE was reported by Sakagami *et al.* in 2013. The resultant film showed a high  $T_c$  of 30.5 K with a sharp transition. The film with an excess of Fe, which was supplied during the growth, exhibited a record self-field  $J_c$  value of 12 MA/cm<sup>2</sup> at 4.2 K measured by magnetisation measurements [86]. Following this path, Miura *et al.* published on the effect of artificial pinning centers [BaZrO<sub>3</sub> (BZO)] on the anisotropy of  $H_{c2}$  and  $J_c$  for P-doped Ba-122 thin films. In these investigations, the density of BZO as well as the P content were changed [87, 88]. The resultant film showed

high self-field  $J_c$  values of  $6 \text{ MA/cm}^2$  at  $5 \text{ K}$  with  $3\%$  BZO particles as well as  $H_{c2}$  anisotropy values of  $\gamma_{H_{c2}} = 1.55$ . In 2014, Sato *et al.* employed higher deposition temperatures. They optimised the film growth to preferentially align dislocations along the  $c$ -axis, which worked well as  $c$ -axis vortex-pinning centers [89].

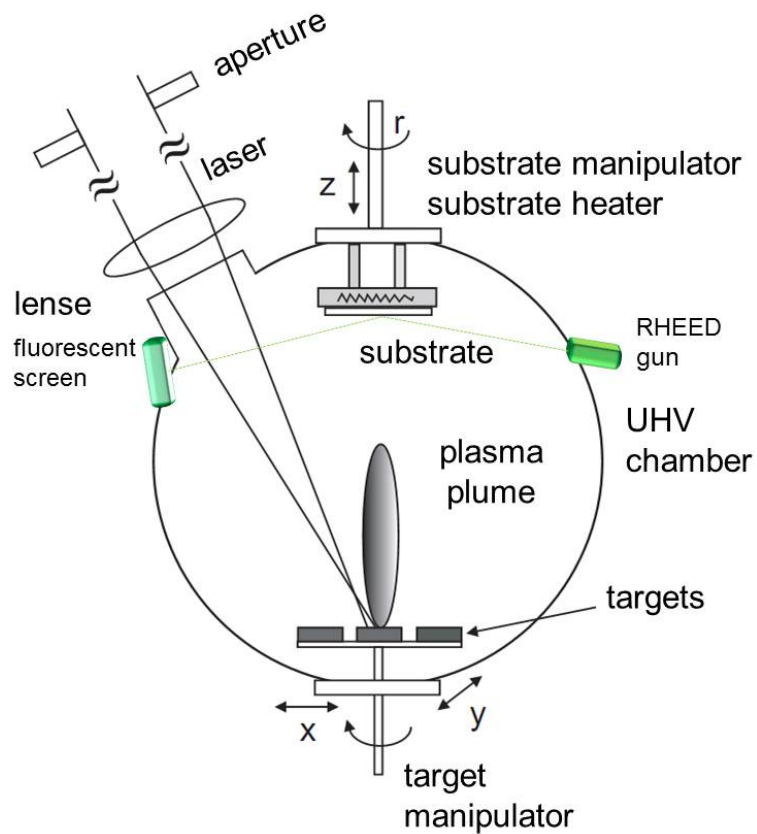
**11 compound.** The “11” superconductors have the lowest  $T_c$  among the FBS with one exception. The discovery of superconductivity above  $100 \text{ K}$  in single layered FeSe grown on doped STO by MBE, which was published in 2015 by Ge *et al.* [90]. The first fabrication of a thin film by PLD presenting a  $T_c$  of  $12 \text{ K}$  has been done by Wu *et al.* in 2009 [91]. Unlike other systems as “122” and “1111” the “11” or “111” compounds show superconductivity without doping or applied pressure. Further investigations have been performed regarding superconducting properties [92], as well as their structural dependence [93]. In this regard, Bellingeri *et al.* reported an enhancement of  $T_c$  up to  $21 \text{ K}$  in epitaxial thin films with high quality, grown on LAO and yttrium-stabilised zirconia substrates [59]. The  $J_c$  was measured by Tsukada *et al.* who prepared thin films on  $\text{CaF}_2$  using PLD and, despite the lower  $T_c$ , displayed a high in-field  $J_c$  at  $4.5 \text{ K}$  of  $5.9 \times 10^4 \text{ A/cm}^2$  at  $10 \text{ T}$  and  $4.2 \times 10^4 \text{ A/cm}^2$  at  $14 \text{ T}$  [94].

**111 compound.** In the case of the “111” compound, superconducting thin films are very hard to achieve. Due to the high volatility of Li, the preparation of LiFeAs thin films using deposition techniques are quite difficult. Nevertheless, in 2015, Chang *et al.* published the preparation of a LiFeAs thin film on a STO (001) substrate grown by MBE [95]. The intrinsic properties were investigated; the film showed a superconducting transition at  $16 \text{ K}$  in the transport measurement. From magnetoresistance measurements  $H_{c2}$  was estimated to  $13.0 \text{ T}$ . The authors claim that the used film preparation method can be transferred to other “111” compounds like NaFeAs. In this regard, these investigations open multiple new possibilities to explore the “111” compounds.

## 2 Experimental

### 2.1 Pulsed laser deposition (PLD)

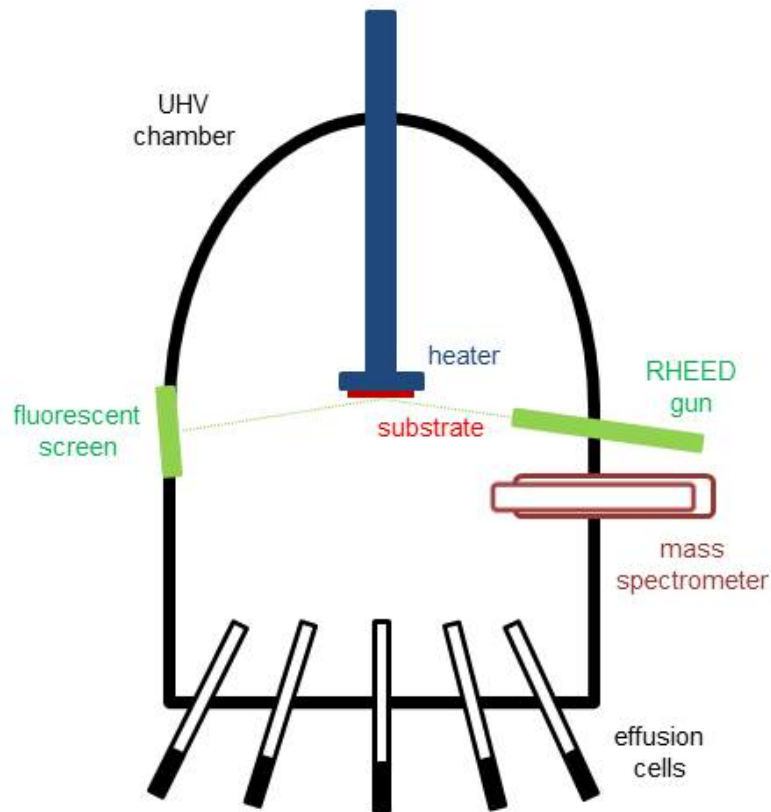
The deposition of the thin films via PLD takes place in a UHV chamber with a base pressure of less than  $10^{-8}$  mbar to avoid a contamination with oxygen and other elements. The PLD chamber is equipped with a Reflection High Energy Electron Diffraction (RHEED) system (see Chapter 2.3), pressure sensors, a substrate manipulator with a substrate heater, a target manipulator, a mass spectrometer, and a pyrometer to ensure a proper control of all necessary parameters (see Fig. 2.1). In addition, two membrane pumps and two turbo molecular pumps are installed to ensure UHV conditions. During the process, a highly energetic laser beam hits the target (cylindrically shaped bulk material with a diameter of around 10 mm) which in this case is Co-doped Ba-122 [79, 96]. The used laser is a KrF excimer laser (Lambda-Physics LPX 305i) with a pulse duration of 20 to 50 ns and a laser energy of around 2-5 mJ (measured with an energy monitor installed at the chamber). It is possible to change the repetition rate of the laser pulses from 1 Hz to effectively 20 Hz. Using a lens, the laser beam is focussed in front of the target which is necessary to ensure a homogeneous energy distribution over the target surface. Focussing the laser beam onto the target would lead to droplets and the destruction of the target [97]. The pulsed laser is absorbed by the surface of the target material heating it up to very high temperatures (about 10000 °C). The material evaporates into a plasma plume which is directed to the heated substrate. The highly energetic material (energies of the ions up to 100 eV [98]) condenses onto the rotating substrate, leading to the formation of the thin film. The growth process can be monitored by a RHEED system to ensure the epitaxial growth with a smooth surface.



**Figure 2.1:** The principle working mechanism and layout of a PLD chamber [99].

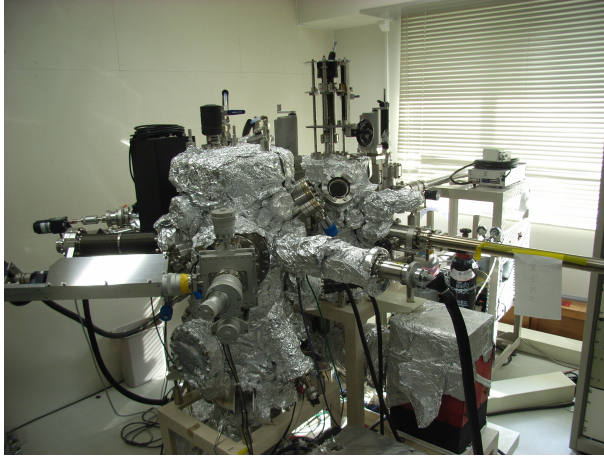
## 2.2 Molecular beam epitaxy (MBE)

Molecular beam epitaxy (MBE) is a technique for growing epitaxial thin films by using molecular or atomic flux beams from heated solid sources interacting with the heated substrate. Placed in evaporation cells, the solid sources provide an angular distribution of the atoms and molecules along the flux beam. A schematic view of an MBE chamber is shown in Fig. 2.2.

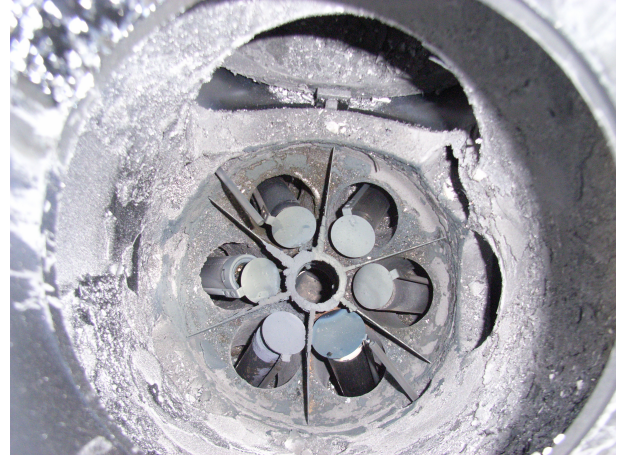


**Figure 2.2:** A simple sketch showing the main components of the deposition chamber in an MBE system. The effusion cells contain the solid sources which differ depending on the film to be grown.

Certain beam conditions should be fulfilled. The mean free path  $l$  of the beam particles should be longer than the size of the chamber. Therefore, the total pressure in the chamber should not exceed approximately  $10^{-5}$  mbar. Hence, ultra high vacuum (UHV) conditions are essential for the growth of thin films by MBE, which means that the rate of beam flux has to be controlled carefully. The chosen crucibles are made of pyrolytic boron nitride ( $\text{Al}_2\text{O}_3$  in case of the Fe cell because of lower reactivity) characterised by a low rate of gas evolution as well as chemical stability up to  $1400^\circ\text{C}$ . Other materials used for crucible materials in the MBE chamber are molybdenum and tantalum. Regarding the solid sources, only ultrapure materials should be used. The control of composition and doping is done by either changing the effusion cell temperature or by opening and closing the mechanical shutters of the cells. In-situ monitoring of the film growth is provided by a RHEED system that can give information about film thickness (RHEED oscillations of the intensity), surface status, and development (RHEED diffraction patterns).



**Figure 2.3:** Front view of the MBE chamber for the thin film growth of P-doped Ba-122 (Nagoya, Japan).



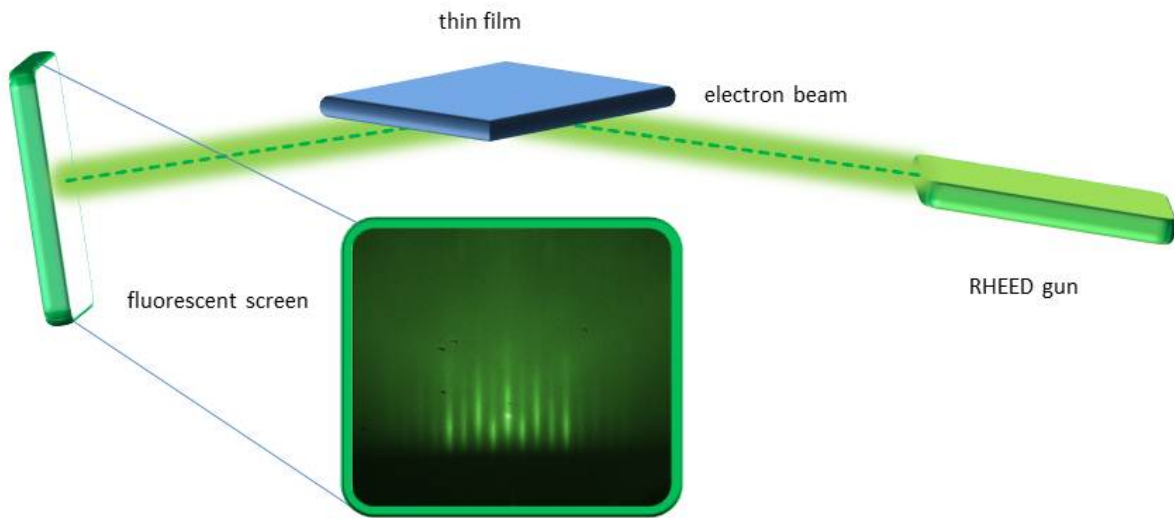
**Figure 2.4:** Top view of the MBE chamber (Nagoya). The effusion cells are located in a round ordering, covered by the shutters. The chamber walls are coated by precipitations from the growth process.

## 2.3 Reflection high energy electron diffraction (RHEED)

The RHEED instrument is usually located perpendicular to the film growth direction as can be seen in Figs. 2.1, 2.2 and 2.5. A voltage of 15 kV accelerates the electrons emitted from a tungsten filament. These electrons hit the growing film at very small angles (about  $2^\circ$ ) and are deflected onto a screen depending on the film surface. Just the first atomic layers will account to the scattering of the electrons because of the small penetration depth of the RHEED beam. Like all electron diffraction techniques, the reflected beam can satisfy the Bragg equation  $n\lambda = 2d \sin\theta$  and obeys the Laue conditions [54]. A video is taken with a CCD camera and analysed. The distance, the shape, as well as the intensity of the reflections may provide information about the film growth, the layer thickness and the crystal structure. In this work, RHEED pictures are taken for monitoring the film growth regarding epitaxy and surface roughness.

The diffraction process in the RHEED system can be described as non-true, i.e. the electron beam is leaving the thin film at another position than where the incident beam had entered. The reflected beam and therefore the diffraction pattern is obtained due to the transmission of the beam through the upper surface and its irregularities. For a true diffraction beam, the pattern exhibits spot like features (see Fig. 2.6a), while in the case of a perfectly flat surface, the pattern shows streaks (see Fig. 2.6b). This can be explained

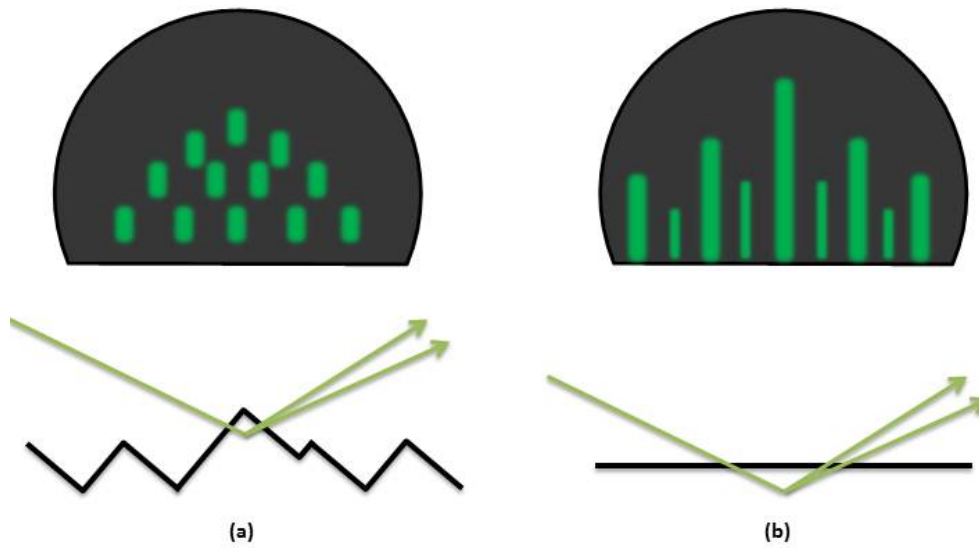




**Figure 2.5:** The principle working mechanism of a RHEED instrument. A typical RHEED picture for a Co-doped Ba-122 thin film revealing long stripes as reflections demonstrating a high quality surface is shown on the screen.

by the missing third dimension in real space, in case of a perfectly flat surface. Therefore, the pattern shows streaks perpendicular to the shadow edge of the reflecting surface. All these effects and patterns should be relativised when considering thermal vibrations and imperfections of the surface.

Another effect observed in the RHEED monitor is the surface reconstruction of the upper layer of the growing thin film. A surface reconstruction is a stronger change of the symmetry of the top layer where atoms reorder in a different periodicity; even a rotation of the new surface mesh is possible. This reconstructed surface produces a reciprocal lattice different from the normal one and can be examined using Low-Energy Electron Diffraction (LEED) where the incident beam is normal to the film surface. Due to its geometry, LEED is not applicable for the use in PLD or MBE, but can be applied for postgrowth characterisation. Nevertheless, these reconstructions can be observed via RHEED as well and are visible in a changed streak pattern on the fluorescent screen [54]. Figure 2.5 shows the principle working mechanism of a RHEED instrument, the RHEED picture which is shown reveals smaller streaks between longer streaks because of different mesh symmetries in the surface reconstruction of the Co-doped Ba-122.



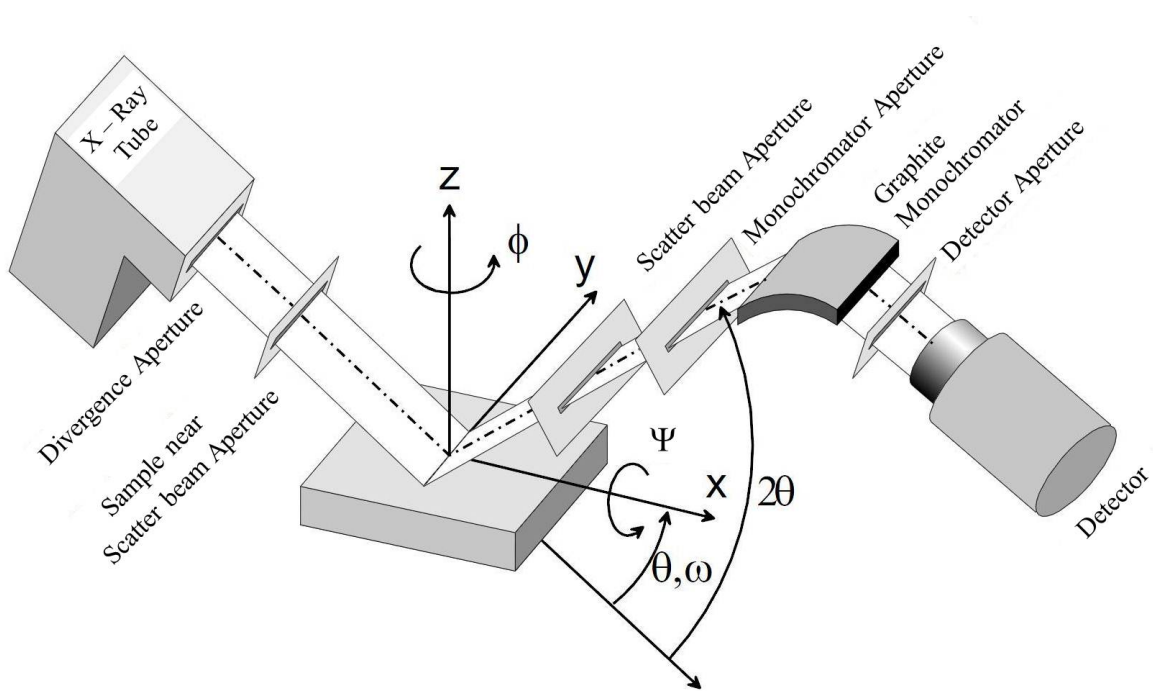
**Figure 2.6:** Modes of RHEED diffraction mechanisms. (a) Transmitting reflection for a more rough surface resulting in a spotty RHEED pattern. (b) Reflection pattern for a flat surface with a streak like shape on the fluorescent screen. The smaller streaks in the pattern indicate surface reconstruction.

## 2.4 Structural characterisation by X-ray diffraction

X-ray diffraction (XRD) may be used to investigate the orientation and the phases of thin films. The diffraction of X-ray beams on ordered structures is used with the Bragg-condition:  $n \times \lambda = 2d \sin(\theta)$  where  $n$  is an integer defined by the order of the diffraction, and  $\theta$  is the deflection angle. Therefore, the lattice distance  $d$  can be calculated. In this work a *Bruker D8 Advance Diffractometer* using monochromatic  $\text{Co-K}\alpha_{1,2}$  radiation ( $\lambda_{\text{Co-K}\alpha} = 0.17889 \text{ nm}$ ) was used for the  $\theta$ - $2\theta$  investigations and the *Philips X'Pert Diffractometer* (monochromatic  $\text{Cu-K}\alpha_{1,2}$  radiation with  $\lambda_{\text{Cu-K}\alpha} = 0.15406 \text{ nm}$ ) was used for the texture investigations.

**$\theta$ - $2\theta$  investigations.** For the  $\theta$ - $2\theta$  geometry, only reflections from lattice planes oriented parallel to the surface are visible. Figure 2.7 presents the schematic view of an X-ray device.  $\phi$  describes the rotation around the  $z$ -axis,  $\Psi$  the rotation around the  $x$ -axis and  $\theta$  marks the deflection of the reflecting beam with respect to the  $x$ -axis.

**Nelson-Riley-function.** From the positions of the reflections of the  $\theta$ - $2\theta$  scan, it is possible to extract the  $c$ -axis lattice parameter using the  $(00l)$  reflections and the Nelson-Riley-function (2.1) [101]:

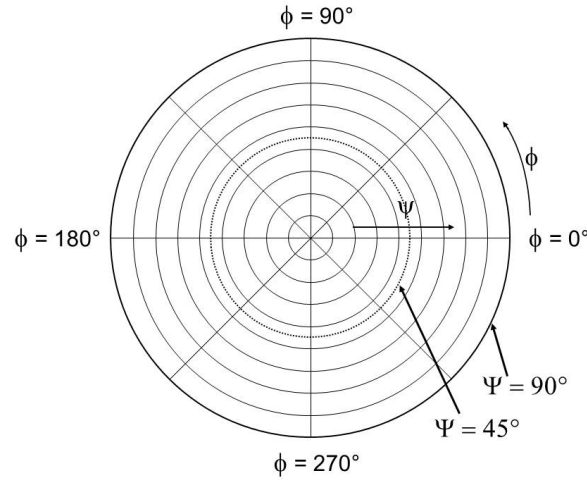


**Figure 2.7:** Setting of an X-ray device [100].

$$f(\theta) = \frac{\cos^2 \theta}{\sin \theta} + \frac{\cos^2 \theta}{\theta} \quad (2.1)$$

The  $c$ -axis is calculated as if an infinite number of planes would be measured by plotting  $c$  over  $f(\theta)$ . Hereby, two systematic errors that might happen during the sample mounting are avoided: the displacement of the sample from the diffraction axis and the vertical divergence of the incoming beam. The samples in this work have been measured using a step size of  $0.02^\circ$  and a scanning speed of  $0.013^\circ/\text{s}$ .

**Texture measurement.** To check epitaxy of the thin film, it is necessary to investigate the in-plan orientation of the crystals by measuring the pole figure and the  $\phi$ -scan of the film. Thereby, it is checked that no misoriented grains appear in the crystal structure.



**Figure 2.8:** Schematic pole figure.

A scan along the  $\phi$  angle will give information about the existence of rotated grains in the layer system. Fixing the afore investigated angles  $\theta$  and  $\Psi$ , a full rotation will be measured to check if there are any grains giving interference maxima for other  $\phi$  orientations. A further step constitutes the measurement of the pole figure where this kind of  $\phi$  scan will be done for every  $\Psi$  angles from  $0^\circ$  to  $85^\circ$ . This measurement will give information about the existence of rotated grains of this material phase in the film.

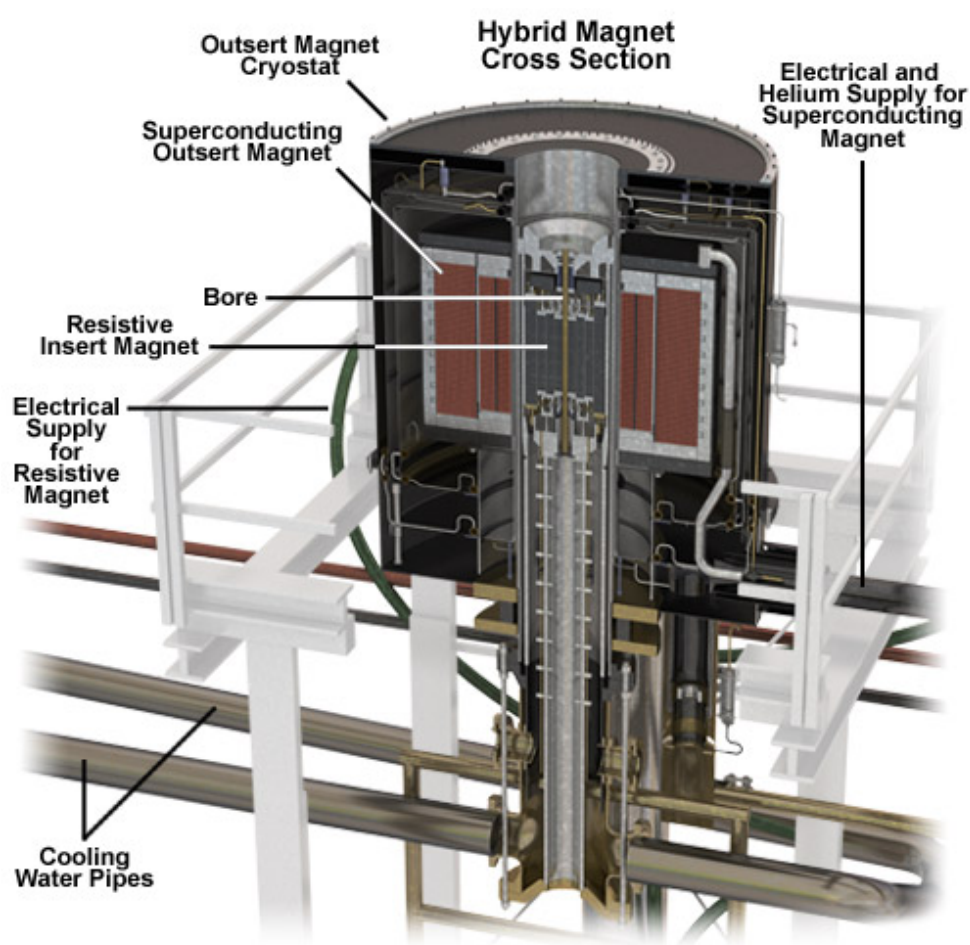
## 2.5 Transport measurements

A basic measurement to ensure a suitable sample for further investigations is the resistivity measurement and has been done for all thin films by a Physical Properties Measurement System (PPMS) from 300 K to below the superconducting transition,  $T_c$ . This was achieved by a four-point contact measurement. For  $J_c$  investigations, a small bridge is patterned onto the thin films to ensure a definite electric current path. This was done by laser cutting in the Applied Superconductivity Center (ASC) in Tallahassee, USA.

The SmFeAs(O,F) thin films were measured in the dc 45 T hybrid magnet of the National High Field Magnet Laboratory (NHMFL), Tallahassee, USA. The magnetic field is generated by a superconducting magnet providing a background field of 11.5 T and a combined dc magnet coil of 33.5 T (see Fig. 2.9) with a full load power usage of 30 MW and a bore diameter of 32 mm.

The P-doped Ba-122 and the Nd-1111 thin films have been measured in a dc 35 T magnet

at the NHMFL as well. In this case, the full load power usage is around 22.5 MW, the bore diameter is 32 mm. In all measurements the used cryostat was a Janis Bath Cryostat (model CNDT). For the rotator we used a double wall He<sub>3</sub> vacuum can to gain better temperature control during the resistivity measurement. The rotator was equipped with a self-made heater which was located directly below the sample to ensure the best possible heat flow control. The temperature dependent measurements of the field dependence of the  $J_c$  has been done in a 16 T PPMS system in the ASC at Tallahassee.



**Figure 2.9:** A schematic cut through the hybrid magnet (superconducting magnet + dc magnet) in the NHMFL, Tallahassee, USA. The sample is located at the centre of the bore experiencing a homogeneous field of up to 45 T [102].

## 2.6 Transmission electron microscopy (TEM)

For the detailed investigation of the local microstructure of thin films, transmission electron microscopy (TEM) offers a deep insight [103]. Unlike RHEED, which is an in-situ analysis

of the thin film surface and, therefore, of the growth process, TEM provides information about the whole film cross section. Also, XRD measurements only give integral information of the film depth. Due to the small de Broglie wavelength of electrons, the resolution of the TEM is much better compared to optical measurements, not only the wave but also the particle nature of the electrons is used.

The analysis of thin films via TEM is done using a thin lamella cut out of a thin film using a focussed ion beam (so-called FIB-cut). This lamella (thickness about 100 nm) is transferred into an UHV chamber and rayed and scanned by a coherent focussed electron beam. The transmitting electrons will be imaged onto a fluorescent screen or captured by a CCD camera (charge-coupled device, CCD). The imaging is the result of different effects, like the contrast in mass-thickness (electrons are scattered differently due to the different thickness of the specimen,) and the scattering contrast (due to different crystal orientations). Therefore, by adjusting the aperture, it is possible to get bright-field and dark-field contrasts, depending on whether the image is generated by the primary beam (transmitting beam) or, when filtering the primary beam, by the diffracted beam, respectively. Other measurements, like the analysis of elements through electron dispersive X-ray analysis and the usage of X-ray devices in locally focussed areas can be combined with these measurements and indeed have been done for the elemental analysis of the SmFeAs(O,F) thin films presented in Chapter 5.

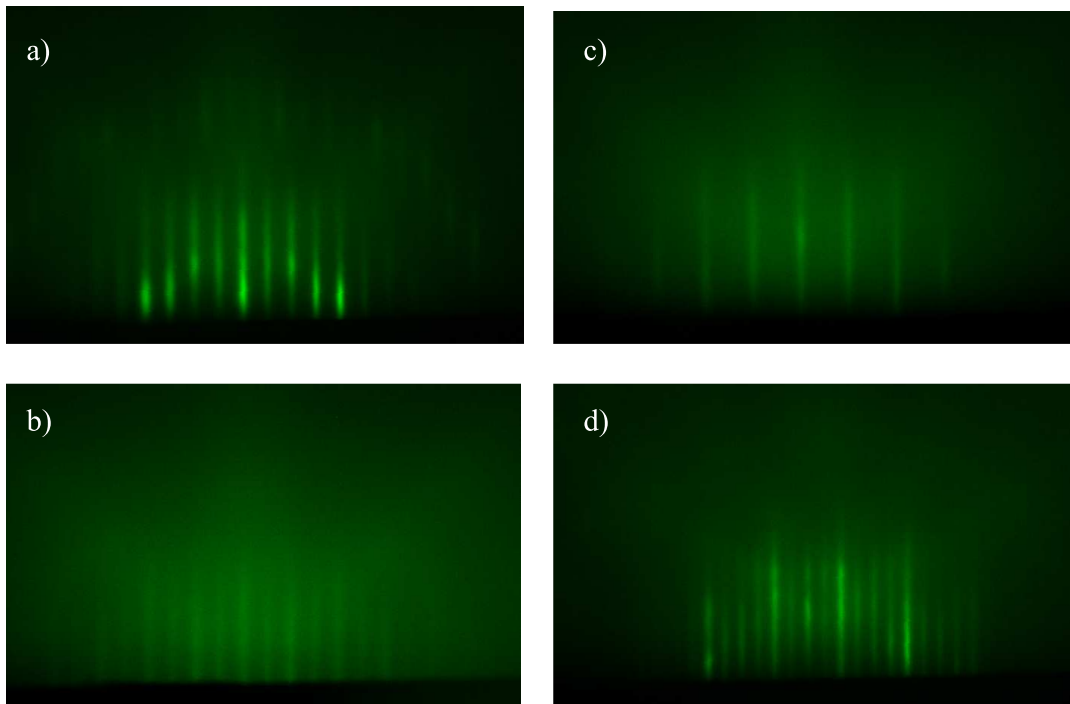
# 3 Versatile substrates for Fe-based superconducting thin films

## 3.1 Scientific problems

Since the discovery of superconductivity in K-doped  $\text{BaFe}_2\text{As}_2$  (Ba-122), [38] many efforts have been made to investigate the physical properties and to understand the physics in these superconducting materials. Compared to single crystals, thin films are suitable for investigating transport and/or optical properties due to their dimensionality. Additionally, thin films are favourable for superconducting electronics applications. The symmetry of the superconducting order parameter has been investigated by means of hybrid Josephson junctions using Co-doped Ba-122 thin films realising S'NS-type Josephson junctions (S': conventional superconductors, such as Nb or Pb, N: normal conductors, S: FBS) as well as SQUIDs using bicrystal junctions [104] [105–107].

Many groups have prepared  $A\text{EFe}_2\text{As}_2$  thin films ( $A\text{E}$ : alkali earth elements, Ca, Sr and Ba) of the so-called "122" family by means of PLD and MBE [69, 71, 83–85, 108, 109] [74]. Thersleff *et al.* proposed the usage of Fe as a buffer layer on a MgO (001) substrate for growing Co-doped Ba-122 thin films, which yields high crystalline quality as well as improved superconducting properties under the used deposition conditions [76].

However, the Fe buffer implies some disadvantages such as the shunting of the current in the normal state which necessitates a recalculation of the superconducting transition temperature,  $T_c$  [110]. Additionally, measurements of the normal state properties are always hindered by the Fe buffer layer. For instance, the parent compound of Ba-122 has shown a spin density wave anomaly in  $R(T)$  curves at around 140 K [111]. However, this transition is hardly recognised in the corresponding thin films on Fe/MgO. Furthermore, the intrinsic physical properties may be influenced by ferromagnetic Fe or FeCo buffer layers, which is a current topic of investigation [112]. Another significant influence of the Fe buffer which leads to off-stoichiometry of the films is Co diffusion from the film into the Fe buffer layer resulting in a Co-gradient over the Ba-122 layer [79]. In order to avoid such problems without compromising crystalline quality and superconducting properties,



**Figure 3.1:** RHEED images of the in-situ growth of the Co-doped Ba-122 phase on (a)  $\text{CaF}_2$  (001), (b)  $\text{SrF}_2$  (001), (c)  $\text{BaF}_2$  (001) and (d) Fe-buffered  $\text{MgO}$  (001) substrates. The pictures were taken after the deposition. The incident electron beam is along the substrates [110] azimuth.

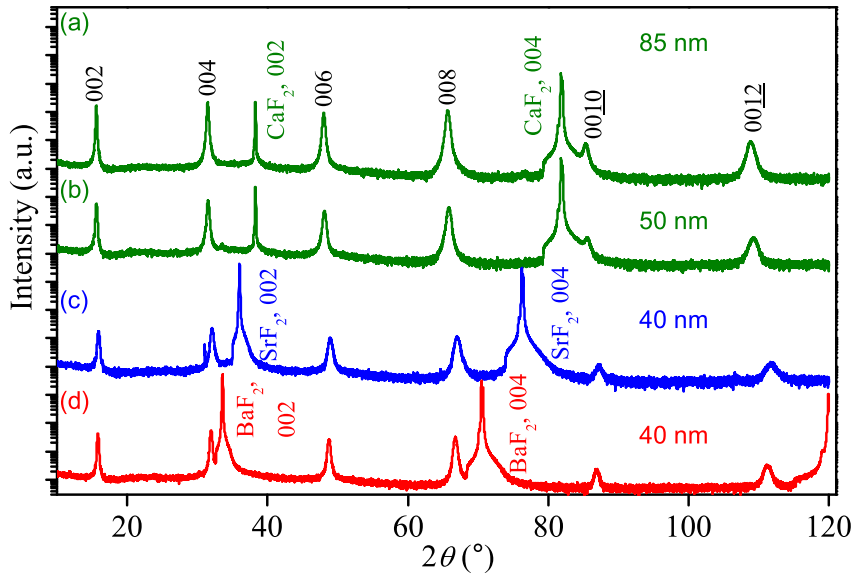


new types of substrates should be explored.

Recently, epitaxial Fe(Se,Te) thin films as well as  $REFeAs(O,F)$  ( $RE$ : Nd and Sm) thin films have been prepared on  $CaF_2$  (001) substrates by PLD and MBE, respectively [65,94,113]. These films show high crystalline quality as well as good superconducting properties. Hence, fluorides may be versatile substrates for Fe-based superconducting thin films. Here, the epitaxial growth of Co-doped Ba-122 on various fluoride substrates is demonstrated and the influence of substrate materials on the structural and superconducting properties is discussed.

### 3.2 Employing fluoride substrates

For the deposition process, a  $BaFe_{1.84}Co_{0.16}As_2$  bulk target prepared by a solid-state-reaction was used (onset  $T_c = 23.7$  K, measured by magnetisation method). The phase purity of the target material was studied by powder XRD in Bragg-Brentano geometry (Co- $K_\alpha$  radiation with  $\lambda = 1.7889$  Å), showing high phase purity. The detailed preparation procedure and analysis of the target material was described by Kurth *et al.* [79,114].



**Figure 3.2:**  $\theta - 2\theta$  scans for the Ba-122 thin films deposited on (a), (b)  $CaF_2$  (001), (c)  $SrF_2$  (001) and (d)  $BaF_2$  (001) substrates, respectively. A weak  $BaF_2$  (002) reflection appears in the film deposited on  $CaF_2$  and  $SrF_2$ .

The fluoride substrates were cleaned in an ultrasonic bath using acetone and isopropanol and were subsequently transferred into the ultra high vacuum chamber (base pressure

$10^{-9}$  mbar). Co-doped Ba-122 layers were deposited using a KrF excimer laser ( $\lambda = 248$  nm, pulse duration = 25 ns) at a frequency of 7 Hz with an energy density of around  $2.5$  J/cm<sup>2</sup> on (001)  $AEF_2$  ( $AE$ : Ca, Sr and Ba) single crystalline substrates. The samples investigated in this chapter are summarised in Table 3.1.

**Table 3.1:** Deposition temperature and layer thickness of the Co-doped Ba-122 thin films.

Substrate	Deposition temp.	Layer thickness
CaF <sub>2</sub>	750 °C	85 nm
CaF <sub>2</sub>	700 °C	50 nm
SrF <sub>2</sub>	700 °C	40 nm
BaF <sub>2</sub>	700 °C	40 nm

The deposition process was monitored in-situ by a Reflection High Energy Electron Diffraction (RHEED) system. In all cases, streak-like patterns were observed during film growth pointing to an epitaxial growth with low surface roughness (see Fig. 3.1). The observation of additional streaks between the main streaks indicates the formation of superstructure during the growth of the Co-doped Ba-122 on CaF<sub>2</sub> and SrF<sub>2</sub>, i.e. surface reconstruction that is also observed in single crystals (Fig. 3.1a and b) [115]. These RHEED patterns are very similar to Co-doped Ba-122 thin films grown on Fe buffered MgO (Fig. 3.1d) [116]. However, despite the observation of streaks, for Co-doped Ba-122 on BaF<sub>2</sub>, no signs of superstructures were observed due to a relatively large misfit of -10.6% (Fig. 3.1c).

### 3.3 Structural properties of Co-doped Ba-122

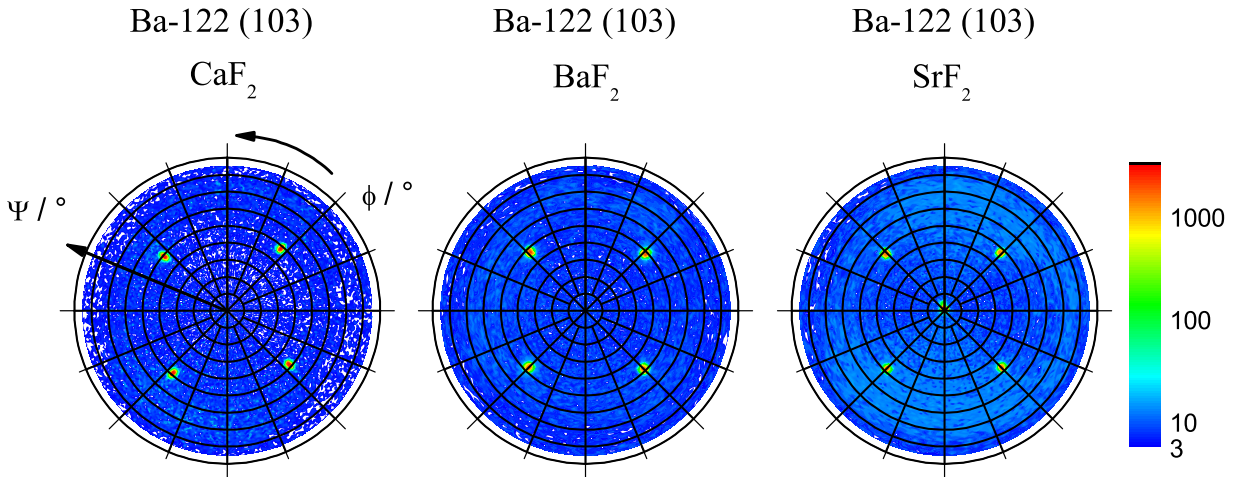
The phase purity of the thin films was confirmed by XRD (see Fig. 3.2). The scans obtained in Bragg-Brentano geometry showed no additional reflections of other phases except for the films deposited on CaF<sub>2</sub> and SrF<sub>2</sub>, where a small peak at  $2\theta = 33.6^\circ$  is visible, which can be assigned to the (002) plane of BaF<sub>2</sub>. The origin of this reflection will be discussed below.

The determination of the epitaxial relationship between films and the substrates was conducted by XRD texture measurements. The poles of the (103) and (202) planes have been used for Co-doped Ba-122 and fluoride substrates, respectively. All films showed a clear fourfold symmetry without any additional peaks. The pole figures of the Ba-122 (103) reflection are shown in Fig. 3.3. The corresponding  $\phi$ -scan of Co-doped Ba-122

and substrates are displayed in Fig.3.4. The basal plane of the Ba-122 film is rotated by  $45^\circ$  with respect to the substrate. Accordingly, the films are grown epitaxially with the relation  $(001)[110]\text{Ba-122}||(\text{001})[100]AEF_2$ . The average full width half maximum (FWHM) values,  $\Delta\phi$ , of films grown on  $\text{CaF}_2$ ,  $\text{SrF}_2$  and  $\text{BaF}_2$  are  $1.31^\circ$ ,  $1.41^\circ$  and  $1.62^\circ$ , respectively. Values were not corrected for device broadening. We assume that the large lattice misfit (Table 3.2) leads to a relatively large  $\Delta\phi$  value. Measurements of the thicker film (85 nm) of Co-doped Ba-122 on  $\text{CaF}_2$  showed an even higher crystalline quality with a  $\Delta\phi$  value of  $0.95^\circ$ , which is almost the same value of layers grown on Fe-buffered MgO [116].

**Table 3.2:** Lattice parameters and misfit data of the Ba-122 on different substrates.

Substrate	Substrate	Thin film		Misfit in
	<i>a</i> -axis	<i>a</i> -axis	<i>c</i> -axis	<i>a</i> -axis
$\text{CaF}_2$	5.451 Å	3.89 Å	13.19 Å	+2.7 %
$\text{CaF}_2$	5.451 Å	3.91 Å	13.17 Å	+2.7 %
$\text{SrF}_2$	5.799 Å	3.94 Å	12.97 Å	-3.2 %
$\text{BaF}_2$	6.196 Å	3.96 Å	13.02 Å	-10.6 %



**Figure 3.3:** Pole figures of the (103) reflection of Co-doped Ba-122 for the films grown on (a)  $\text{CaF}_2$ , (b)  $\text{BaF}_2$  and (c)  $\text{SrF}_2$ . A clear fourfold symmetry is visible without any rotated grains. The diffraction intensity unit for texture measurements is cps.

As stated earlier, Co-doped Ba-122 films have been grown with an in-plane rotation of  $45^\circ$  with respect to the substrates. Therefore, the lattice misfit between film and substrate is defined as  $((a_{\text{film}} \times \sqrt{2}) - a_{\text{substrate}}) / (a_{\text{film}} \times \sqrt{2})$ . In this calculation, the lattice parameter  $a_{\text{film}} = 3.96 \text{ \AA}$  of the bulk material (i.e. PLD target) was used. In Table 3.2, the in-plane and out-of-plane lattice parameters of Co-doped Ba-122 evaluated through high-resolution reciprocal space maps (RSM) are also summarised. The out-of-plane lattice parameters

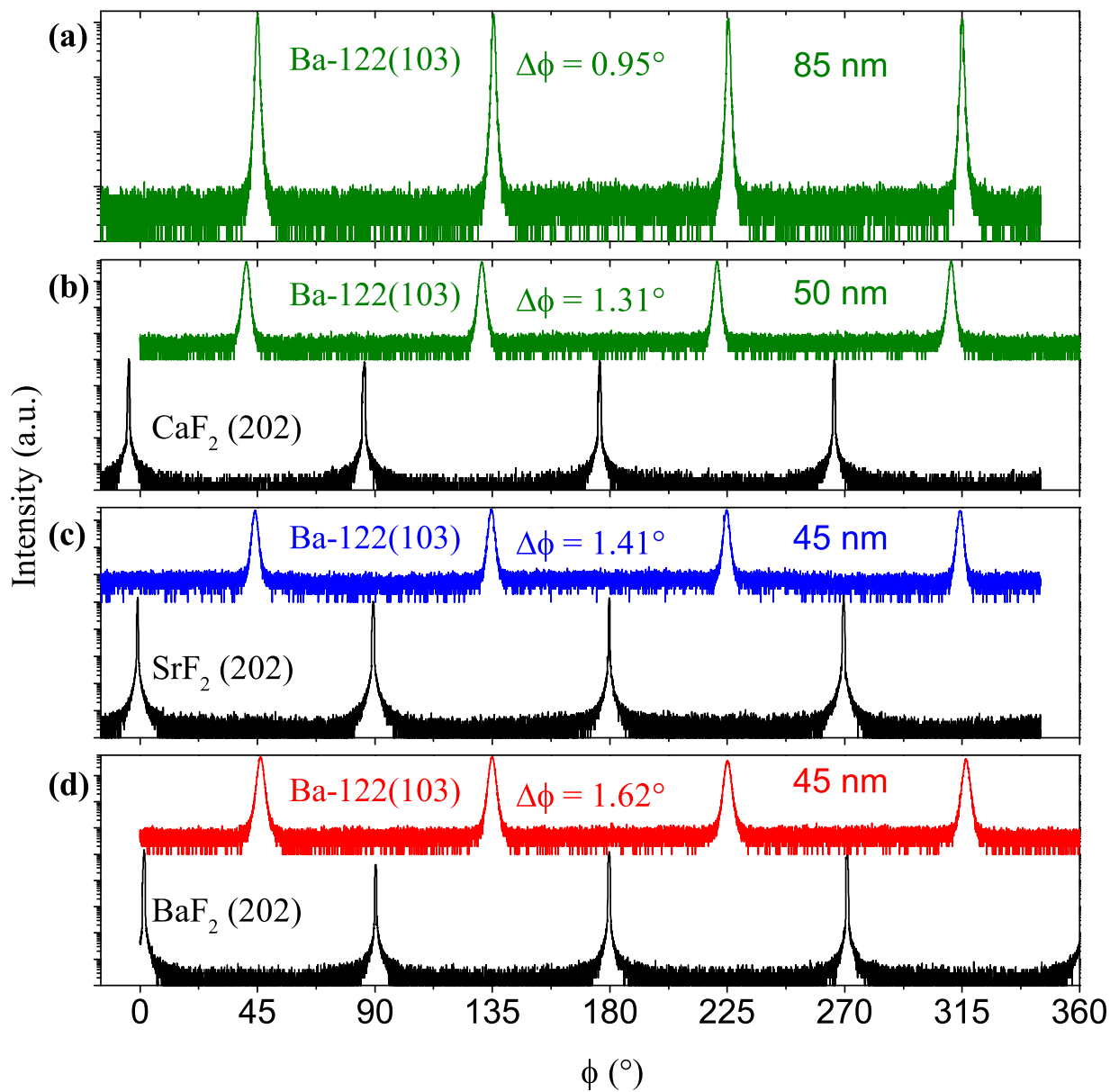
evaluated by the Nelson Riley extrapolation from  $\theta - 2\theta$  scans are in good agreement with the values of the RSM measurements. Clearly, negative misfit values of films on  $\text{SrF}_2$  and  $\text{BaF}_2$  lead to a slightly larger in-plane lattice parameter compared to films on  $\text{CaF}_2$ . However, the change in lattice parameter  $a$  is small despite a large misfit, in particular with the  $\text{BaF}_2$  substrate, whereas a significant change in lattice parameter  $c$  is observed. Additionally, a reaction layer between Co-doped Ba-122 and substrates is observed, which will be discussed later. Hence, such a change in lattice parameters cannot be explained by the simple misfit scenario indicative of another mechanism such as F intercalation into the Co-doped Ba-122 lattice. Possible diffusion of F from the fluoride substrate has been discussed in both the  $\text{SmFeAs}(\text{O},\text{F})$  and the  $\text{Fe}(\text{Se},\text{Te})$  system [117, 118].

TEM investigations of the films grown on  $\text{CaF}_2$  and  $\text{BaF}_2$  showed no appreciable defects in the Co-doped Ba-122 layers (Figs. 3.6 and 3.5). The respective film thickness on  $\text{CaF}_2$  and  $\text{BaF}_2$  substrates in Fig. 3.6 are 50 nm and 40 nm. For the film on  $\text{SrF}_2$ , a layer thickness of 40 nm was determined and the thicker film shown in Fig. 3.5 revealed a thickness of about 85 nm.

Microstructural investigations on a thicker film on  $\text{CaF}_2$  (i.e. better crystalline quality) by high-resolution TEM (HRTEM), high-resolution scanning TEM (HRSTEM), and electron energy loss spectroscopy (EELS) have also been conducted. Although a possible fluorine diffusion into the Co-doped Ba-122 has been discussed earlier, a trace of fluorine in the layer cannot be detected by EELS, presumably due to the high volatility of the fluorine under the influence of the electron beam. An interfacial layer (thickness  $\sim 10$  nm) between the Co-doped Ba-122 and the  $\text{CaF}_2$  substrate is clearly observed (Figs. 3.5 and 3.6a). A HRSTEM line scan over the interface with combined Ba detection using EELS revealed a small diffusion of Ba into the  $\text{CaF}_2$  substrate. As stated earlier, a small  $\text{BaF}_2$  signal was detected in  $\theta$ - $2\theta$  scans (Fig. 3.2). Accordingly, this reaction layer can be assumed to be  $\text{BaF}_2$ .

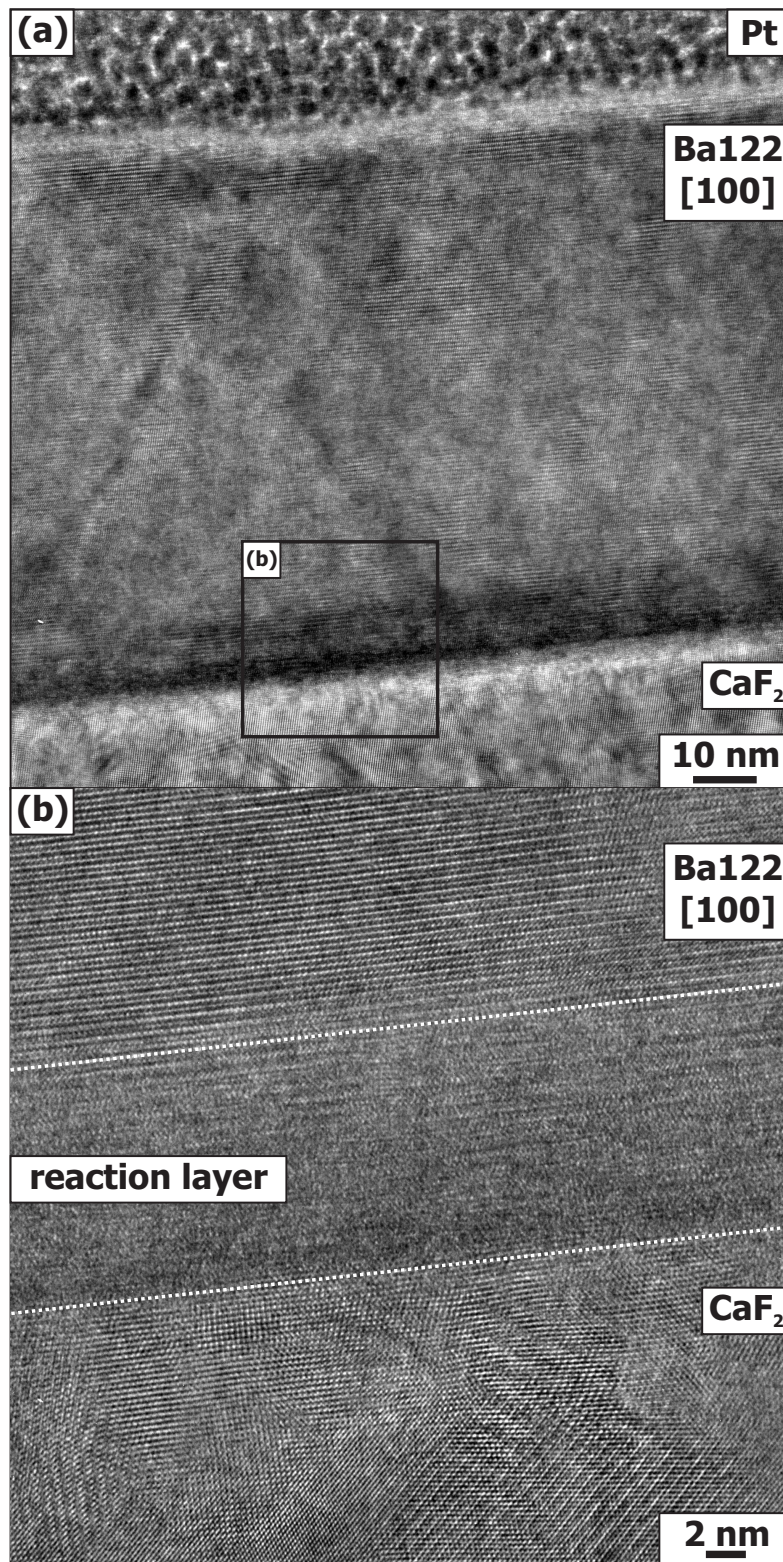
### 3.4 Superconducting properties of Co-doped Ba-122 grown on fluoride substrates

The  $T_{c,90}$  of the thin films, which is defined as 90% of the resistance in the normal state at 30 K, was determined through resistance measurements with a four-probe method using a PPMS (Fig. 3.7a). The film deposited on  $\text{BaF}_2$  shows a  $T_{c,90}$  of 21.4 K and the film on  $\text{SrF}_2$  shows 22.1 K, whereas the film deposited on  $\text{CaF}_2$  has the high value of 26.9 K. The highest

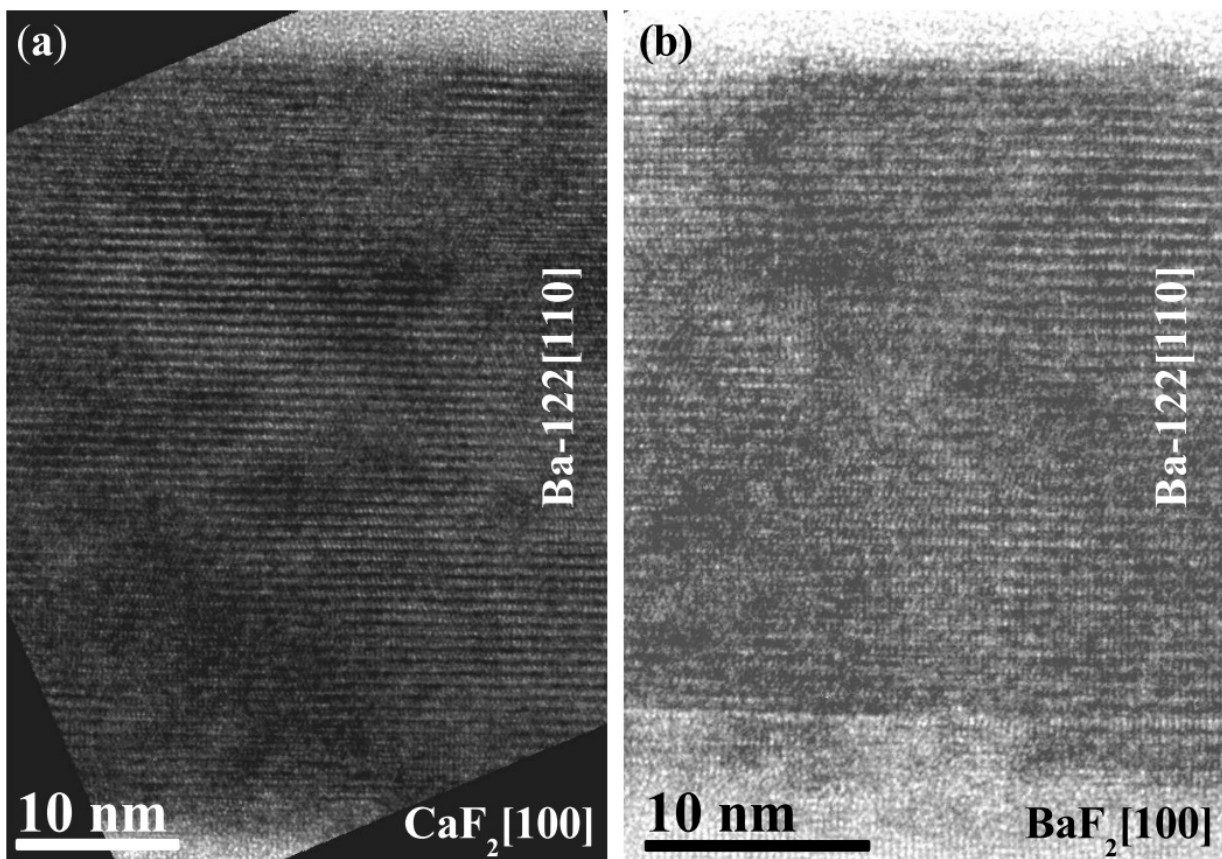


**Figure 3.4:**  $\phi$ -scans of the (103) reflection of the Ba-122 phase grown on (a), (b)  $\text{CaF}_2$ , (c)  $\text{SrF}_2$  and (d)  $\text{BaF}_2$  showing sharp reflections with a four-fold symmetry. No rotated grains are observed.

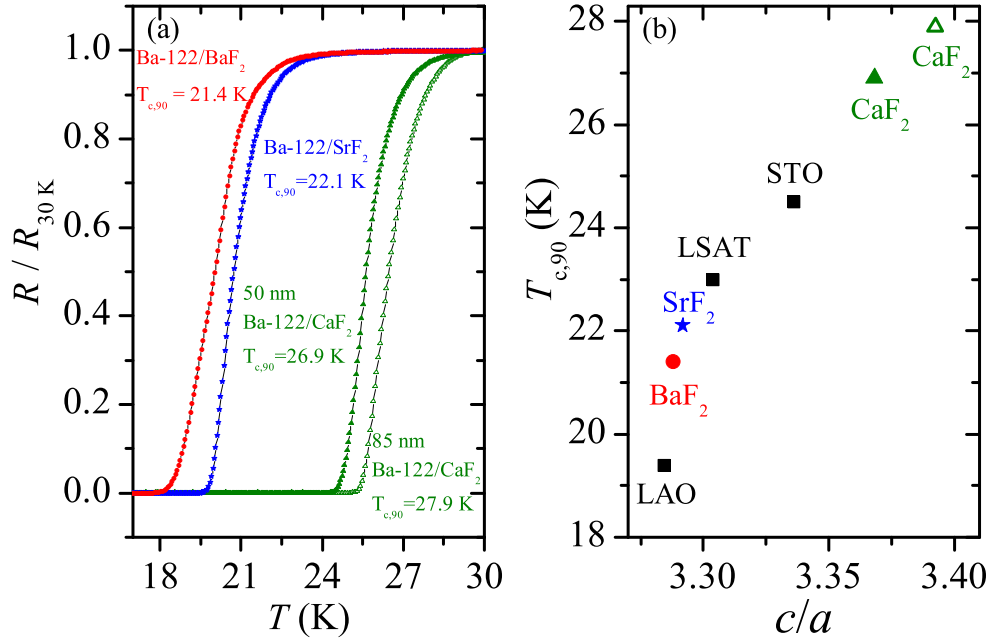




**Figure 3.5:** HRTEM investigations of the Ba-122 film (thickness about 85 nm) deposited on CaF<sub>2</sub> (a). A closer look at the Ba-122-CaF<sub>2</sub>-substrate interface (b) reveals a reaction layer which can be assumed to be BaF<sub>2</sub> due to XRD and EELS data.



**Figure 3.6:** TEM bright field picture of the (a) Ba-122/CaF<sub>2</sub> (thickness about 50 nm) and the (b) Ba-122/BaF<sub>2</sub> thin film (thickness about 40 nm) showing high structural quality of the Ba-122 layer. However, a reaction at the interface is observed.

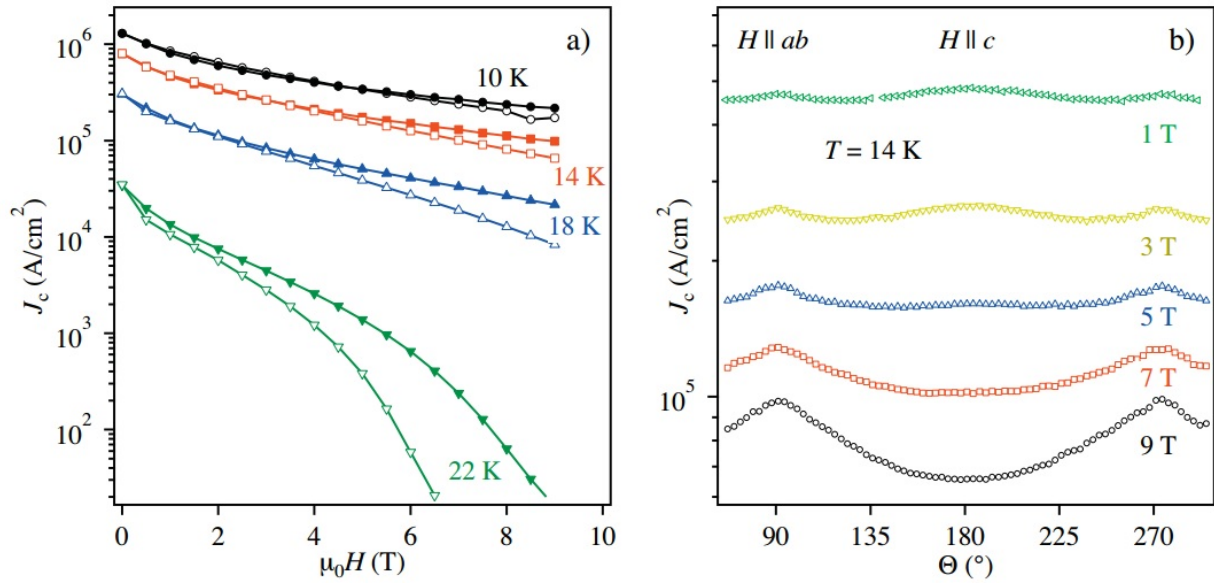


**Figure 3.7:** (a) Resistance measured curves for the Ba-122 deposited upon BaF<sub>2</sub> (red round), SrF<sub>2</sub> (blue star) and CaF<sub>2</sub> (green triangle).  $T_{c,90}$  is 21.4 K for the film deposited on BaF<sub>2</sub>, 22.1 K for the film on SrF<sub>2</sub>, 26.9 K on CaF<sub>2</sub> and 27.9 K for the thicker film on CaF<sub>2</sub> (green half-filled triangle). (b)  $T_{c,90}$  over  $c/a$  shows an almost linear dependence. The film with the highest  $c/a$  ratio shows the highest  $T_{c,90}$  (green half-filled triangle). The data from oxide substrates are also plotted on the same figure [74].

$T_c$  of over 28 K has been achieved in thick Co-doped Ba-122 on CaF<sub>2</sub>. Additionally, this film shows a high self-field critical current density ( $J_c$ ) of over 1 MA/cm<sup>2</sup> even at 10 K and a good in-field  $J_c$  performance, as shown in Fig. 3.8a [119]. Here, a criterion of 1  $\mu$ V/cm was used for evaluating  $J_c$ . In the angular-dependent  $J_c$  measurements, the magnetic field  $H$  was applied in the maximum Lorentz force configuration ( $H$  perpendicular to  $J$ ) at an angle of  $\theta$  measured from the  $c$ -axis.  $J_c$  is nearly isotropic at fields of 1 - 5 T, which can be seen in the angle dependence of  $J_c$  at 14 K, as well (Fig. 3.8b). Hence, fluoride substrates, in particular CaF<sub>2</sub> offer a clear benefit for growing epitaxial Co-doped Ba-122 with good crystalline quality and superconducting properties. Tarantini *et al.* showed that, especially for multilayer thin films, the  $J_c$  and the pinning force density ( $F_p$ ) can be improved immensely for films grown on CaF<sub>2</sub> compared to films grown on LSAT substrates. The increase of  $J_c$  and  $F_p$  after the multilayer deposition is more than 60% in the case of the growth on CaF<sub>2</sub> due to a change in the microstructure and a following different nature of the pinning centres [120].

Figure 3.7(b) shows the relationship between the  $T_c$  and the  $c/a$ . For comparison purposes, the films on various oxide substrates are also plotted in the same figure [74]. In





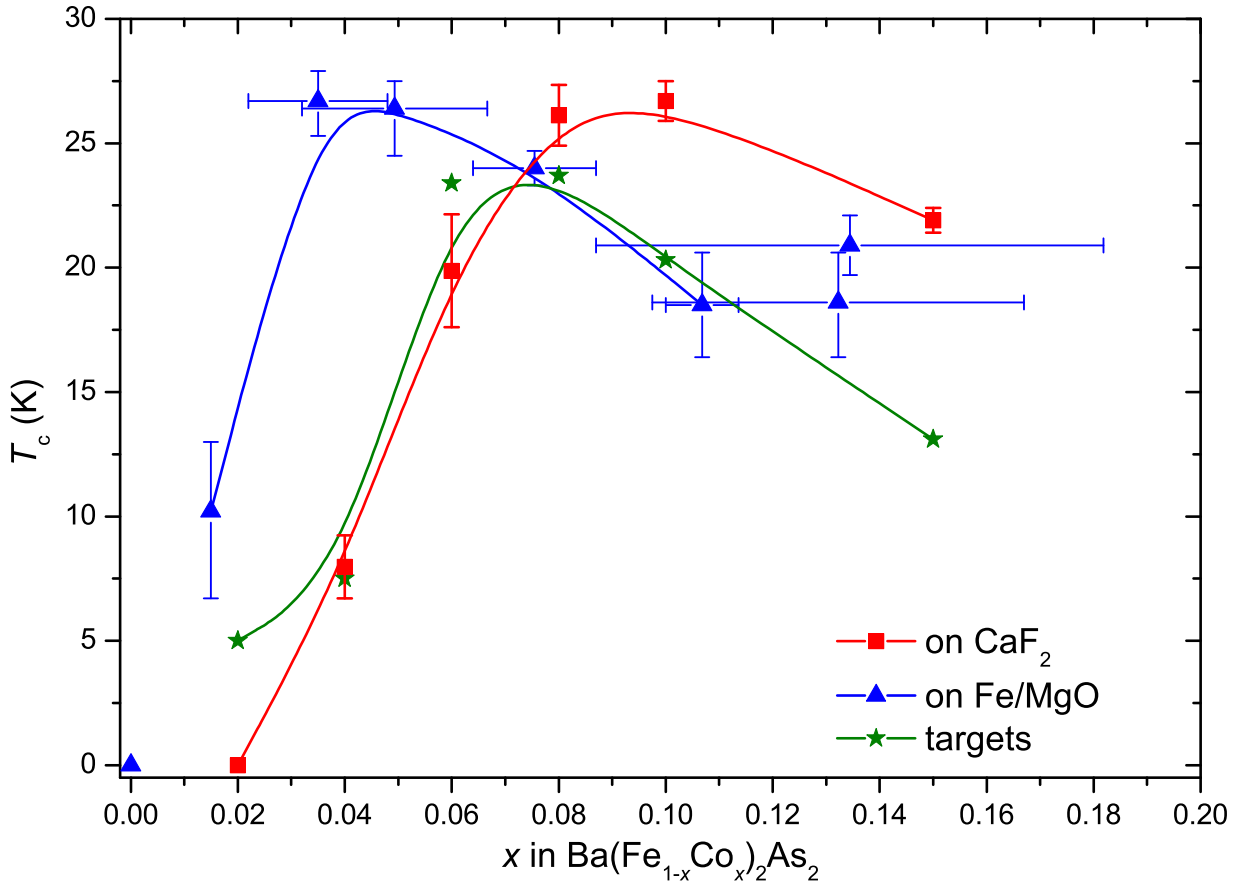
**Figure 3.8:** (a) Field dependence (up to 9 T) of  $J_c$  for Co-doped Ba-122 thin films grown on CaF<sub>2</sub> measured for various temperatures. The closed symbols represent the data measured in  $H \parallel ab$ , the open symbols mean  $H \parallel c$ . (b) Angle dependence of  $J_c$  in the presence of different magnetic fields measured at 14 K. A  $c$ -axis correlated peak is visible at lower magnetic fields vanishing above 5 T. The picture is taken from Ref. [119].

Fig. 3.7(b), an increase in  $T_c$  can be observed, with increasing  $c/a$ . Regarding the above results and also shown in Fig. 3.9, the lattice distortion clearly affects the superconducting properties. The origin of the trend of the  $c/a$  ratio needs further investigations. Figure 3.9 presents the doping phase diagram of Ba-122 films on CaF<sub>2</sub>. For comparison purposes, Ba-122 on Fe-buffered MgO (representing “on Fe/MgO” in Fig. 3.9) and the targets (polycrystalline materials) are also shown in the same figure [79]. It can be seen that the shift of the superconducting dome is immense. This can be related to the strain which is implemented by the substrate and has a similar effect on the superconducting properties like doping [46].

### 3.5 Summary of the chapter

Here, it can be emphasised that the crystalline quality of the thicker films grown on CaF<sub>2</sub> is identical, if not superior, to the films on Fe-buffered MgO. Additionally, several advantages over the use of Fe buffer layers are highly expected, such as no current shunting due to the Fe layer [110]. Most importantly, the stoichiometry of the Co-doped Ba-122 film, in particular the Co concentration, can be more stable, since Co diffusion into the Fe-buffer is avoidable.

To conclude, Co-doped Ba-122 thin films have been grown on various (001) fluoride substrates by PLD. Despite the presence of a possible  $\text{BaF}_2$  reaction layer, all films have been grown epitaxially with high crystalline quality. In particular, the crystalline quality of the Co-doped Ba-122 on the  $\text{CaF}_2$  substrate is almost identical and/or superior to that on Fe-buffered MgO substrates. The lattice distortion of the Co-doped Ba-122, which influences  $T_c$  significantly, is confirmed by RSM. The highest  $T_c$  of about 28 K with high and nearly anisotropic  $J_c$  has been achieved on  $\text{CaF}_2$ . Therefore, the  $\text{CaF}_2$  substrate offers a clear benefit for growing high-quality epitaxial Fe-based superconducting thin films and has already been used for junction fabrication, point-contact spectroscopy, and other investigations by many groups [119, 121–123].



**Figure 3.9:** Phase diagram of Co-doped Ba-122 for thin films grown on  $\text{CaF}_2$  [124], Fe buffered MgO and for the target material [79]. The shift of the phase diagram origins from the different strain states transferred from the substrates. The  $T_c$  of the films was determined via transport measurements as  $T_{c,90}$ , whereas the targets  $T_c$  was evaluated by magnetisation measurements (i.e. the onset of the signal). The Co content of the films on Fe/MgO was measured by Auger Electron Spectroscopy, whereas the corresponding values of the films on  $\text{CaF}_2$  and targets are nominal.

# 4 Unusually high critical current in clean P-doped $\text{BaFe}_2\text{As}_2$ single crystalline thin films

## 4.1 Scientific merit of P-doped Ba-122

Electron and hole-doped  $\text{BaFe}_2\text{As}_2$  (Ba-122) compounds show high upper critical fields with low anisotropy at low temperatures [125]. These properties are favourable for high-field applications, and, indeed, high-performance K-doped Ba-122 wires have been fabricated by a powder-in-tube technique [126,127]. Although the growth of partially oriented K-doped Ba-122 thin films prepared by a two-step process has been presented [83], in-situ K-doped Ba-122 thin films are difficult to accomplish due to the high vapour pressure of K. It has been reported that K-doped Ba-122 thin films were prepared by MBE; although the films are not stable in air [84]. On the other hand, isovalently P-doped Ba-122 thin films with a superconducting transition temperature ( $T_c$ ) of around 30 K, which is the second highest  $T_c$  in the Ba-122 family, have been fabricated by both PLD and MBE, where films prepared by the former method showed slightly lower  $T_c$  [86–88]. Additionally, bicrystal experiments revealed a high critical current density ( $J_c$ ) of around  $1 \text{ MA/cm}^2$ , even at a grain boundary angle as large as  $24^\circ$  at 4 K, [86] far beyond the superconducting properties of Co-doped Ba-122 [109,128] [129]. Hence, P-doped Ba-122 may be a good candidate for Ba-122 wire and tape applications. However, only properties at relatively low fields (up to 9 T) have been investigated so far. In order to use this material class for applications, the knowledge of in-field transport properties in a wide range of external fields and orientations needs to be extended. In this chapter, high-field (dc up to 35 T) transport properties of P-doped Ba-122 epitaxial thin films prepared by MBE are presented, and the feasibility of applications for this material class will be discussed.

**Table 4.1:** Growth parameters of P-doped Ba-122 thin films prepared by MBE

Sample		A	B
Substrate		MgO (001)	MgO (001)
Growth-time		60 min.	30 min.
Thickness		107 nm	45 nm
Growth-temp.		854 °C	847 °C
Cell-temp.	Ba	538.5 °C	403 °C
	Fe	1065 °C	1065 °C
	As	190 °C	186 °C
	GaP	703 °C	690 °C

## 4.2 MBE process of P-doped Ba-122

The P-doped Ba-122 thin films have a thickness of 107 nm and 45 nm, respectively, obtained from transmission electron microscopy (TEM), and were grown on a MgO (001) substrate by MBE [130]. The substrates were clamped to the holder with a thin indium layer in between to achieve high thermal conductivity from the heater. The substrates were thermally cleaned at 300 °C in the pre-chamber prior to the deposition. After cleaning, the substrate was transferred into the main chamber. All elements were supplied from Knudsen cells using solid sources: Ba, Fe, As, and GaP. P<sub>2</sub> flux was obtained from the GaP source, where Ga was eliminated by the use of two trapping pyrolytic boron nitride caps placed on the GaP cell [131]. A composition analysis of the thin films was done by Electron Probe Micro Analysis (EPMA) [132]. An accelerated electron beam was focused on the surface of the thin film with the help of electromagnetic lenses. The wavelength and intensity of the emerging X-rays were recorded to determine the stoichiometry. This measurement is highly sensitive because of its wave-dispersive nature and has a high spatial resolution, necessitating a measurement at different positions on the film to ensure homogeneity. When analysed, no Ga was detected in the film, proving an almost pure phosphorus flux. The relation of vapour pressure and cell temperature, which was obtained before using an ion gauge beam flux monitor, constitutes an important factor. By changing the cell temperature, the flux was adjusted and thereby the P content of the thin films was varied with a constant As vapour pressure and a variable vapour pressure of P. Due to its low sublimation point at around 615 °C, the excess As evaporates without being incorporated into the film. Therefore, an oversupply of As has no influence on the film stoichiometry. Similar methods have been used successfully in the past, for example for the preparation of GaAs thin films [133]. The growth conditions are summarised in Table 4.1.

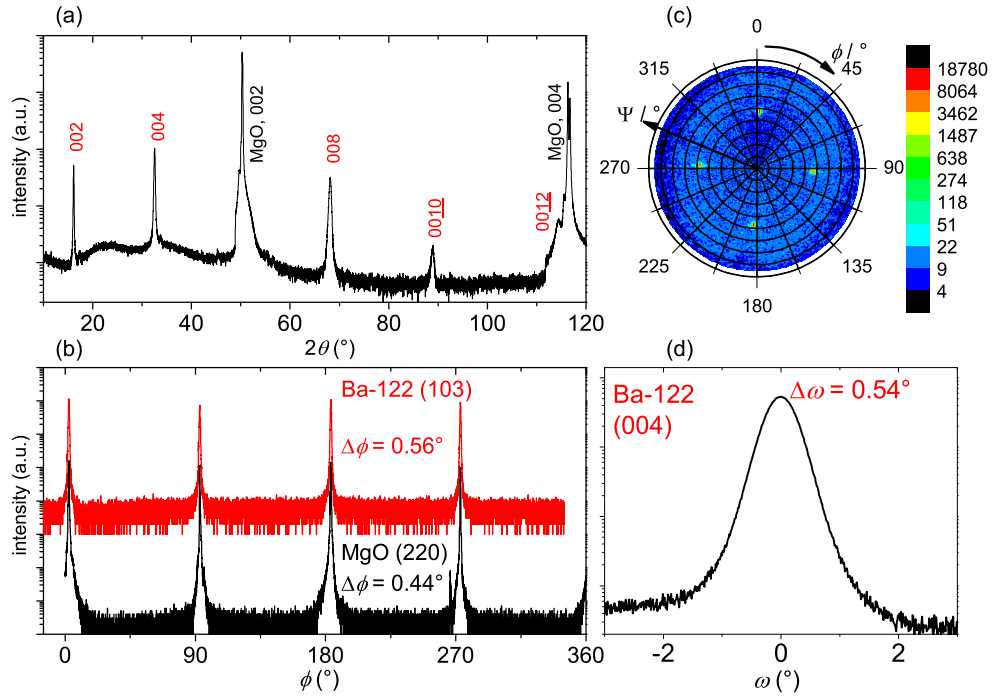
**Table 4.2:** Structural data and superconducting properties for films A and B

Sample		A	B
$\Delta\omega$ ( $^\circ$ )		0.54	0.74
$\Delta\phi$ ( $^\circ$ )		0.56	0.96
$c$ -axis ( $\text{\AA}$ )		12.78	12.77
Composition	Ba:Fe:(As+P)	1 : 1.92 : 1.93	1 : 2.09 : 2.09
	P-content	0.22	0.23
$T_{c,90}$ (K)		30.9	30.0
$J_{c,sf}$ at 4.2 K ( $\text{A}/\text{cm}^2$ )		6.3 M	8.5 M
$F_{p,max}$ at 4.2 K ( $\text{N}/\text{m}^3$ )	$\parallel ab$	77 G	125 G
	$\parallel c$	35 G	35 G
$\mu_0 H_{irr}$ at 4.2 K (T)	$\parallel ab$	71.2	66.5
	$\parallel c$	44.0	41.8

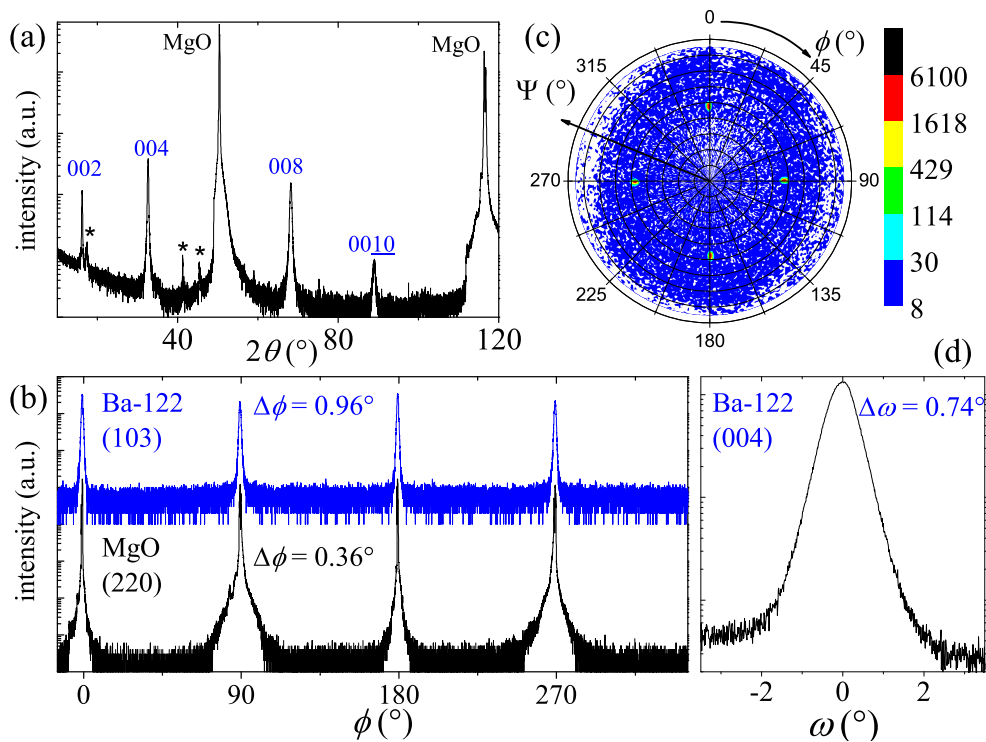
### 4.3 Structural properties and microstructure of P-doped Ba-122

The thin films are grown  $c$ -axis oriented with high phase purity, which was confirmed by  $\theta - 2\theta$  scans (Fig. 4.1a and Fig. 4.2a). Only the  $00l$  reflections of the Ba-122 phase as well as the single crystalline substrate were observed. The (103)  $\phi$ -scan (Fig. 4.1b and Fig. 4.2b) and the pole figure measurements of the (103) Ba-122 reflection of the film revealed an in-plane orientation with FWHM values,  $\Delta\phi$ , of  $0.56^\circ$  and  $0.96^\circ$  for films A and B, respectively. Rocking curve measurements on the (004) reflection showed a sharp  $\Delta\omega_{\text{Ba-122,(004)}}$  of  $0.54^\circ$  and  $0.74^\circ$  for films A and B, respectively, as can be seen in Fig. 4.1d and Fig. 4.2d (values are not corrected for device broadening). The epitaxial relation was confirmed to be  $(001)[100]\text{Ba-122} \parallel (001)[100]\text{MgO}$ .

Overview brightfield TEM images (Fig. 4.3 and Fig. 4.4) were taken on an FEI Tecnai T20 (LaB<sub>6</sub>, 200 kV). High-resolution imaging was carried out using an FEI Titan 80-300, operating at 300 kV (FEG) with an image- $C_s$  corrector. The lamella was prepared with the in-situ lift-off method in a focused ion beam device [134]. In Fig. 4.3c, no reaction layer can be observed at the interface between the P-doped Ba-122 thin film and the MgO substrate. Additionally, neither appreciable defects nor grain boundaries were observed in the TEM investigations (Fig. 4.3) for sample A, again indicating a high crystalline quality and phase purity of the investigated film. For sample B (see Fig. 4.4), it was not possible to complete the TEM investigation in detail due to a broken lamella. Nevertheless, the pictures show a flat and homogeneous surface, but also some structural defects in the Ba-122 layer, as well as a possible reaction layer.

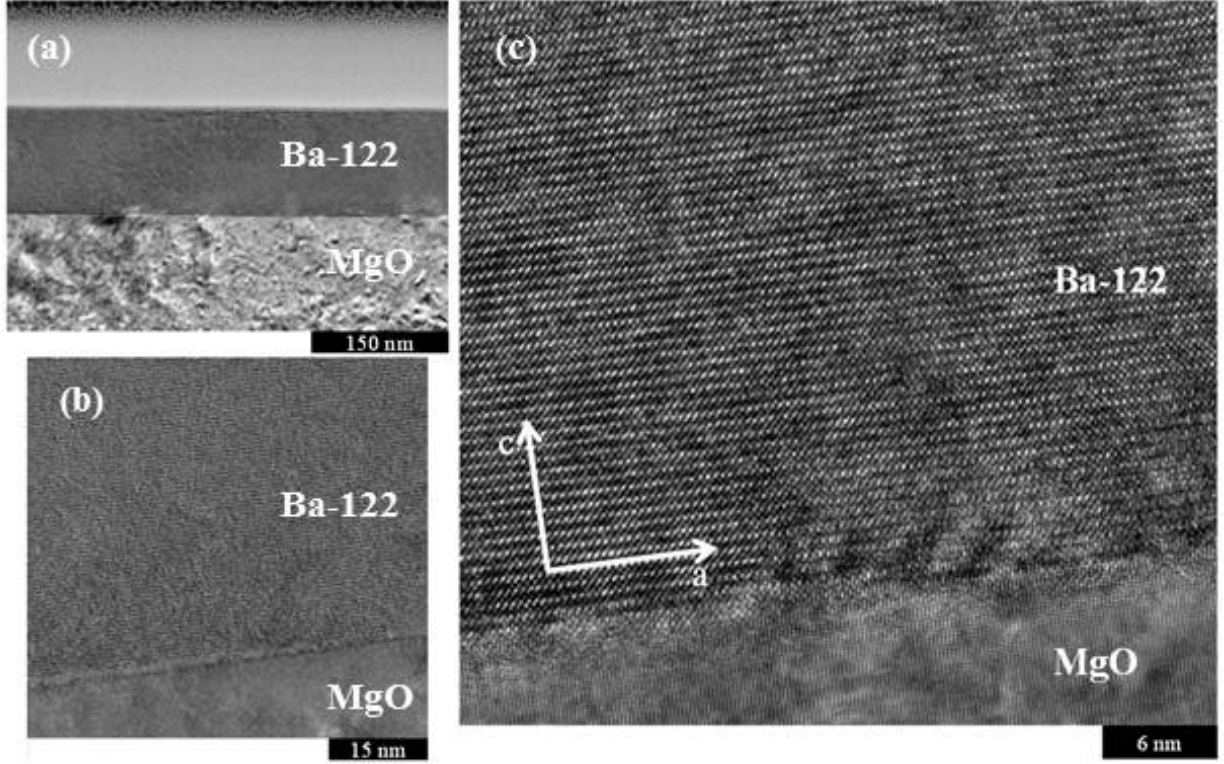


**Figure 4.1:** Structural data of the P-doped Ba-122 thin film A. (a)  $\theta - 2\theta$  scan showing the  $c$ -axis oriented growth. (b)  $\phi$ -scan of the (103) reflections of the Ba-122 and the (220) reflection of the MgO substrate proving the cube-on-cube film growth. (c) Pole figure of the (103) reflection of the Ba-122 thin film. No other growth direction was observed. The measured unit is cps. (d) Rocking curve of the (004) reflection.



**Figure 4.2:** Structural data of the P-doped Ba-122 thin film B. (a)  $\theta - 2\theta$  scan showing the  $c$ -axis oriented growth. The stars point out reflections originating from the measurement device. (b)  $\phi$ -scan of the (103) reflection of the Ba-122 and the (220) reflection of the MgO substrate proving the cube-on-cube film growth. (c) Pole figure of the (103) reflection of the Ba-122 thin film. No other growth direction was observed. The measured unit is cps. (d) Rocking curve of the (004) reflection.

The film stoichiometry was confirmed by EPMA to be Ba:Fe:(As+P) = 1 : 1.92 : 1.93 and 1 : 2.09 : 2.09, with a P content of 0.22 and 0.23 for film A and B, respectively, which is lower than the optimal doping level for single crystals or powder samples (i.e., 0.33) [44, 135, 136].

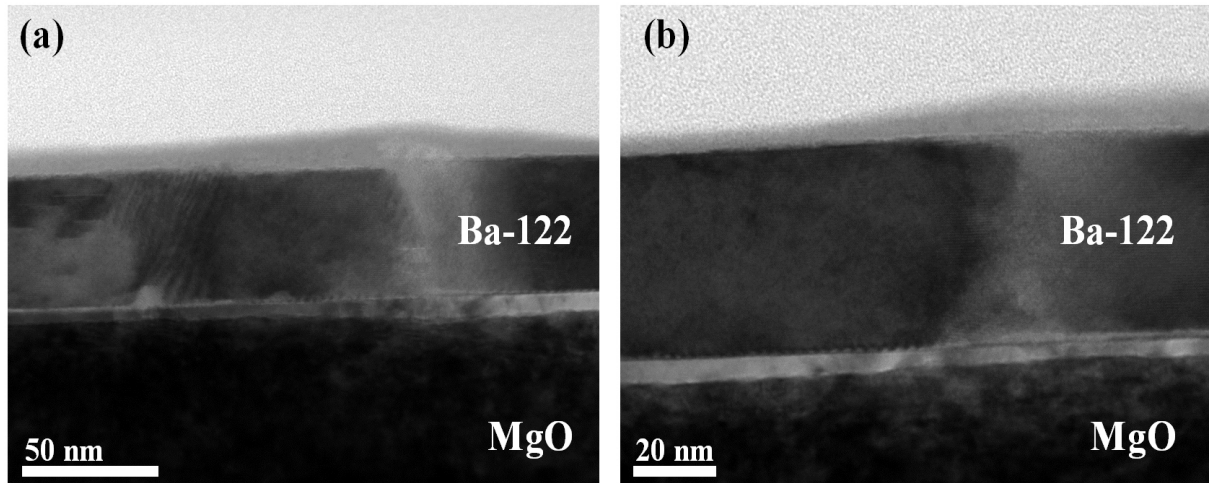


**Figure 4.3:** TEM pictures of the P-doped Ba-122 thin film A. (a) A flat and homogeneous surface has been observed. (b) and (c) No defects along the *a*- or *c*-axis have been found, pointing to a nearly perfect film growth.

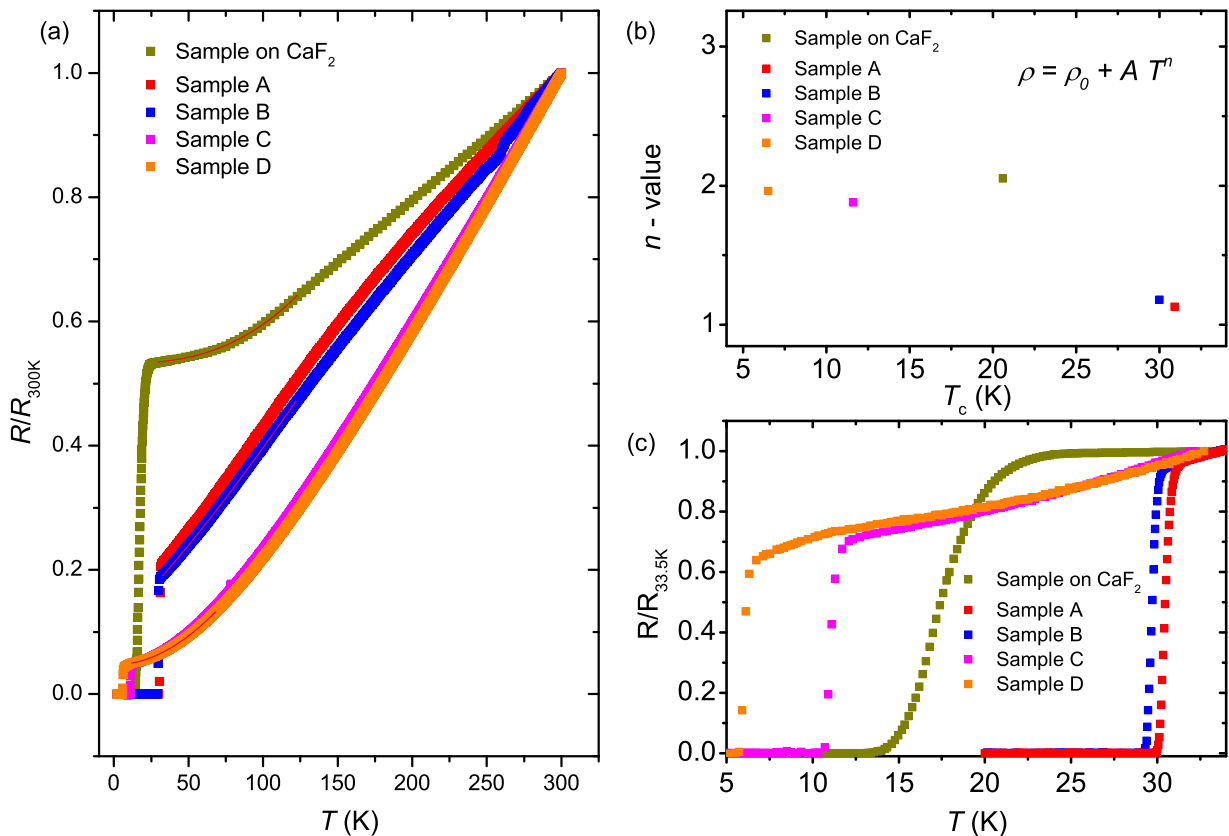
## 4.4 Superconducting properties of P-doped Ba-122

High-field transport measurements on a small bridge of 1 mm length and 40  $\mu\text{m}$  width, prepared by laser-cutting, were conducted in the dc facility up to 35 T at the NHMFL at 4.2 K. The higher temperature measurements were performed in a 16 T PPMS. A criterion of 1  $\mu\text{V}/\text{cm}$  was used to define  $J_c$ . The magnetic field  $H$  was applied in maximum Lorentz force configuration during all measurements ( $H \perp J$ ,  $J$  being the current density). Resistivity measurements in the absence of magnetic field unveiled an onset  $T_c$  of 30.7 K and 30.0 K for films A and B, respectively, which is higher than that of PLD processed films [85, 87] and comparable with the  $T_c$  of optimally doped single crystals [137]; however,

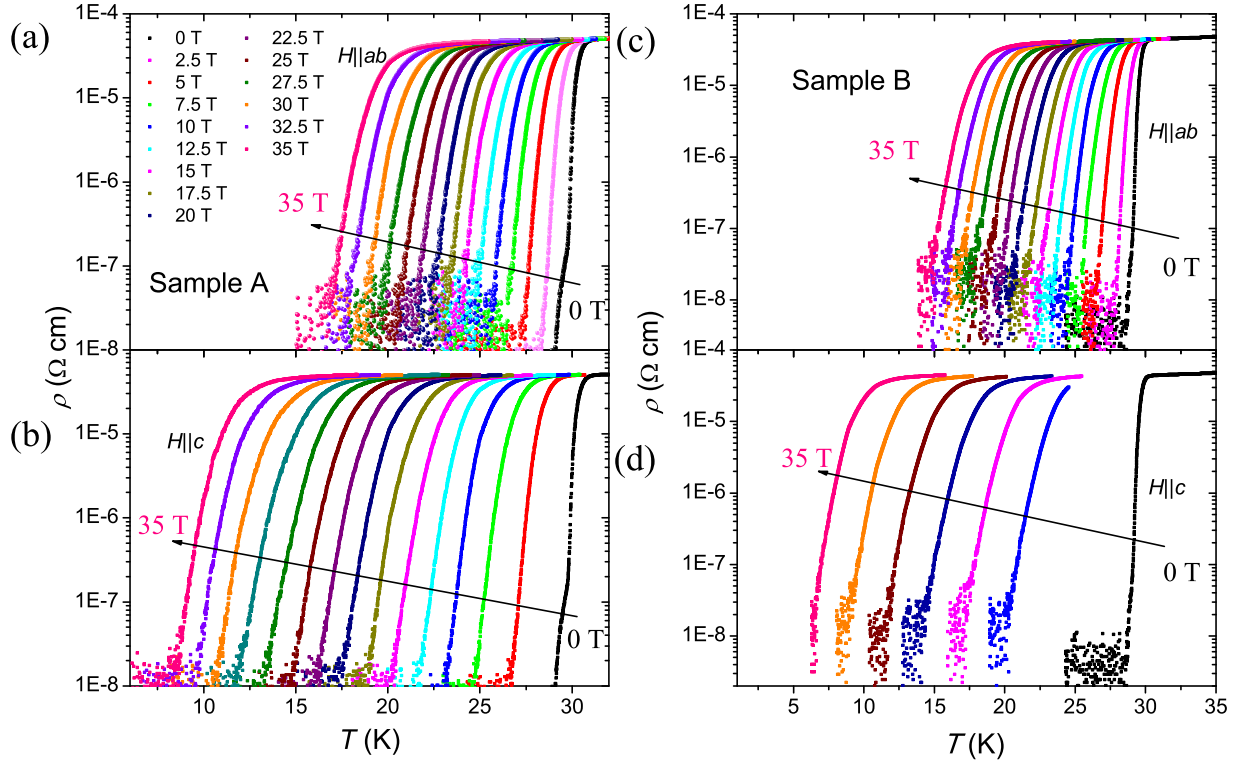




**Figure 4.4:** TEM pictures of the P-doped Ba-122 thin film B in (a) lower and (b) higher magnification. A flat and homogeneous surface has been observed, as well as some defects in the crystal structure.



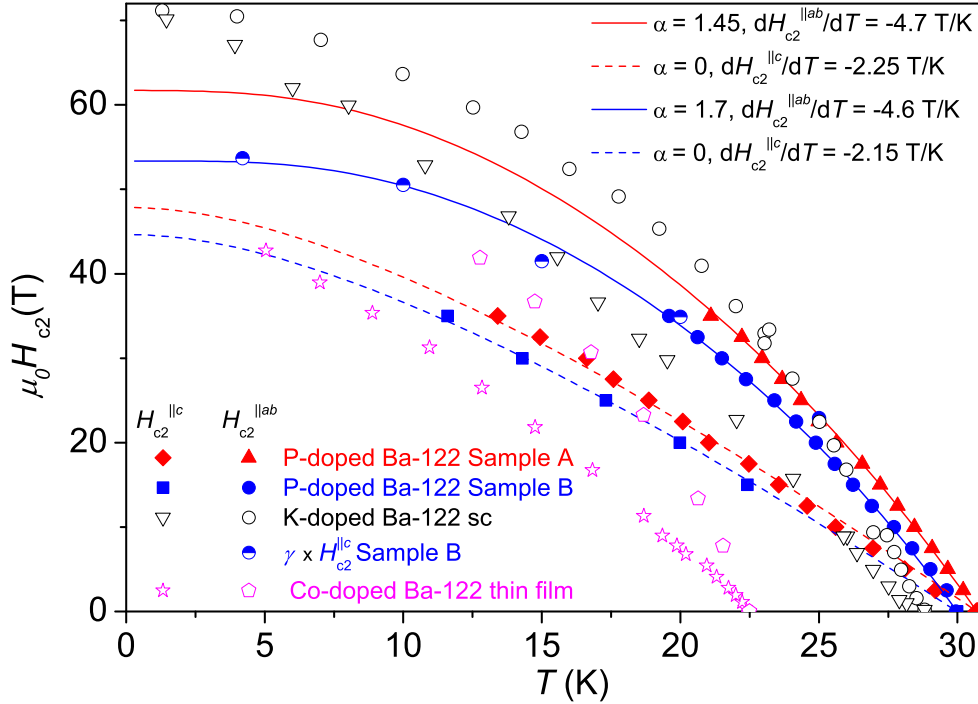
**Figure 4.5:** (a) Normalised temperature dependence of the resistance for different P-doped Ba-122 thin films measured up to 300 K. The solid red lines are the fitting curves using the equation  $\rho = \rho_0 + AT^n$  in the range of  $T_c < T < 120$  K. (b) The resultant  $n$ -values as a function of  $T_c$ . (c) Normalised resistance curves for all films in the vicinity of  $T_c$ .



**Figure 4.6:** (a) Field dependence of the resistive measurements of the P-doped Ba-122 thin films (a,b) Sample A and (c,d) Sample B in (a,c)  $H||ab$  and (b,d)  $H||c$  direction.

the films have a lower P content. The lattice parameters  $c = 12.78 \text{ \AA}$  and  $c = 12.77 \text{ \AA}$  of the respective films A and B (evaluated from XRD analysis presented in Fig. 4.1a and Fig. 4.2a, using the Nelson-Riley fit,) are shorter than that of single crystals with the same P content ( $c = 12.88 \text{ \AA}$ ) [135]. This arises from the presence of tensile strain in the films. Investigating the superconducting properties of BaFe<sub>2</sub>(As<sub>1-x</sub>P<sub>x</sub>)<sub>2</sub> thin films grown by MBE on LAO and MgO substrates, Kawaguchi *et al.* reported that tensile strain in the underdoped regime for P-doped Ba-122 enhances  $T_c$  [130]. The normal state resistivity shows a linear temperature dependence below 100 K, which is a typical behaviour for optimally P-doped Ba-122 (Fig. 4.5a) [138]. The resistive measurements of P-doped Ba-122 thin films grown onto different substrates by PLD (Sample on CaF<sub>2</sub>) and MBE (Sample C and Sample D), exhibiting different  $T_c$ , are plotted in Fig. 4.5 to emphasise the different shape of the resistance curve in the normal state. These films were grown with an intentional non-optimal doping of P. The different shape is due to the transition from the non-Fermi-liquid state to the Fermi-liquid counterpart at the funnel shaped quantum critical region of P-doped Ba-122 when the sample is cooled down, and was pointed out by Analytis *et al.* [139].  $n$  is close to unity for Sample A and Sample B with the maximum  $T_c$ , indicating the non-Fermi-liquid state. On the other hand, an exponent  $n$  of 2 for sample

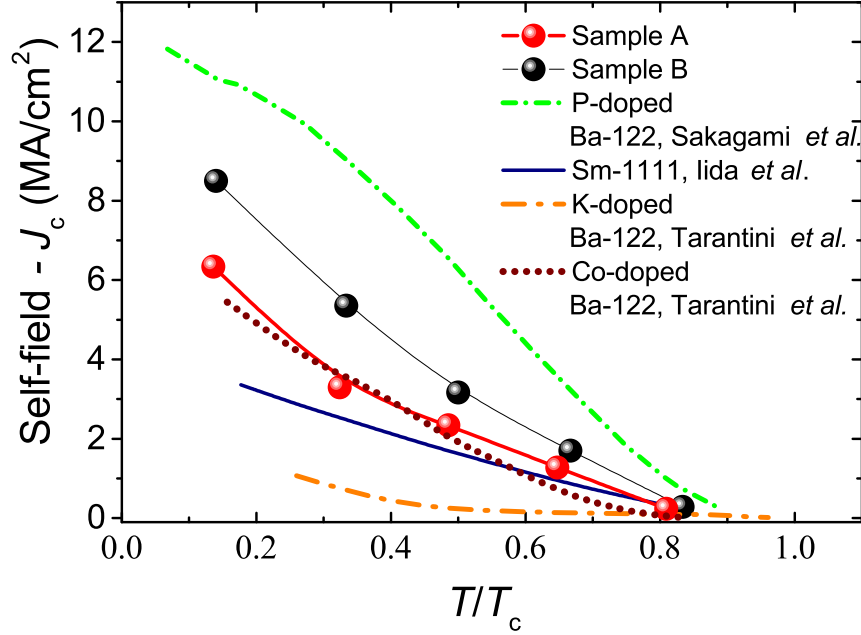
B, C, D, and the sample on  $\text{CaF}_2$  suggests a Fermi-liquid state due to electron-electron interactions. Therefore, the tensile strain shifts the superconducting transition of the films to higher values [130], comparable to a  $T_c$  of higher P concentrations without strain, a dependency which has been observed for Co-doped Ba-122 thin films as well [79].



**Figure 4.7:** Temperature dependence of the upper critical field of P-doped Ba-122 (filled symbols) in  $H\parallel c$  (rotated squares for A and blue squares for B) and  $H\parallel ab$  (triangles for A and circles for B) direction. For Sample B,  $H_{c2}^{ab}$  was calculated by  $\gamma \times H_{c2}^c$ . The data for a Co-doped Ba-122 thin film [140] (pink stars and pentagon) and a K-doped Ba-122 single crystal [141] (black triangles and circles) of comparable  $T_c$  are shown as well. The lines are the single-band WHH fits of the P-doped Ba-122. The  $T_{c,\text{onset}}$  criterion was used for extracting the  $H_{c2}$ .

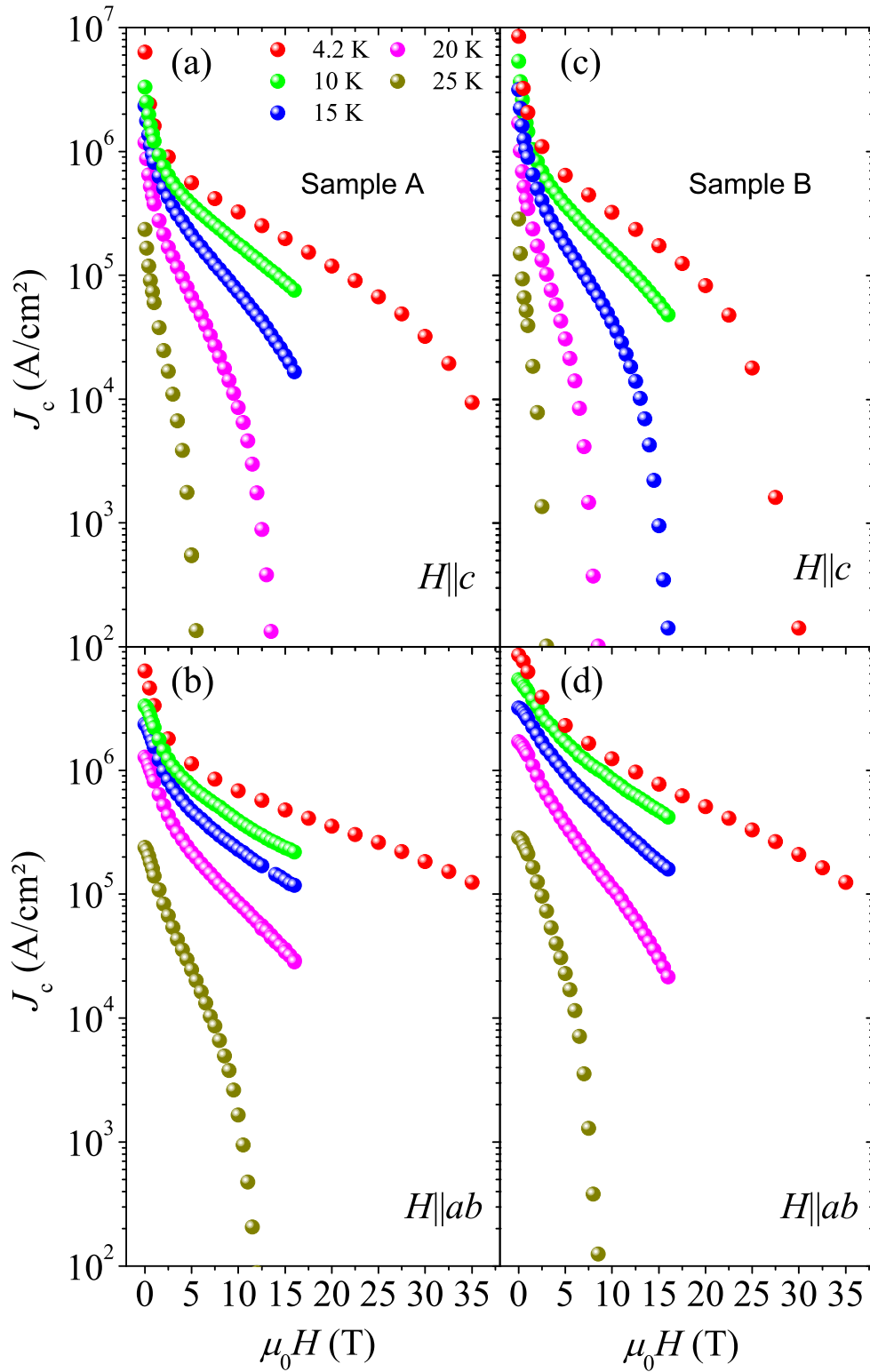
The temperature dependence of the resistivity  $\rho(T)$  was measured in magnetic fields up to 35 T, in both main crystallographic directions (Fig. 4.6). The broadening of the transition width with increasing magnetic field is small, similar to other Ba-122 systems, due to the small Ginzburg number,  $G_i$  [142]. The temperature dependence of the  $H_{c2}$  values evaluated from the resistivity data shown in Fig. 4.6 is plotted in Fig. 4.7. The  $H_{c2}$  data for both directions (i.e.  $H\parallel c$  and  $H\parallel ab$ ) can be fitted by the single-band Werthamer-Helfand-Hohenberg (WHH) model [143]. The temperature dependence of  $H_{c2}$  for  $H\parallel c$  does not show any paramagnetic limiting effects up to 35 T in accordance with data by Putzke *et al.* [137] (i.e. Maki parameter  $\alpha = 0$ ). However,  $H_{c2}$  for  $H\parallel ab$  is reduced at low temperatures, compared to an extrapolation from the slope at  $T_c$  with  $\alpha=0$ . In this case,

a value of  $\alpha = 1.45$  was obtained. This can be attributed to a Pauli-limiting behaviour, which is typical for FBS [144, 145]. As can be seen in Fig. 4.7,  $H_{c2}(T)$  for P-doped Ba-122 is relatively small compared to other compounds having comparable  $T_c$  [140] [141, 146]. Additionally, the  $H_{c2}$  anisotropy of P-doped Ba-122 is larger than that of Co-doped and K-doped Ba-122. Nevertheless, the critical currents are unusually high for P-doped Ba-122 compared to other FBS, as shown below.

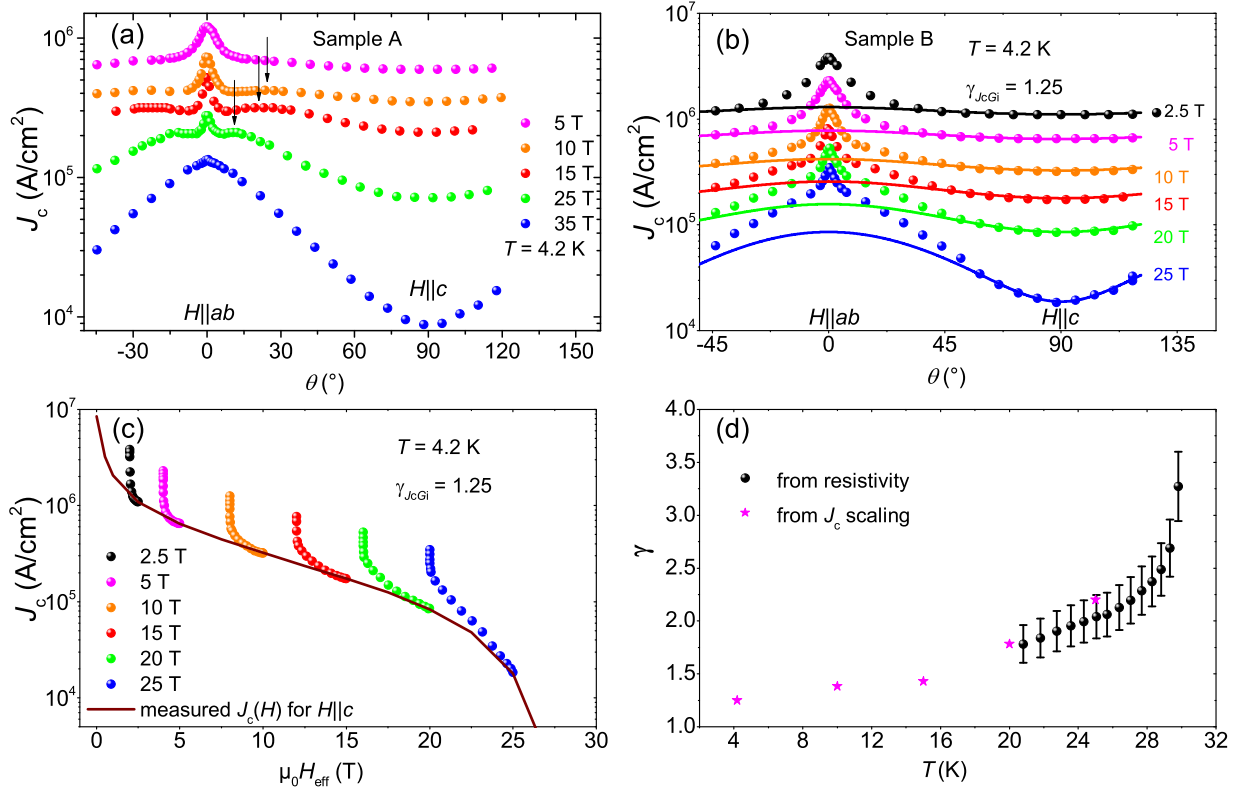


**Figure 4.8:** Self-field  $J_c$  in dependence on the normalised temperature for several FBS [147] [86, 120, 148]. The temperature is normalised to  $T_{c,onset}$ , in the case of Sm-1111 to  $T_{c,90}$ .

In Fig. 4.8, the temperature dependence of the self-field  $J_c$  for the P-doped Ba-122 thin films is compared to other  $J_c$  results reported for FBS. It is seen, that P-doped Ba-122 shows the highest self-field  $J_c$  values among FBS. Even SmFeAs(O,F) (Sm-1111) with a much higher  $T_c$  of 54K shows smaller  $J_c$  values, as was reported in Chapter 5 [147] [120, 148]. The clean P-doped Ba-122 film (sample A) presents a self-field  $J_c$  of about 6.3 MA/cm<sup>2</sup> at 4.2 K, which is almost 7% of the depairing current density [142, 149]. Sample B shows a slightly higher Fe content as well as higher self-field  $J_c$  of 8.5 MA/cm<sup>2</sup> at 4.2 K, which is even 9% of the depairing current density. This  $J_c$  may be further increased by adding artificial pinning centres [88]. As can be seen in Fig. 4.8, the film prepared by the same method but with an excess of Fe content during the growth has twice the value of  $J_c$  [86]. The different shape of the temperature dependence of the self-field  $J_c$ , when comparing our films to the film prepared by Sakagami *et al.*, can be explained by the existence of  $\delta T_c$  pinning in the thin film containing Fe particles. The shape of the



**Figure 4.9:** Field dependence of the  $J_c$  of the P-doped Ba-122 thin films (Sample A, left, and Sample B, right) in  $H||c$  (top) and  $H||ab$  (bottom) direction, measured at different temperatures.



**Figure 4.10:** (a) Angle dependence of  $J_c$  of P-doped Ba-122 thin films, for Sample A and (b) Sample B measured in various magnetic fields at 4.2 K. The curves in (b) show the respective calculated  $J_c$ . (c) Blatter scaling for Sample B at 4.2 K, resulting in a  $\gamma_{J_c G_i}$  value of 1.25. The scaling has also been done for 10 K, 15 K, 20 K and 25 K. (d) Anisotropy value  $\gamma$  calculated from  $J_c$  scaling of the data measured at different temperatures in the PPMS up to 16 T (pink stars) and resistivity data (black circles).

curve can be described by an initial upturn at high temperatures which is reduced at lower temperatures, comparable to observations that were done for MgB<sub>2</sub> [150].

The field dependence of  $J_c$  at various temperatures is summarised in Fig. 4.9. The  $J_c$  values for  $H\parallel c$  ( $J_{c,H\parallel c}$ ) are always lower than those for  $H\parallel ab$  ( $J_{c,H\parallel ab}$ ), and no feature close to  $H\parallel c$  is observed in Figs. 4.10a and b: these findings indicate the absence of  $c$ -axis correlated pinning and that the material anisotropy dominates the general  $J_c$  trend. The pinning force density ( $F_p$ , shown in Fig. 4.12) calculated according to  $F_p = H \times J_c$  at 4.2 K shows values up to 77 GN/m<sup>3</sup> (at 15 T for sample A) and 125 GN/m<sup>3</sup> (at 10 T for sample B) for  $H\parallel ab$ . The data for  $H\parallel c$  show a maximum of around 35 GN/m<sup>3</sup> at 10 T for both films (Table 4.2). Compared to the results presented by Miura *et al.* [87, 88] and Adachi *et al.* [85], the films showed slightly higher  $J_c$  values which might be due to the higher  $T_c$ . In particular  $J_c$  at 35 T  $H\parallel c$  is as high as  $J_{c,H\parallel c}=1 \times 10^4$  A/cm<sup>2</sup> for sample A. In general,  $J_c$  of the optimally P-doped Ba-122 thin films is quite robust against applied magnetic fields. The question arises why the microstructurally clean film exhibits such high  $J_c$  values. Usually, a high density of defects is necessary to achieve high  $J_c$  results. However, neither crystal structure defects nor impurity phases were observed in film A (Fig. 4.1 and Fig. 4.3). Alternatively, it has been shown by Putzke *et al.* that the vortex core energy of the flux lines is enhanced close to the optimal doping (see Fig. 4.11) [137]. Therefore, it can be supposed that this high vortex core energy is a key factor responsible for the unusually high  $J_c$  in optimally P-doped Ba-122. In this context, comparable  $J_c$  values of the P-doped Ba-122 with  $T_c$  around 25 K containing BZO particles [88] or strong pinning centres [89] could be explained by the reduction of the vortex core energy due to non-optimal  $T_c$ .

Figure 4.10a and b shows the angular dependence of  $J_c$  [ $J_c(\theta)$ ] measured at 4.2 K and various fields up to 35 T.  $J_c$  has a broad maximum positioned at  $\theta = 0^\circ$  ( $H\parallel ab$ ) and no prominent  $J_c$  peaks at  $\theta = 90^\circ$  ( $H\parallel c$ ). Low  $J_c(H)$ -anisotropy values ( $\gamma_{J_c} = J_{c,H\parallel ab}/J_{c,H\parallel c}$ ) of around 2 up to 15 T at 4.2 K are observed. As presented in Fig. 4.4, no correlated defects were observed in sample B. In this case, (i.e. only the mass anisotropy is responsible for the  $J_c$  anisotropy)  $J_c$  can be scaled with  $H_{\text{eff}}$ , ( $H_{\text{eff}} = H \times (\sin^2\theta + \cos^2\theta/\gamma_{J_c G_1}^2)^{1/2}$ ), where  $\gamma_{J_c G_1}$  is the mass anisotropy ratio [i.e. anisotropic Ginzburg Landau (AGL) scaling]. Based on the angle dependence of the  $J_c$  measured at various temperatures, the  $\gamma_{J_c G_1}$ -values are evaluated. Unlike single-band superconductors,  $\gamma_{J_c G_1}$  shows a temperature dependence: ranging from 1.25 at 4.2 K to 2.2 at 25 K (scaling see Fig. 4.10c). Figure 4.10d presents the temperature dependence of the anisotropy. It can be seen, that  $\gamma_{J_c G_1}$  follows well the  $H_{c2}$ -anisotropy.

A small shoulder near the  $ab$ -peak, marked with arrows for sample A in Fig. 4.10a is

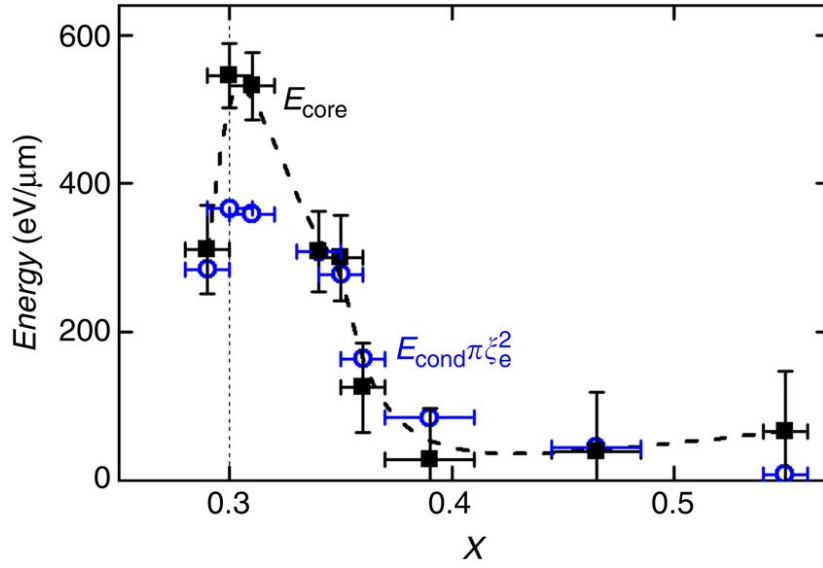
observed. It shifts to lower angles when the magnetic field is increased. Such shoulders are known from cuprates and usually exist due to strong correlated defects, such as seen in double-perovskite-doped YBCO thin films [151], or due to uncorrelated extended defects, such as in Au-irradiated YBCO thin films [152] or in SmBCO thin films with Sm-rich precipitates [153]. There, the shoulders are accompanied by extended structural defects and often also by a strong  $c$ -axis peak in a certain magnetic field range. For these films, no extended or correlated defects in TEM images nor any sign of an off-axis peak was observed by XRD. Therefore, the reason for these shoulders may lie in a possible variation of the P-content. For example, nanoscale regions of non-optimal P-content (not observable in TEM) of size slightly larger than the coherence length might act as uncorrelated strong pinning centres due to the unusually strong P-content dependence of the vortex core energy (shown in Fig. 4.11) [137, 154]. These possible P-inhomogeneities in combination with the inequality of  $\lambda$  and  $\xi$  anisotropy as in the FBS can lead to such shoulders, as was shown by van der Beek *et al.* [155]. This scenario is further evidenced by the  $J_c(T)$  dependence at intermediate and high temperatures (Fig. 4.8a). Additional artificial disorder in the form of Fe impurities enhances the strong pinning, resulting in a  $J_c(T)$  dependence consistent with the  $\delta l$  pinning scenario in the whole temperature range [156].  $\delta l$  pinning is induced by fluctuations in the mean free path of the charge carriers. Thus, it can be believed that pinning driven by differences in the vortex core energy enhances  $J_c$  values of the optimally P-doped Ba-122 well above all other FBS.

There is still room for a further increase in  $J_c$  of the P-doped Ba-122 thin films, like doping with pinning-promoting particles like it was done by Miura *et al.* [88] in combination with optimal growth [46] [89] and high crystalline quality. Additionally, a high concentration of a secondary phase like Fe can be incorporated into the superconducting matrix as artificial pinning centres for a  $J_c$  increase without a detrimental decrease in  $T_c$  [86]. This implies that the  $J_c$  anisotropy can be reduced while maintaining a high  $T_c$  as well as  $J_c$ . The unusually high critical currents make P-doped Ba-122 one of the most promising materials among FBS for the study of the superconducting pairing mechanism and high-field applications.

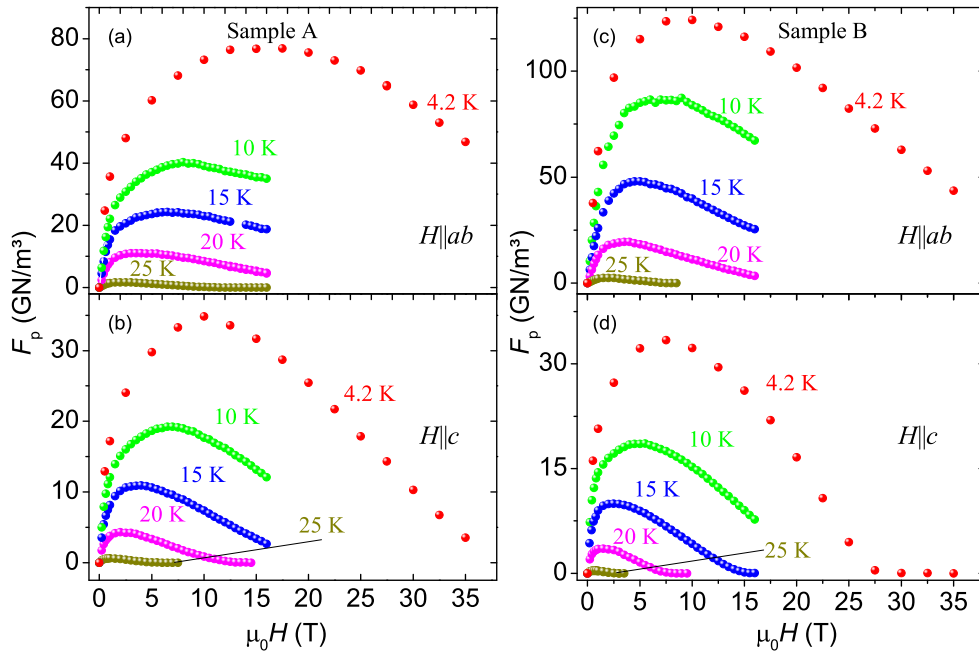
## 4.5 Summary of the chapter

To conclude, using MBE, P-doped Ba-122 thin films were successfully fabricated directly on MgO substrates, achieving epitaxy and phase purity with a high  $T_c$  of 30.7 K and 30.0 K for sample A and sample B, respectively. Although both samples A and B show a high  $T_c$  and non-Fermi-liquid behaviour, the P content is lower than observed for optimally





**Figure 4.11:** Doping dependence of the vortex core energy,  $E_{\text{core}}$  (black squares) along with an alternative estimate derived from the specific heat condensation energy ( $E_{\text{cond}}$ , blue circles) and the effective vortex area ( $\pi\xi_e^2$ ). The dashed lines are guides to the eye.  $x$  is the P content [i.e.  $x$  in  $\text{BaFe}_2(\text{P}_x\text{As}_{1-x})_2$ ]. The graph is taken from Ref. [137].



**Figure 4.12:** Pinning force density of the P-doped Ba-122 thin films (Sample A, left, and Sample B, right) for both major crystallographic directions  $H \parallel c$  (bottom) and  $H \parallel ab$  (top) measured at different temperatures.

doped single crystals. This results from tensile strain which is transferred through the MgO substrate. The field and the angle dependence of  $J_c$  up to 35 T as well as the temperature dependence of  $J_c$  in fields up to 16 T were measured. A very high self-field  $J_c$  of 6.3 MA/cm<sup>2</sup> and 8.5 MA/cm<sup>2</sup> at 4.2 K for samples A and B, respectively, was observed, even though no structural defects were found in TEM and XRD for sample A. This observation suggests that in the optimally doped P-doped Ba-122 compound, rather weak structural inhomogeneities result in strong pinning centres. This unusual pinning enhancement is explained by a sharp maximum in the vortex core energy near to the optimal doping.

From the AGL scaling analysis, the  $\gamma_{J_c G_i}$  values are evaluated. Unlike single-band superconductors,  $\gamma_{J_c G_i}$  shows a temperature dependence ranging from 1.25 at 4.2 K to 2.2 at 25 K. It was observed that  $\gamma_{J_c G_i}$  follows well the  $H_{c2}$  anisotropy, which is similar to the Co-doped Ba-122 [78, 140].

# 5 SmFeAs(O,F): a candidate for high-field magnet applications

## 5.1 Scientific problems

Among the recently discovered Fe-based superconductors [4], the highest superconducting transition temperature  $T_c$  of 55 K has been reported for SmFeAs(O,F) [36]. This new class of material shows high upper critical fields at low temperatures, together with a moderate anisotropy coefficient ranging from 4 to 7 [157], which is favourable for high-field magnet applications. Hence, several attempts on wire fabrication using SmFeAs(O,F) by powder-in-tube technique (PIT) have already been reported [158], despite the lack of information about the field and orientation dependence of the intra-grain critical current density [i.e.  $J_c(H, \Theta)$ ]. In order to exploit this material class, the knowledge of these properties should be extended.

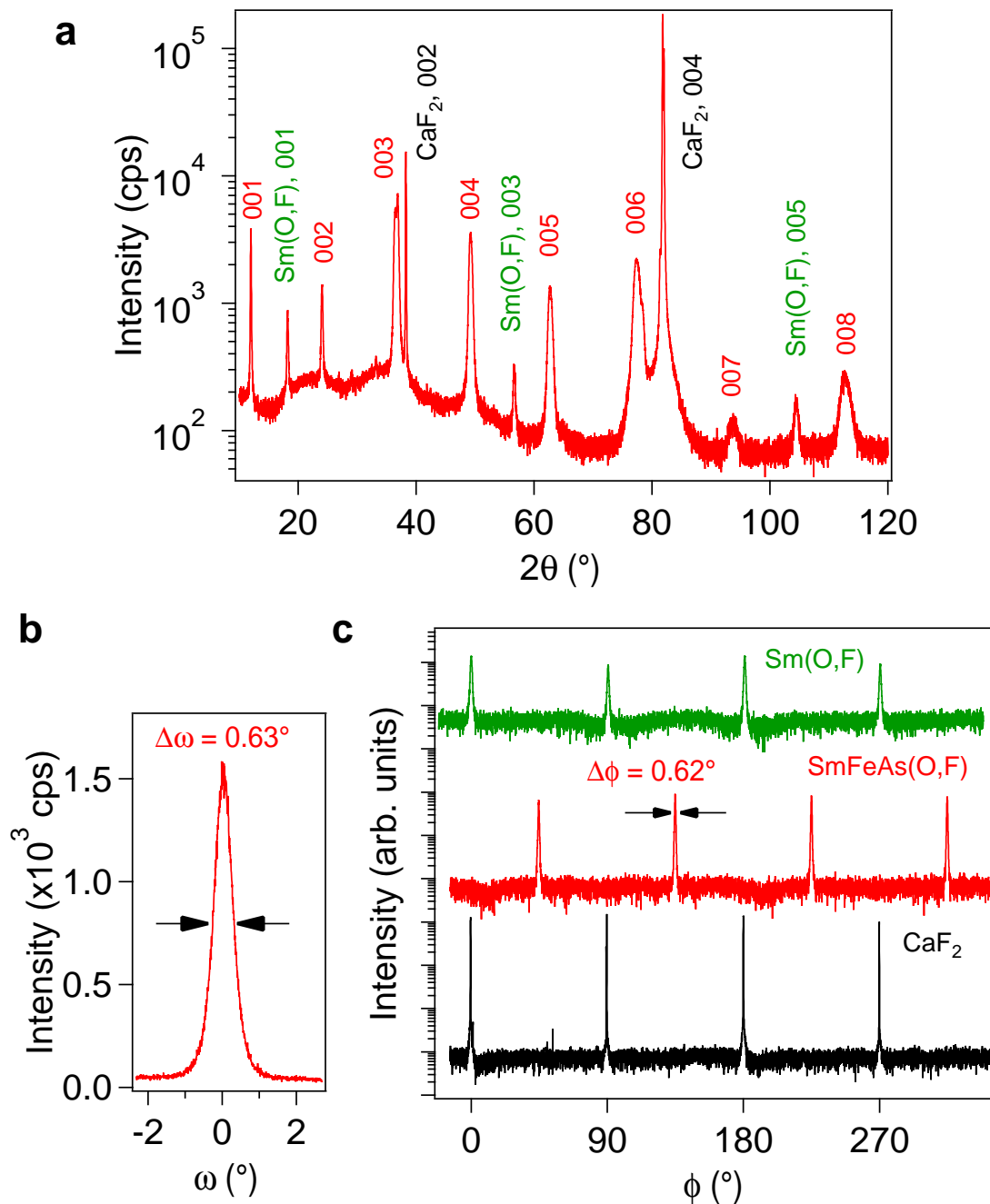
Epitaxial thin films are favourable for electronics device applications and for investigating transport, as well as optical properties, thanks to their geometry. Recent success in fabricating epitaxial Fe-based superconducting thin films opens a great opportunity for investigating their physical properties and exploring possible superconducting applications. To this date, high-field transport properties of Co-doped SrFe<sub>2</sub>As<sub>2</sub> (Sr-122), BaFe<sub>2</sub>As<sub>2</sub> (Ba-122), and Fe(Se,Te) epitaxial thin films have been reported on by several groups [70, 141] [140]. For Co-doped Ba-122, the  $J_c$  performance can be tuned by the introduction of artificial pinning centres and proton irradiation [159, 160]. Additionally, multilayer approaches that can tailor superconducting properties and their anisotropy have been reported on by Lee *et al.* [82]. Furthermore, epitaxial Co-doped Ba-122 and Fe(Se,Te) thin films have been prepared by ion-beam assisted deposition MgO-coated conductor templates [80] [161, 162] and on rolling-assisted biaxially textured substrates [163], respectively. Similarly, high-performance K-doped Ba-122 and Sr-122 wires produced by PIT have been reported on by Weiss *et al.* [126] and Gao *et al.* [164]. These results are very promising for realising Fe-based superconducting high-field applications. However, transport critical current properties of high- $T_c$  (i.e. over 50 K) oxypnictide thin films have not been reported on before,

due to the absence of high-quality films. Recently, in-situ  $LnFeAs(O,F)$  ( $Ln=Nd$  and  $Sm$ ) epitaxial thin films with  $T_c$  exceeding 50 K have been prepared by MBE [65, 113]. These successes give many possibilities to explore electro-magnetic properties.

In this chapter, various in-plane (i.e. current is flowing in the crystallographical *ab*-plane) transport properties up to 45 T of epitaxial  $SmFeAs(O,F)$  thin films grown on  $CaF_2$  (001) single crystalline substrates by MBE are presented and their pinning properties are discussed. A high  $J_c$  of over  $10^5$  A/cm<sup>2</sup> was recorded at 45 T and 4.2 K for both crystallographic directions, which is promising for high-field magnet applications. By analysing pinning properties, a dimensional crossover between the out-of-plane superconducting coherence length  $\xi_c$  and the Fe-As interlayer distance  $d_{FeAs}$  was observed at 30-40 K. This indicates a possible intrinsic Josephson junction in  $SmFeAs(O,F)$  at low temperatures [147].

## 5.2 MBE process for $SmFeAs(O,F)$

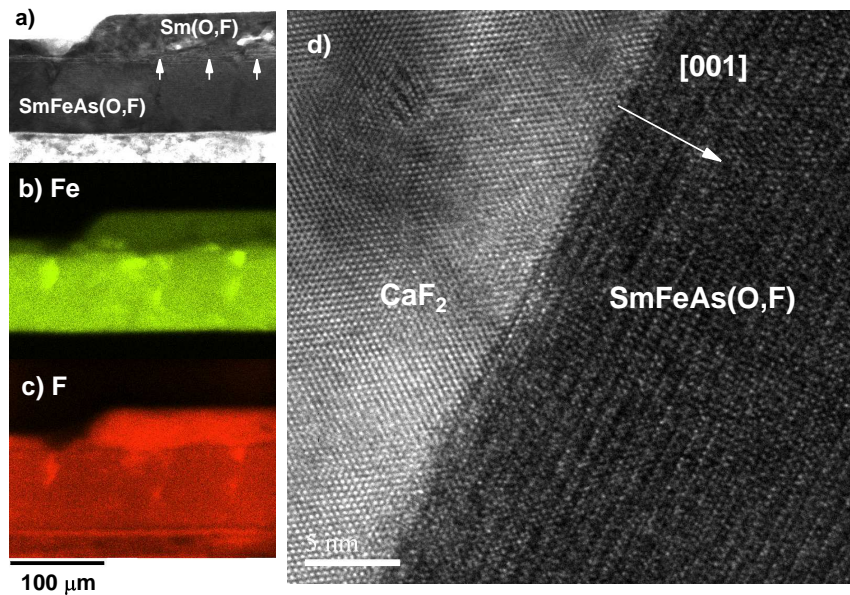
$SmFeAs(O,F)$  films of 80 nm thickness have been grown in the customer-designed MBE chamber at Tokyo University of Agriculture and Technology. A parent compound of  $SmFeAsO$  film was prepared on  $CaF_2$  (001) single crystalline substrates at 650 °C, followed by the deposition of a  $SmF_3$  cap layer. Empirically, Fe-rich pnictide films fabricated by MBE showed high  $J_c$  values [86]. Hence, a slight Fe excess was supplied during the growth of  $SmFeAsO$  layers. After the  $SmF_3$  deposition, the sample was kept at the same temperature in the MBE chamber for 30 min for the purpose of F diffusion into the  $SmFeAsO$  layer. The detailed fabrication process has been described by Ueda *et al.* [68, 113].  $SmFeAs(O,F)$  films have been grown epitaxially with high crystalline quality confirmed by XRD.



**Figure 5.1:** (a)  $\theta - 2\theta$  scan of the  $\text{SmFeAs}(\text{O},\text{F})$  thin film grown on  $\text{CaF}_2$  (001) substrate. All peaks are assigned as the  $00l$  reflections of  $\text{SmFeAs}(\text{O},\text{F})$ ,  $\text{Sm}(\text{O},\text{F})$  and  $\text{CaF}_2$ , indicative of the  $c$ -axis texturing for both  $\text{SmFeAs}(\text{O},\text{F})$  and  $\text{Sm}(\text{O},\text{F})$  layers. (b) The rocking curve of the 004 reflection of  $\text{SmFeAs}(\text{O},\text{F})$  shows a narrow FWHM of  $0.63^\circ$ , proving a highly out-of-plane textured film. (c)  $\phi$  scans of the 112 peak of  $\text{SmFeAs}(\text{O},\text{F})$ , the 112 peak of  $\text{Sm}(\text{O},\text{F})$ , and the 111 peak of  $\text{CaF}_2$ . The  $\phi$  scan of  $\text{SmFeAs}(\text{O},\text{F})$  revealed no additional reflections other than sharp (average FWHM,  $\Delta\phi$ , of  $0.63^\circ$ ) and strong reflections at every  $90^\circ$ , indicative of biaxial texture. These results highlight that the  $\text{SmFeAs}(\text{O},\text{F})$  is grown epitaxially with high crystalline quality. The  $\text{Sm}(\text{O},\text{F})$  cap layer is also grown biaxially textured. The epitaxial relation of each layer and substrate is confirmed to  $(001)[100]\text{Sm}(\text{O},\text{F})\parallel(001)[110]\text{SmFeAs}(\text{O},\text{F})\parallel(001)[100]\text{CaF}_2$ .

### 5.3 Structural properties and microstructure of SmFeAs(O,F)

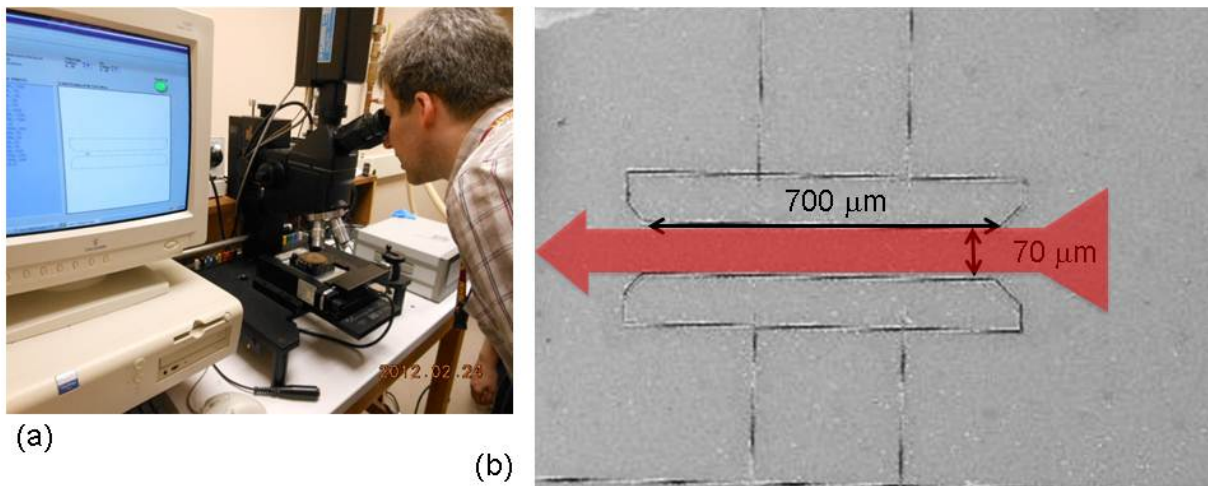
A TEM lamella of the SmFeAs(O,F) thin film was prepared by means of focused ion-beam cutting. Microstructural analyses have been performed by using a JEOL TEM-2100F TEM equipped with an energy-dispersive X-ray spectrometer. As verified by XRD, a biaxially textured SmFeAs(O,F) film with a narrow FWHM of less than  $0.65^\circ$  was obtained (Fig. 5.1). Trapezoid-shaped Sm(O,F) cap layers, which are changed from SmF<sub>3</sub>, are aligned discontinuously (Fig. 5.2a). Additionally, a crystallographically disordered layer of around 20 nm thickness, as indicated by the arrows, is present between the Sm(O,F) cap and the SmFeAs(O,F) layer. Relatively dark particles are observed in the SmFeAs(O,F) matrix, which are identified as iron-fluoride, presumably FeF<sub>2</sub>, by elemental mappings, shown in Figs. 5.2b and 5.2c. This is due to the excess of Fe supplied during the film growth. Compared to Fe(Se,Te) [94] and Co-doped Ba-122 films (Chapter 3) [96] grown by PLD, a sharp and clean interface is observed between the SmFeAs(O,F) film and the CaF<sub>2</sub> substrate, as shown in Fig. 5.2d. Furthermore, the SmFeAs(O,F) layers were free of correlated defects and large angle grain boundaries (GBs).



**Figure 5.2:** (a) Cross-sectional scanning TEM image of the SmFeAs(O,F) thin film. A crystallographically disordered layer as indicated by the arrows is present between Sm(O,F) cap and SmFeAs(O,F) layers. (b) Elemental Fe and (c) F mappings measured by energy dispersive X-ray spectroscopy. (d) High-resolution TEM image of the SmFeAs(O,F) thin film in the vicinity of the CaF<sub>2</sub> substrate/ SmFeAs(O,F) film interface.

## 5.4 Superconducting properties of $\text{SmFeAs}(\text{O},\text{F})$

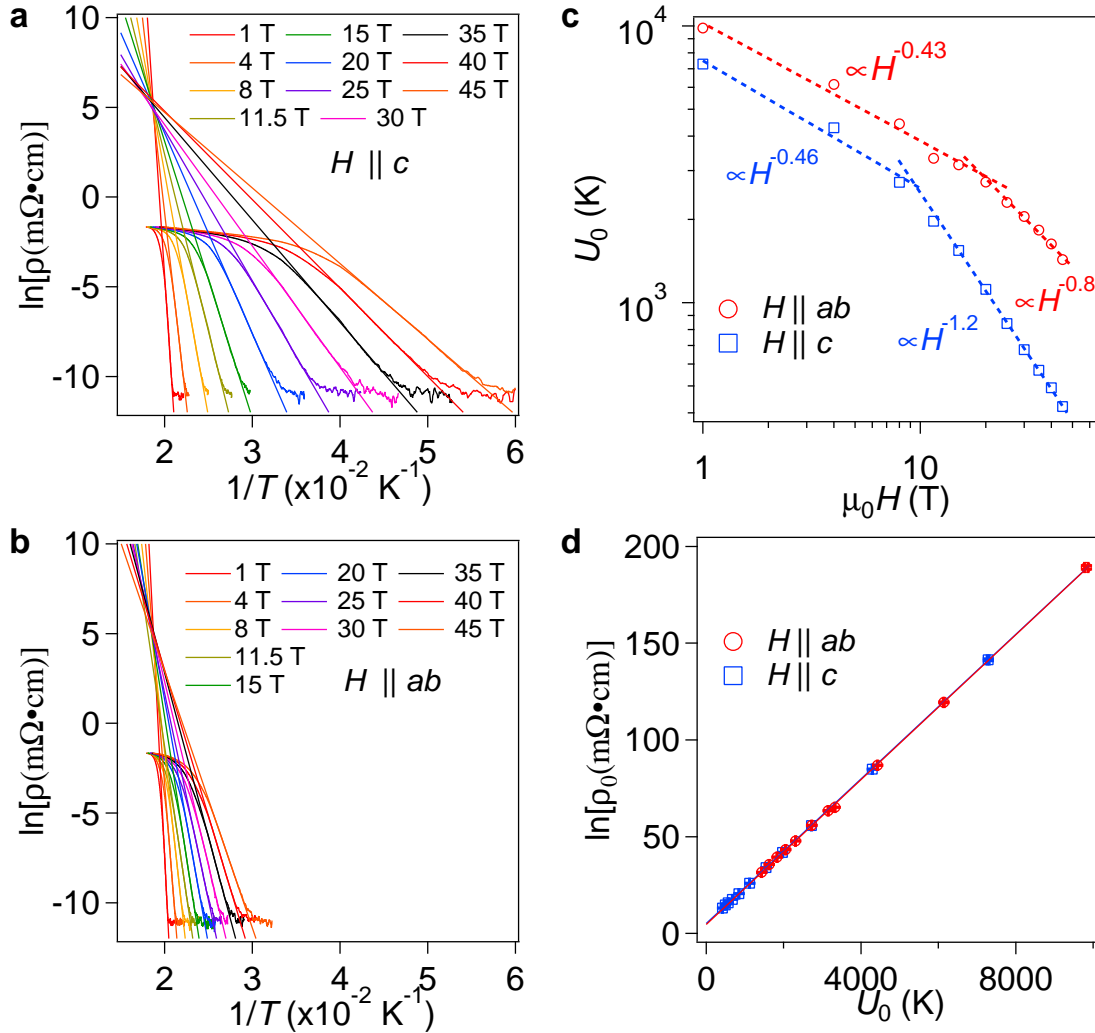
A small bridge of  $70\ \mu\text{m}$  width and  $0.7\ \text{mm}$  length was fabricated by laser cutting (see Fig. 5.3). The bridge was cut with a pulse repetition rate of  $1\ \text{kHz}$  and the energy was set to  $19\%$  of the maximum value. The laser is a  $50\ \mu\text{J}$  Q-switched Nd:YAG laser with a motorised and computer controlled microscope stage.  $I$ - $V$  characteristics on this sample were measured in four-probe configuration by a commercial PPMS [Quantum Design] up to  $12\ \text{T}$ . Transport measurements up to  $45\ \text{T}$  were carried out in the high-field dc facility at the NHMFL. A voltage criterion of  $1\ \mu\text{V}/\text{cm}$  was employed for evaluating  $J_c$ . The magnetic field  $H$  was applied in maximum Lorentz force configuration during all measurements ( $H \perp J$ , where  $J$  is the current density).



**Figure 5.3:** (a) The laser cutting machine in the ASC, Tallahassee, USA, for preparing the bridge for the following transport measurements. (b) View onto the Sm-1111 thin film bridge after laser cutting. The arrow points along the current path.

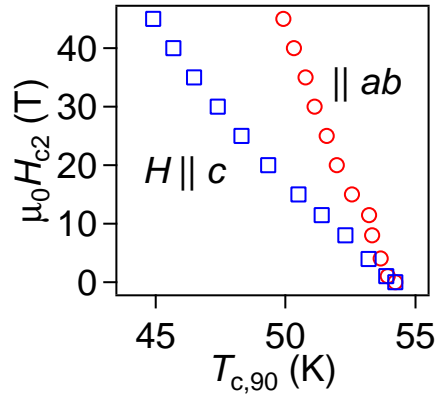
The superconducting transition temperature  $T_{c,90}$  defined as  $90\%$  of the normal state resistivity is  $54.2\ \text{K}$  in zero magnetic field. Figures 5.4a and 5.4b show Arrhenius plots of the resistivity for both main crystallographic directions measured in static fields up to  $45\ \text{T}$ . For both directions,  $T_{c,90}$  is shifted to lower temperature with increasing  $H$ , as shown in Fig. 5.5. The respective  $T_{c,90}$  at  $45\ \text{T}$  for  $H \parallel c$  and  $\parallel ab$  are  $44.9\ \text{K}$  and  $49.9\ \text{K}$ . A significant broadening of the transition is observed for  $H \parallel c$ , which is reminiscent of high- $T_c$  cuprates. Such broadening of the transition originates from enhanced thermally activated vortex motion for  $H \parallel c$ . In contrast, the in-field  $T_{c,90}$  as well as its transition width for  $H \parallel ab$  are less affected by  $H$  than that for  $H \parallel c$ . The activation energy  $U_0(H)$  for vortex motion can be estimated by the model of thermally activated flux flow [165]. On

the assumption that  $U(T, H) = U_0(H)(1 - T/T_c)$ ,  $\ln\rho(T, H) = \ln\rho_0(H) - U_0(H)/T$  and  $\ln\rho_0(H) = \ln\rho_{0f} + U_0(H)/T_c$  is obtained, where  $\rho_{0f}$  is the prefactor. In Figs. 5.4a and 5.4b, the slope of the linear fits corresponds to the  $U_0$  for vortex motion. Figure 5.4c shows  $U_0$  as a function of  $H$  for both main directions.  $U_0(H)$  shows a power law [i.e.  $U_0(H) \sim H^{-\alpha}$ ] for both crystallographic directions. In the range of  $1 \text{ T} < \mu_0 H < 8 \text{ T}$ ,  $\alpha = 0.46$  is observed for  $H \parallel c$ , whilst a similar field dependence of  $U_0(H)$  reaches 20 T for  $H \parallel ab$ . In higher fields,  $U_0$  for  $H \parallel ab$  shows a weak  $H$  dependence. On the other hand,  $\alpha = 1.2$  is obtained for  $H \parallel c$  in the range of  $8 \text{ T} < \mu_0 H < 45 \text{ T}$ , which is close to 1, suggesting a crossover from plastic to collective pinning at around  $\mu_0 H \sim 8 \text{ T}$  [166, 167].

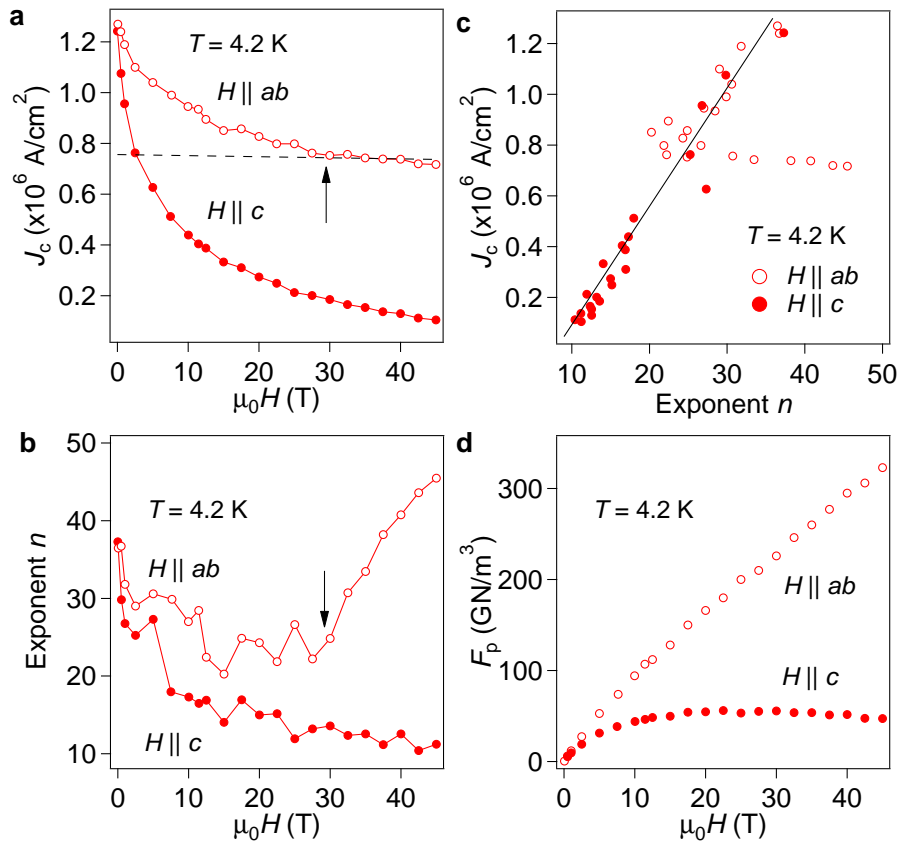


**Figure 5.4:** (a) Arrhenius plots of  $\rho$  at various magnetic fields parallel to the crystallographic  $c$ -axis and (b)  $ab$ -plane. (c) Field dependence of the activation energy for  $H \parallel c$  and  $\parallel ab$ . (d) Relationship between  $\ln\rho_0$  and  $U_0$  for  $H \parallel c$  and  $\parallel ab$ .





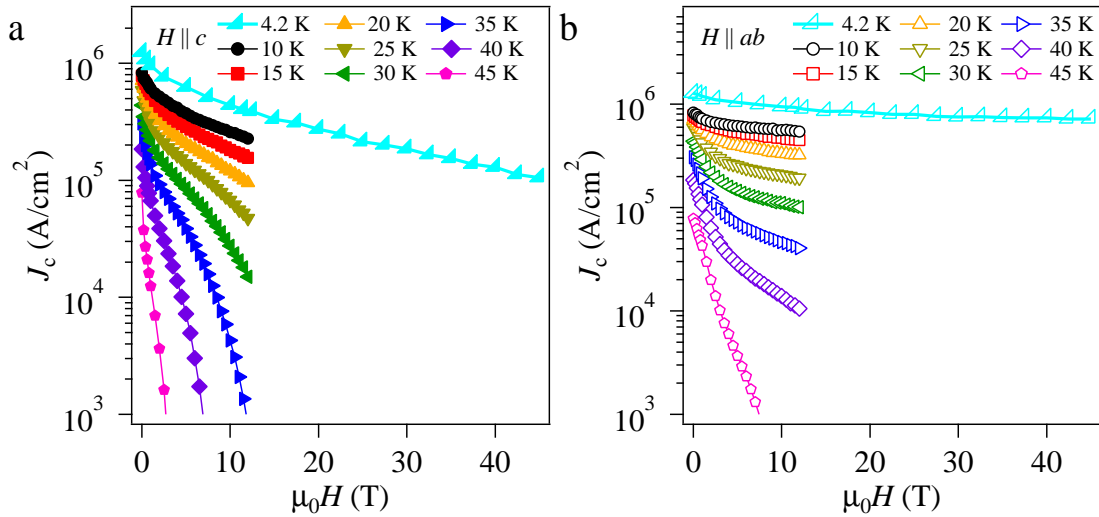
**Figure 5.5:** The temperature dependence of the  $H_{c2}$  of the  $\text{SmFeAs}(\text{O},\text{F})$  film for both directions, extracted by employing a 90% criterion of normal state resistivity.



**Figure 5.6:** (a) Field dependence of  $J_c$  measured at 4.2 K up to 45 T for both crystallographic directions and (b) the corresponding exponent  $n$  values. A crossover from extrinsic to intrinsic pinning is indicated by the arrow. (c) Scaling behaviour of the field dependent  $J_c$ . (d) Pinning force density  $F_p$  for both crystallographic directions at 4.2 K.

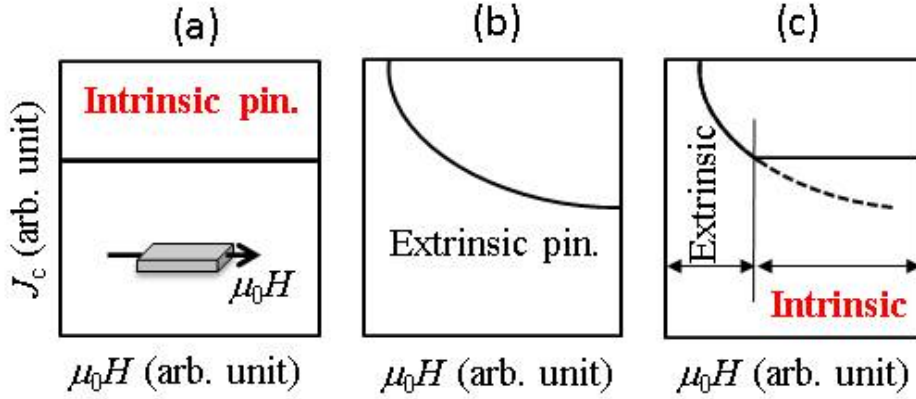
Figure 5.4d shows the relationship between  $\ln\rho_0$  and  $U_0$  for  $H \parallel c$  and  $\parallel ab$ . The linear fitting for  $H \parallel c$  yields  $T_c = 53.4 \pm 0.2$  K, while the corresponding value for  $H \parallel ab$  is  $T_c = 53.5 \pm 0.2$  K. Both  $T_c$  values are equal within error and close to  $T_{c,90}$ . This perfect linear scaling is due to the correct assumption that both conditions  $U(T, H) = U_0(H)(1 - T/T_c)$  and  $\rho_{of} = \text{const.}$  are satisfied in a wide temperature range (see Figs. 5.4a and 5.4b).

The field dependence of  $J_c$  at 4.2 K for both principal crystallographic directions measured up to 45 T is displayed in Fig. 5.6a.  $J_c$  for  $H \parallel c$  ( $J_c^c$ ) is lower than that for  $H \parallel ab$  ( $J_c^{ab}$ ), which is a consequence of the moderate anisotropy of SmFeAs(O,F). This tendency is observed for all temperature regions (see Fig. 5.7). A  $J_c^c$  of over  $10^5$  A/cm<sup>2</sup> was recorded even at 45 T, which is favourable for high-field magnet applications.



**Figure 5.7:** Magnetic field dependence of  $J_c$  measured at different temperatures for (a)  $H \parallel c$  ( $J_c^c$ ) and (b)  $H \parallel ab$  ( $J_c^{ab}$ ). For  $\mu_0 H > 3$  T,  $J_c^{ab}$  is getting more and more insensitive to  $H$  with decreasing temperature.

$J_c^{ab}$  is observed to decrease gradually with  $H$  and shows an almost constant value of  $7.4 \times 10^5$  A/cm<sup>2</sup> for  $\mu_0 H > 28$  T. This behaviour can be explained by a combination of extrinsic (i.e., normal precipitates and stacking faults) and intrinsic pinning, which is a similar observation in the quasi two-dimensional (2D) system YBa<sub>2</sub>Cu<sub>3</sub>O<sub>7- $\delta$</sub>  [i.e.,  $\xi_c(0)/d_{\text{CuO}_2} \sim 0.4$ , where  $\xi_c(0)$  is the out-of-plane superconducting coherence length at zero temperature and  $d_{\text{CuO}_2}$  is the interlayer distance between the CuO<sub>2</sub> planes] [23]. In Figure 5.8, the principle effect of the intrinsic and extrinsic pinning mechanism onto  $J_c$  is schematically shown to explain the resulting shape of the  $J_c(H)$  of the measured film.



**Figure 5.8:** (a) The schematic view of the effect of intrinsic pinning (b) extrinsic pinning and (c) the combination of both, which leads to a temperature dependent crossover in the film on the field dependence of  $J_c$  [23].

$\text{SmFeAs}(\text{O},\text{F})$  is an alternating structure of  $\text{SmO}$  and  $\text{FeAs}$  layers, similarly to high- $T_c$  cuprates. Additionally,  $\xi_c(0)$  is shorter than the interlayer distance between  $\text{Fe-As}$  planes  $d_{\text{FeAs}}$ . Hence, a modulation of the superconducting order parameter along the crystallographic  $c$ -axis and intrinsic pinning is highly expected in  $\text{SmFeAs}(\text{O},\text{F})$ . In fact, the extrinsic pinning is dominant up to 28 T, whereas the intrinsic pinning overcomes the extrinsic one above 28 T. The estimation of  $\xi_c(0)$  and  $d_{\text{FeAs}}$  in the  $\text{SmFeAs}(\text{O},\text{F})$  case will be discussed later.

By analysing the  $E$ - $J$  curves from which  $J_c$  was determined, the information on the pinning potential is obtained. On the assumption of a logarithmic current dependence of the pinning potential  $U_p$  for homogeneous samples,  $E$ - $J$  curves show a power-law relation  $E \sim J^n$  ( $n \sim U_p/k_B T$ , where  $k_B$  is the Boltzmann constant) [36]. Hence,  $J_c$  scales with  $n$  and indeed the field dependence of  $n$  has a behaviour similar to  $J_c(H)$  for  $H \parallel c$ , as presented in Fig. 5.6b. For  $H \parallel ab$ ,  $n$  decreases with  $H$  up to 28 T, similarly to the  $J_c(H)$  behaviour, whereas at a larger field, it suddenly increases due to the dominating intrinsic pinning. Hence, a failure to scale  $J_c$  with  $n$  or deviations, as shown in Fig. 5.6c, indicates the presence of intrinsic pinning.

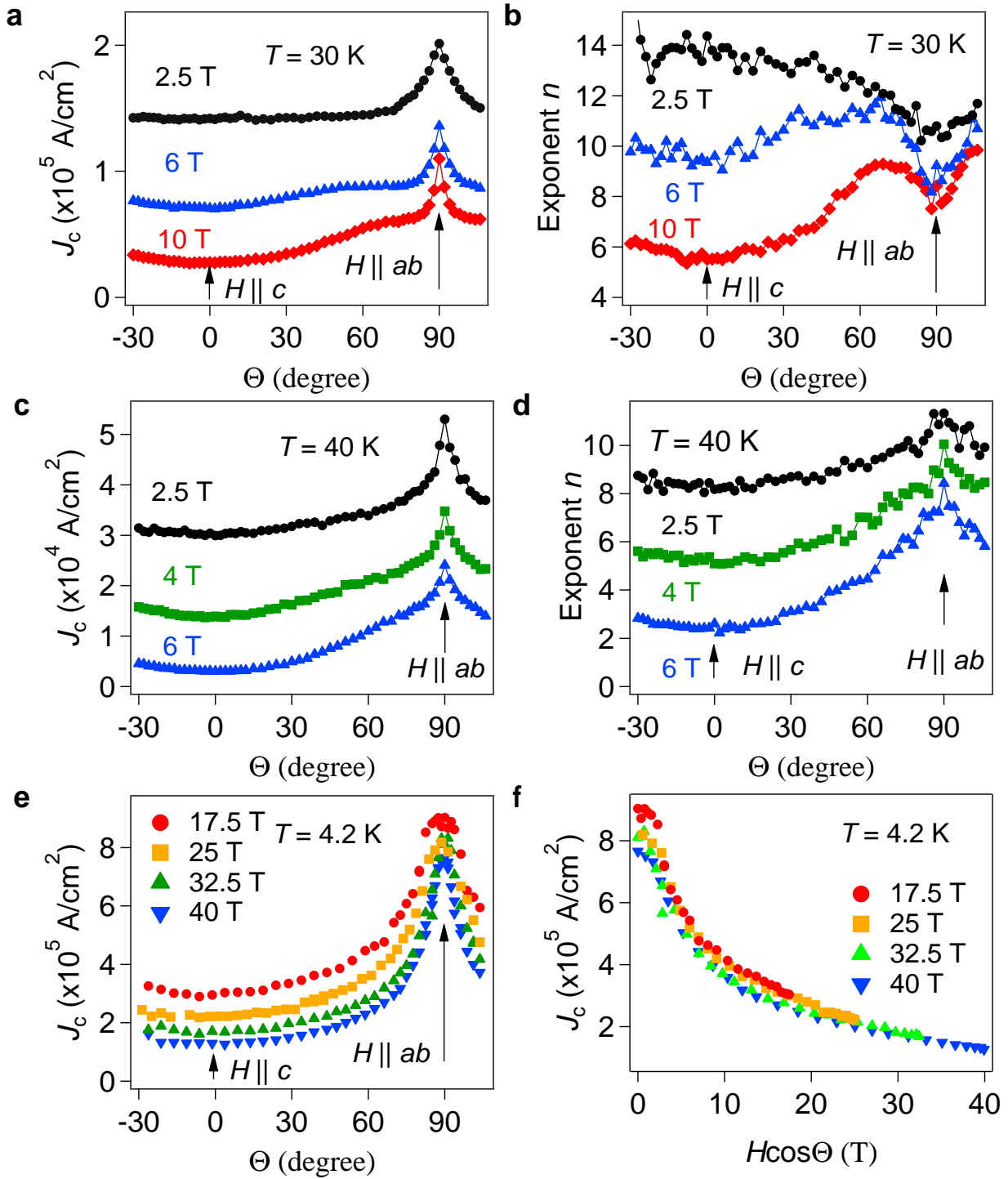
The field dependence of the pinning force density  $F_p$  for both crystallographic directions at 4.2 K is summarised in Fig. 5.6d. An almost field independent  $F_p$  above 10 T for  $H \parallel c$  is observed, whereas  $F_p$  for  $H \parallel ab$  is still increasing up to the maximum field available.

In order to gain a deeper insight into the flux pinning, the angular dependence of  $J_c$  [ $J_c(\Theta)$ , where  $\Theta$  is the angle between  $H$  and the  $c$ -axis] was measured and is summarised in Fig. 5.9. Figure 5.9a presents  $J_c(\Theta)$  at 30 K in three different magnetic fields. Almost isotropic  $J_c(\Theta, 2.5 \text{ T})$  of around  $0.14 \text{ MA/cm}^2$  was observed at angles  $\Theta$  up to  $75^\circ$ . A similar

isotropic behaviour is seen at 6 T. These results suggest the presence of  $c$ -axis correlated defects. However, the presence of these defects is ruled out by TEM investigation, since only relatively large  $\text{FeF}_2$  particles are observed in the  $\text{SmFeAs}(\text{O},\text{F})$  matrix. Recently, van der Beek *et al.* pointed out that defects of size larger than the out-of-plane coherence length contribute to  $c$ -axis pinning in anisotropic superconductors [155]. Additionally, the intrinsic pinning is active below  $T = 30 \sim 40$  K, as shown below. Hence, the combination of large particles and the intrinsic pinning may be responsible for this isotropic  $J_c(\Theta)$ .

For  $H \parallel ab$ , a broad maximum of  $J_c$  is observed and this peak becomes sharper with increasing  $H$  (Fig. 5.9a). However, the corresponding  $n$  shows a broad minimum for  $H$  close to the  $ab$  direction (Fig. 5.9b), which is an opposite behaviour compared to  $J_c$ . This is due to the thermal fluctuation of Josephson vortices, which leads to flux creep. The flux creep rate  $S = -d\ln(J)/d\ln(t)$  and the exponent  $n$  are related as  $S = 1/(n - 1)$  [168]. When the applied field is close to the  $ab$ -plane, a number of thermally fluctuating Josephson vortices are generated, leading to an increase of  $S$ . This could quantitatively explain a dip of  $n$  around  $H \parallel ab$ . A similar behaviour has been observed in  $\text{YBa}_2\text{Cu}_3\text{O}_{7-\delta}$  thin films [169–171] and  $\text{Fe}(\text{Se},\text{Te})$  thin films [172]. On the other hand, this dip of  $n$  disappears at 40 K, although the  $J_c$  still shows a broad maximum (Figs. 5.9c and 5.9d). Hence, the activation temperature of the intrinsic pinning is between 30 and 40 K, which is in good agreement with the transition temperature between Abrikosov- and Josephson-like vortices in  $\text{SmFeAs}(\text{O},\text{F})$  single crystals [173].

Figure 5.9e shows  $J_c(\Theta)$  measured at 4.2 K in fields up to 40 T. A sharp peak is observed for  $H \parallel ab$  with a  $J_c$  of around of  $8 \times 10^5$  A/cm<sup>2</sup>. For 2D superconductors (e.g.  $\text{Bi}_2\text{Sr}_2\text{CaCu}_2\text{O}_{8+x}$ ), the relation  $J_c(\Theta, H) = J_c^c(H \cos \Theta)$  holds for the intrinsic pinning regime, whereas  $J_c^{ab}$  is field independent [174, 175]. Thus, in this regime,  $J_c(\Theta, H)$  depends only on the field component along the  $c$ -axis. For the  $\text{SmFeAs}(\text{O},\text{F})$  thin film, the aforementioned condition is satisfied above 28 T at which the crossover field between extrinsic and intrinsic pinning is observed (see Fig. 5.6a). Hence, for  $\Theta > 59^\circ$  ( $\sin \Theta = 28/32.5 = 0.86$ ,  $\Theta = \sin^{-1}(0.86) = 59^\circ$ ), the  $ab$  component of the applied fields exceeds 28 T, entering the field-independent  $J_c^{ab}$  region. It means, that both angular- $J_c$  curves measured at 32.5 and 40 T rescale with  $H \cos \Theta$ , as shown in Fig. 5.9f.



**Figure 5.9:** Field and orientation dependence of critical current density ( $J_c$ ) of SmFeAs(O,F) thin film. (a) Angular dependence of  $J_c$  measured at 3 different applied magnetic fields at 30 K and (b) the corresponding exponent  $n$  values. (c)  $J_c(\Theta, H)$  measured at 40 K under several magnetic fields ( $\mu_0 H = 2.5, 4$  and  $6 \text{ T}$ ) and (d) the corresponding exponent  $n$  values. (e) Angular dependence of  $J_c$  at 4.2 K under various applied magnetic fields up to 40 T. (f) Scaling behaviour of the angular dependent  $J_c$  measurements. Below 17 T (i.e., by substituting  $\mu_0 H = 32.5 \text{ T}$  and  $\Theta = 59^\circ$  in  $H \cos \Theta$ ) as indicated by the arrow, both curves overlap.

The coherence length  $\xi_c(0)$  is estimated by using  $T_{\text{cr}} = (1 - \tau_{\text{cr}})T_c$ , where  $T_{\text{cr}}$  is the dimensional crossover temperature and  $\tau_{\text{cr}} = 2\xi_c(0)^2/d_{\text{FeAs}}^2$  is the dimensionless ratio characterising the crossover from quasi-2D-layered to continuous 3D-anisotropic behaviour [21]. By substituting  $T_{\text{cr}} = 30 - 40$  K and  $d_{\text{FeAs}} = 0.858$  nm from the XRD, shown in Fig. 5.1,  $\xi_c(0) = d_{\text{FeAs}}\sqrt{(1 - \frac{T_{\text{cr}}}{T_c})/2}$  is calculated to  $0.3 \sim 0.4$  nm. The ratio  $\xi_c(0)/d_{\text{FeAs}} = 0.35 \sim 0.47$  explains the intrinsic pinning related to a quasi-2D system observed in this film. The relation  $\xi_{\text{ab}}(0) \simeq \sqrt{\gamma}\xi_c(0)$  yields  $\xi_{\text{ab}}(0) = 1.7 \sim 2.2$  nm, where  $\gamma$  is the effective-mass or resistivity anisotropy, which is about 30 at  $T = 0$  K from measurements of the  $c$ -axis plasma frequency, using infrared ellipsometry [176]. The evaluated superconducting coherence lengths for both main crystallographic directions are in very good agreement with single-crystal values reported by Welp *et al.* [177].

The presence of a dimensional crossover indicates a possible intrinsic Josephson junction in SmFeAs(O,F), which can be used in superconducting electronic applications such as terahertz radiation sources and superconducting Qubits [178–180]. Indeed, the intrinsic Josephson junction was reported for a PrFeAsO<sub>0.7</sub> single crystal, where an  $s$ -shaped stack junction in  $c$ -direction was prepared by focused ion-beam [181].

For high-field magnet applications, a high  $J_c$  together with a low  $J_c$  anisotropy ( $\frac{J_c^{\text{ab}}}{J_c^c}$ ) in the presence of a magnetic field is necessary. The present results are promising, since  $J_c$  is over  $10^5$  A/cm<sup>2</sup> at 45 T for both main crystallographic directions. A further increase in  $J_c$  is possible, since the only appreciable defects in these SmFeAs(O,F) films are large FeF<sub>2</sub> particles. An improved pinning performance and, as a consequence, a larger  $J_c$  could be accomplished by incorporating artificial pinning centres similarly to Co-doped Ba-122 thin films reported by Tarantini *et al.* [159] or with the help of low-density columnar-defect incorporation by ion irradiation [182]. Albeit the  $J_c$  anisotropy is increasing with  $H$ , this value is still low compared to high- $T_c$  cuprates. For instance, the  $J_c$  anisotropy is about 3.6 at 30 T and 4.2 K in SmFeAs(O,F), whereas the corresponding value in YBa<sub>2</sub>Cu<sub>3</sub>O<sub>7- $\delta$</sub>  is over 7, albeit the latter shows higher  $J_c$  than the former [183].

PIT is a more realistic process than MBE for high-field magnet applications. High temperature heat treatment in PIT leads to a loss of F; however, this problem can be solved by employing a low temperature synthesis and an ex-situ process with a SmF<sub>3</sub>-containing binder, as explained in refs. [184, 185]. Despite a high  $T_c$  of over 45 K for both SmFeAs(O,F) wires, self-field  $J_c$  shows only a few thousand A/cm<sup>2</sup> at 4.2 K, which is presumably due to grain boundaries (GBs), poor grain connectivity and low density. Obviously, these PIT-processed wires contain a high density of large angle GBs. In the case of Co-doped Ba-122, GBs with misorientation angles above 9° seriously reduce the critical current [128]. However, PIT-processed K-doped Ba-122 and Sr-122 wires showed a

relatively high inter-grain  $J_c$  [126,164]. Clean GBs (i.e. no segregation of secondary phases around GBs), good grain connectivity and a low anisotropy may be responsible for these high-performance wires. An approach similar to the one employed in K-doped Ba-122 and Sr-122 wire fabrication may be useful for improving inter-grain  $J_c$  in SmFeAs(O,F) wires, as well. Nevertheless, bicrystal experiments on SmFeAs(O,F) will give valuable information on these issues.

## 5.5 Summary of the chapter

In this chapter, intrinsic electro-magnetic properties of epitaxial SmFeAs(O,F) thin films prepared by MBE on CaF<sub>2</sub> (001) substrate by measuring field-angular dependence of transport properties up to 45 T are explored. The findings strongly support the presence of a competition behaviour between extrinsic pinning below 28 T and intrinsic pinning above 28 T. The intrinsic pinning starts being effective below  $T = 30 \sim 40$  K, at which the cross-over between the out-of-plane coherence length and the interlayer distance occurs. This knowledge of SmFeAs(O,F) electro-magnetic properties could stimulate future development of superconducting applications of this class of material.





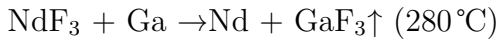
# 6 Transport properties of NdFeAs(O,F) in high magnetic fields

## 6.1 Scientific merit of NdFeAs(O,F)

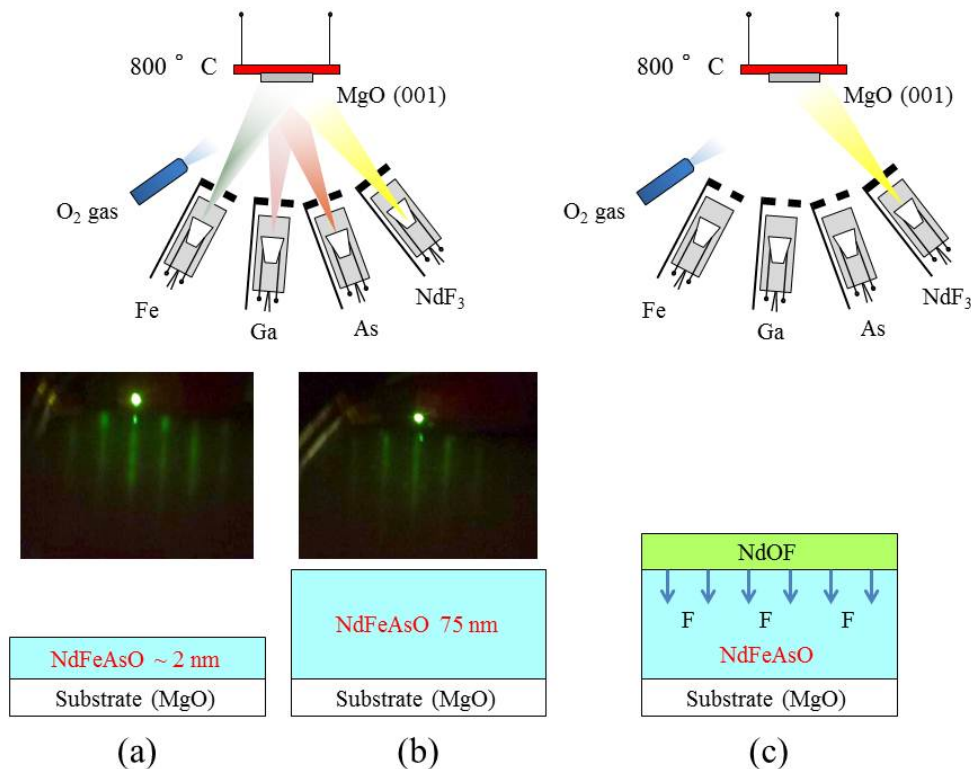
Along with SmFeAs(O,F), the NdFeAs(O,F) superconductor exhibits the highest superconducting transition temperature,  $T_c$ , apart from the cuprates. It was found in 2008 by Ren *et al.* [33, 186]. In the early stages of the discovery of the FBS, [4] investigations of the temperature-dependent in-field properties revealed promising qualities [187, 188]. NdFeAs(O,F) exhibits a large mass anisotropy, enhanced thermal fluctuations, and a Ginzburg number,  $G_i$ , comparable to that of YBCO. The question arises, if differences in the electronic properties of these materials origin from different critical temperatures or from other effects such as, for example, the presence of magnetic ions [189, 190]. In this regard, NdFeAs(O,F) and SmFeAs(O,F) are bridging materials between cuprates and MgB<sub>2</sub>. However, due to the absence of high-quality films, transport critical current properties of high- $T_c$  (i.e. over 45 K) NdFeAs(O,F) thin films have not been reported before. Recently, in-situ prepared NdFeAs(O,F) epitaxial thin films with  $T_c$  exceeding 50 K have been fabricated by MBE on various substrates [63, 65, 191, 192]. These films show a very clean microstructure, which guarantees reliable investigations. This work reports on in-field properties of epitaxial NdFeAs(O,F) thin films prepared by MBE.

## 6.2 MBE process of NdFeAs(O,F)

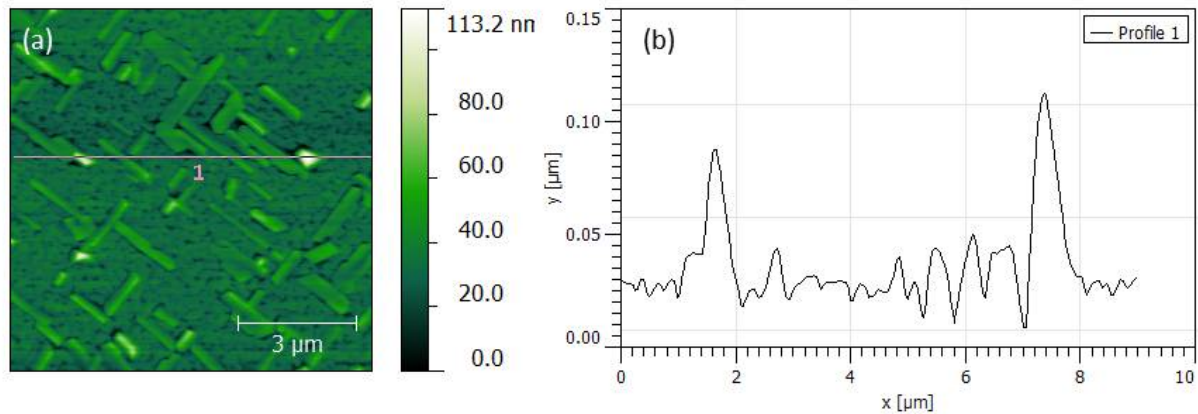
An epitaxial NdFeAs(O,F) thin film with a thickness of 90 nm has been prepared on a MgO (001) substrate by MBE using a two-step process [192]. After mounting the substrate, which was clamped to the holder using indium for effective heat transfer, it was thermally cleaned at 700 °C for 30 min (similar to the treatment reported for the growth of P-doped Ba-122, Chapter 4). The growth temperature was 800 °C and the growth rate was 100 nm/h. First, a NdFeAsO layer was prepared using the solid sources Fe, As, Ga and NdF<sub>3</sub>. Thereby, Ga works as an F getter by the following reaction:



The second step was the growth of a NdOF layer on top of the NdFeAsO. Due to the diffusion of the F into the NdFeAsO layer, superconducting NdFeAs(O,F) was obtained. After the deposition, the film was cooled to room temperature and subsequently dismantled for basic characterisations like XRD analysis. In order to remove the NdOF cap layer from the NdFeAs(O,F), ion-beam etching was carried out by the group of Prof. Paul Seidel at Friedrich-Schiller University, Jena, Germany. The sample was partially covered by photoresist varnish (AZ5114) to protect the superconducting NdFeAs(O,F) layer. As can be seen in Fig. 6.2a, NdOF islands with an average height of around 100 nm were observed. Some part of the area is covered with NdOF. Hence, over-etching is highly likely without protection. For the etching process an etching rate of 40 nm/min was applied. In order to remove the NdOF layers, we employed a longer etching time, resulting in a final thickness of around 60 nm for NdFeAs(O,F).



**Figure 6.1:** Growth of NdFeAs(O,F) thin films by MBE. (a) Applying Fe-, Ga- and As-flux with an O<sub>2</sub> gas flow produces the NdFeAsO layer. Streaks on the RHEED pattern indicate a flat surface also for (b) the end stage of the film growth. (c) Subsequently, a NdOF layer is deposited by applying a NdF<sub>3</sub> flux with O<sub>2</sub> gas flow. In this process, F diffuses into the NdFeAsO layer.

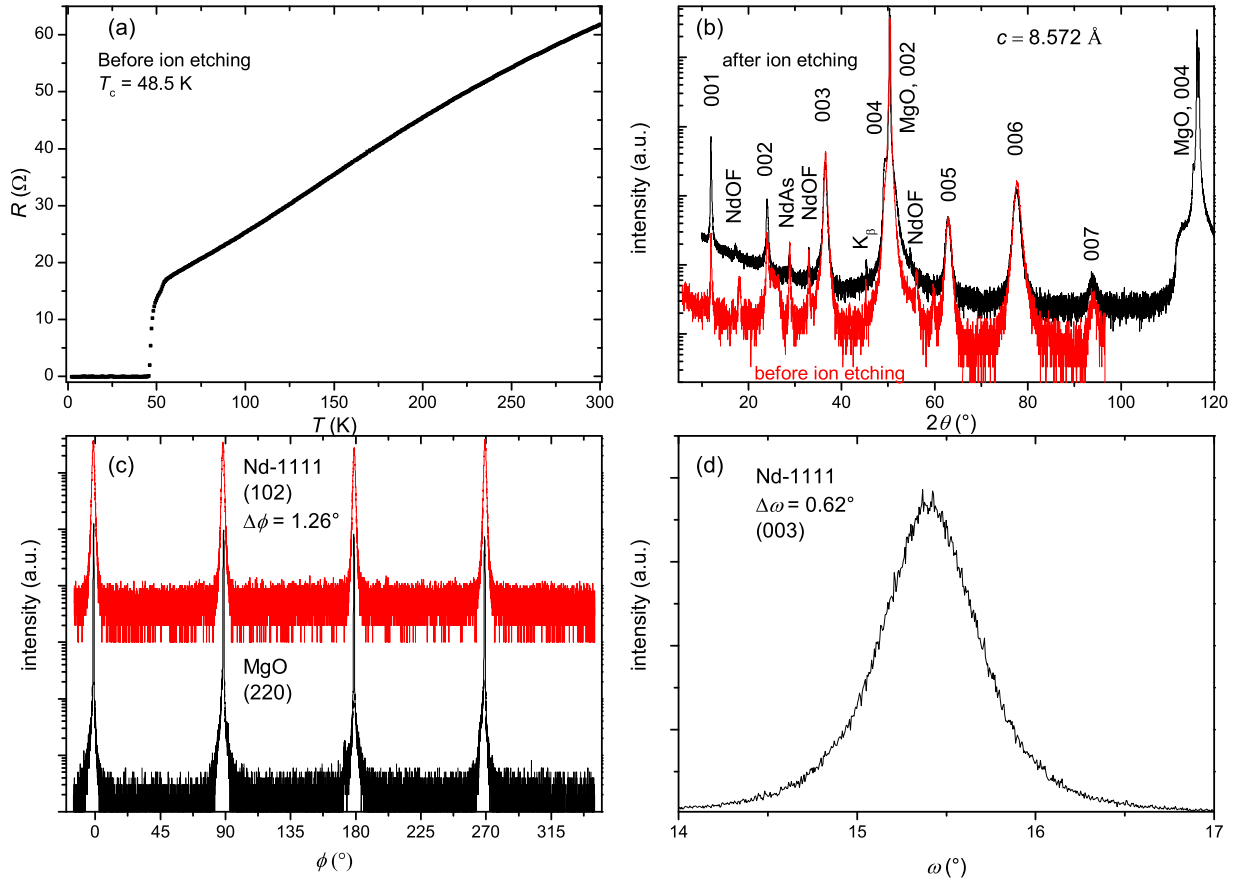


**Figure 6.2:** (a) Atomic force microscopy (AFM) picture of the film surface together with the corresponding height profile (b). The height profile was measured along the line “1” (white line in the AFM picture). The picture reveals NdOF islands with a height up to 100 nm covering the surface of the Nd-1111 layer. This picture was taken before the ion-beam etching.

### 6.3 Structural analysis of NdFeAs(O,F) by XRD

The structural investigation of the NdFeAs(O,F) thin film proved high-quality epitaxial growth of the Nd-1111 phase. Figure 6.3b shows the  $\theta$ - $2\theta$  scan for the as-grown film and for comparison, the XRD pattern for the film after ion-beam etching. Clearly, the diffraction intensity of NdOF as well as NdAs was reduced after the ion-beam etching, which indicates that the NdOF cap layer is effectively removed. The  $c$ -axis lattice constant of the film was evaluated to  $c = 8.572 \text{ \AA}$  from the Nelson-Riley function, which is very close to the value of single crystals (i.e.  $c_{sc} = 8.58 \text{ \AA}$  [12]). The (002) rocking curve showed a small FWHM ( $\Delta\omega$ ) of  $0.62^\circ$ , as shown in Fig. 6.3d.

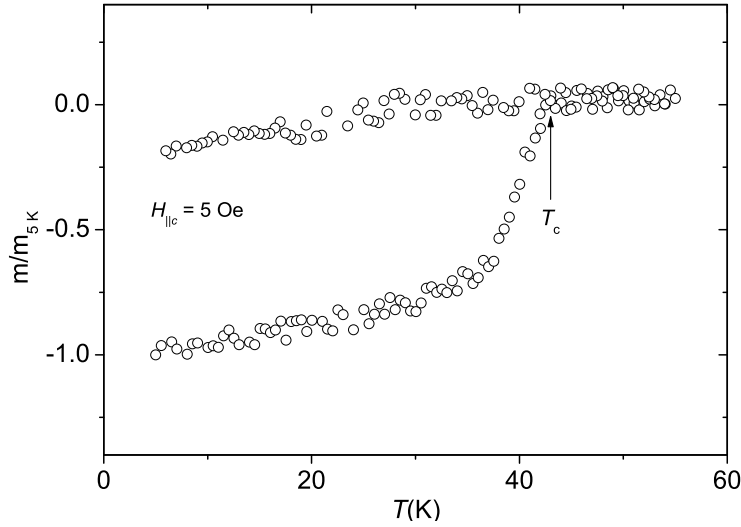
The (102)  $\phi$ -scan revealed a fourfold symmetry, indicative of epitaxial growth (see Fig. 6.3c). The epitaxial relation was confirmed to be  $(001)[100]\text{NdFeAs(O,F)} \parallel (001)[100]\text{MgO}$ . The average  $\Delta\phi$  value of the (102) Nd-1111 reflection was around  $1.26^\circ$ .



**Figure 6.3:**  $R(T)$  and structural characterisation of the Nd-1111 thin film. (a) Temperature dependence of the resistance before the ion-beam etching. A second transition is visible. (b) Comparison of the XRD of the Nd-1111 thin film before and after ion-beam etching. Impurity peaks from NdOF and FeAs are almost removed after the ion-beam etching. However, a small amount of the NdOF peak is still observable. This indicates that NdOF islands are still on top of the Nd-1111 layer. The Nd-1111 phase is grown without misorientations. (c)  $\phi$ -scan of the Nd-1111 thin film shows the fourfold symmetry with a  $\Delta\phi$  value of  $1.26^\circ$ . (d) Nd-1111 rocking curve scan of the (003) reflection, exhibits high quality with a  $\Delta\omega$  value of  $0.62^\circ$ .

## 6.4 Superconducting properties of NdFeAs(O,F)

A bridge of  $42 \mu\text{m}$  width and 1 mm length was fabricated by laser cutting (similar to Fig. 5.3). Before the ion-beam etching process, the  $I-V$  characteristic was measured using a PPMS (Quantum Design) at Nagoya University. The resistive measurement before the ion-beam etching process is shown in Fig. 6.3a. A second transition is visible presumably due to a different current path compared to the bridge-structured sample. This can be seen as step-like behaviour of the resistivity in the superconducting transition.



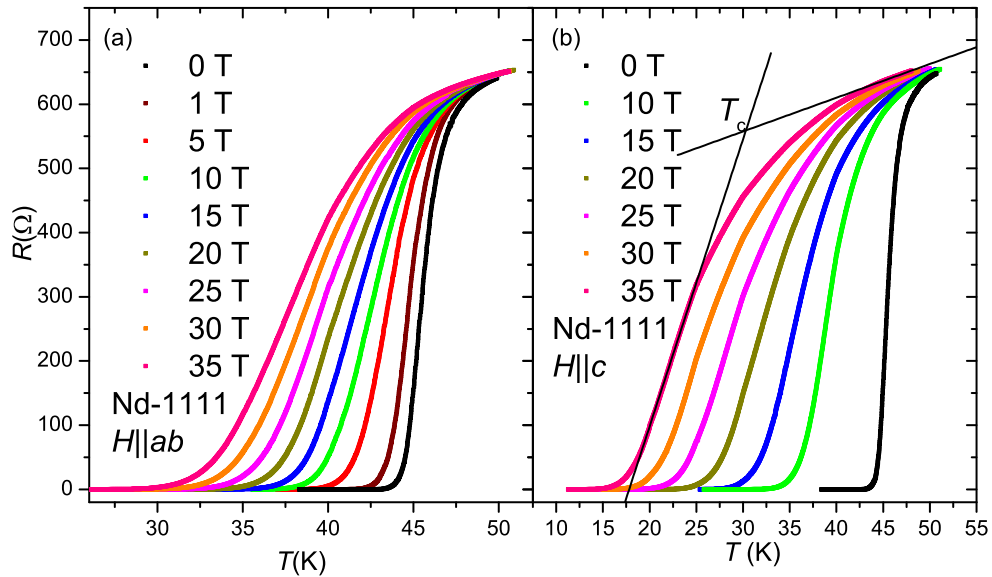
**Figure 6.4:** Temperature dependence of the magnetisation measurement done by a SQUID magnetometer with an applied field of 5 Oe. The  $T_c$  clearly coincides with the transport measurements. The top curve shows the field cooled measurement, the bottom curve shows the zero-field cooled measurement.

After the ion-beam etching, no second transition was observed in the  $R(T)$  measurements (see Fig. 6.5). This could be due to a smaller current path after laser cutting, that allows to avoid possible inhomogeneous areas. Bulk superconductivity with a transition temperature ( $T_c$ ) of 43 K was also confirmed by measuring the temperature dependence of the magnetisation (see Fig. 6.4). This  $T_c$  value coincides with the temperature, at which resistivity goes to zero. High-field transport measurements up to 35 T were carried out in the high-field dc facility at the NHMFL. A voltage criterion of  $1 \mu\text{V}/\text{cm}$  was employed for evaluating  $J_c$ . The magnetic field  $H$  was applied in maximum Lorentz force configuration during all measurements ( $H \perp J$ ).

The superconducting transition temperature  $T_{c,\text{onset}}$ , defined as the crossing point of the fit of the normal state resistance and the steepest slope of the superconducting transition, is 46.6 K in zero magnetic field (see Fig. 6.5b). Figures 6.5a and 6.5b show the temperature dependence of the resistance for both crystallographic directions measured in static fields up to 35 T. A significantly stronger shift of the superconducting transition to lower temperatures for  $H\parallel c$  as compared to  $H\parallel ab$  was observed. Similar to Sm-1111 and some cuprates, it is originating from thermally activated vortex motion for  $H\parallel c$  and the significant upper critical field ( $H_{c2}$ ) anisotropy. The  $T_{c,\text{onset}}$  at 35 T for  $H\parallel c$  and  $H\parallel ab$  is 30.3 K and 42.7 K, respectively. The temperature dependence of  $H_{c2}$  was determined using the  $T_{c,\text{onset}}$  of the resistive measurements (see Fig. 6.6). The  $H_{c2}$  curves at  $T_c$  have a steep slope of  $-8.3 \text{ T/K}$  for  $H\parallel ab$  and a moderate slope of  $-2.3 \text{ T/K}$  for  $H\parallel c$ . The extrapolated upper critical field

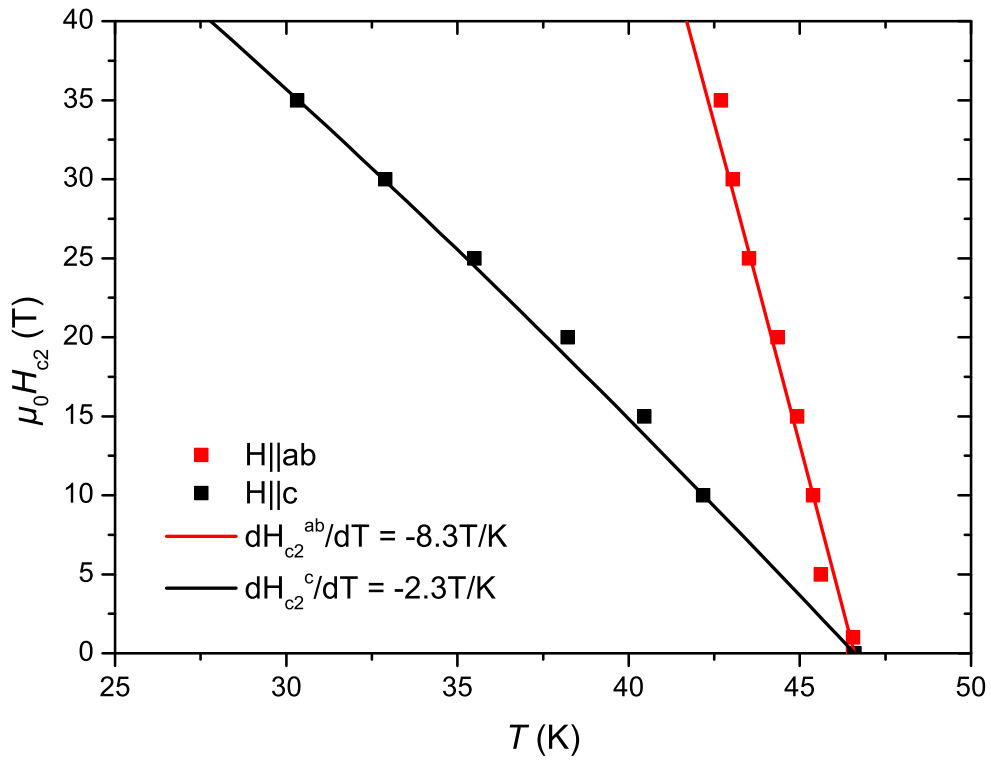
$H_{c2}(0)$  for  $H\parallel ab$  using the single-band WHH model [143] is about 270 T, which is very high compared to other FBS. The value in  $H\parallel c$  direction is 74 T which is moderate as compared to other FBS.

The extrapolated value of  $H_{c2}\parallel ab$  considerably exceeds the BCS paramagnetic limit  $H_p^{\text{BCS}}[\text{T}] = 1.84 T_c[\text{K}] \sim 90 \text{ T}$  [193]. However, in the case of strong coupling, the BCS theory might strongly underestimate the paramagnetic limiting field. In this case,  $H_p = (1+\lambda)H_p^{\text{BCS}}$  applies. Taking into account  $\lambda \sim 2$  [194] for the "1111" system, the result is  $H_p \sim 270 \text{ T}$  which is comparable to the extrapolation using the WHH model. The analysis of the available experimental data did not show any noticeable flattening of the  $H_{c2}$  curves due to Pauli-paramagnetic effects. However, at low temperatures, some reduction of  $H_{c2}$  as compared to the extrapolation can be expected. Further, sizeable multi-band effects for  $H_{c2}$  are not expected, since in the case of the "1111" family, superconducting coupling is dominated by inter-band interaction. This leads to similar superconducting gaps for electron and hole Fermi-surfaces. Therefore, the Nd-1111 should effectively react like a single-band superconductor. These findings coincide with the results found in single crystals [188]. The anisotropy value  $\gamma_{H_{c2}} = 3.6$ , extrapolated from the WHH-fit, is very stable and does not show a temperature dependence at high temperatures.



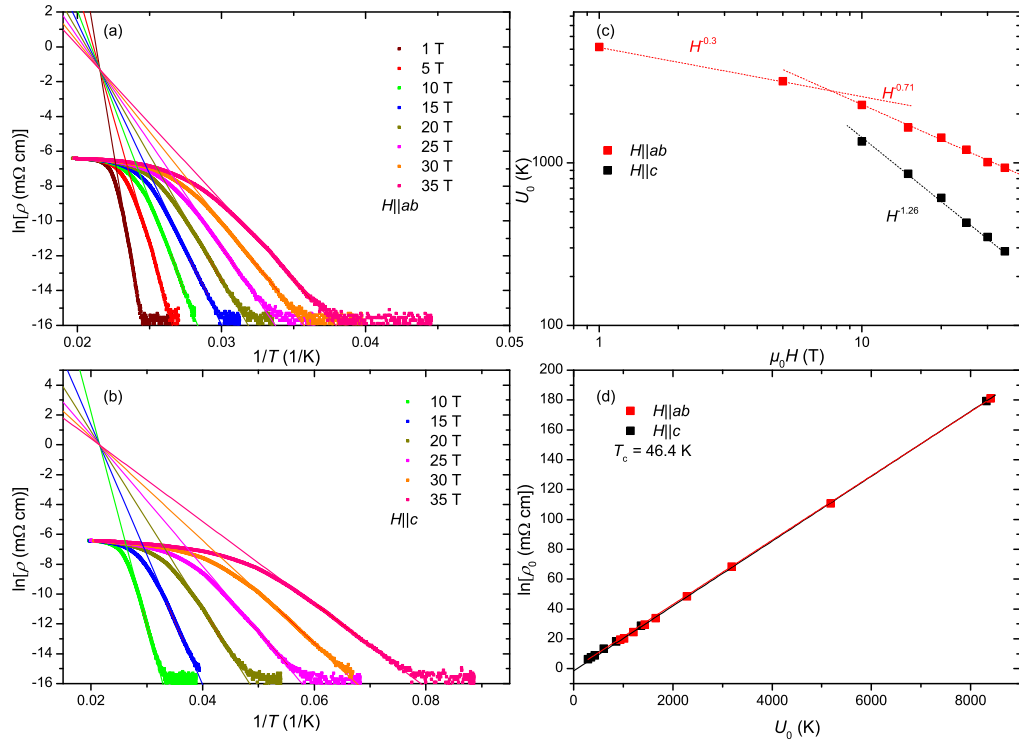
**Figure 6.5:** Resistive measurements in dependence of the applied magnetic field up to 35 T for (a)  $H\parallel ab$  direction and (b)  $H\parallel c$  direction after ion-beam etching. The two linear fits show the extraction of the  $T_{c,\text{onset}}$ . In this chapter  $T_c$  is defined as  $T_{c,\text{onset}}$ .

Figures 6.7a and 6.7b show the Arrhenius plots of resistivity for both crystallographic directions measured in static fields up to 35 T. The activation energy  $U_0(H)$  for vortex

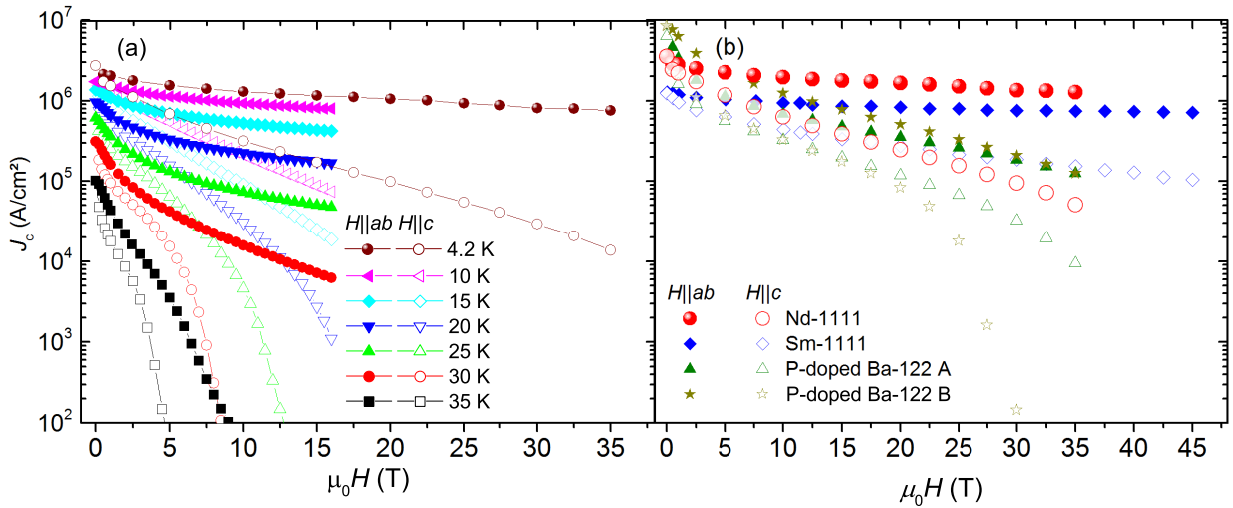


**Figure 6.6:** Temperature dependence of  $\mu_0 H_{c2}$  of the Nd-1111 thin film extracted from the  $T_{c,onset}$  of the resistive measurements with the corresponding single-band WHH-fits. From this fit the expected  $\mu_0 H_{c2}(0K)$  for  $H||ab$  direction (red) is around 270 T which is extremely high. The slope values are valid near  $T_c$ .

motion is estimated by the model of thermally activated flux flow [165] and is done similar to the investigations for Sm-1111 (see Chapter 5). Figure 6.7c shows the field dependence of the activation energy. For  $H||ab$ , in the field range  $1 \text{ T} < \mu_0 H < 8 \text{ T}$ , an  $\alpha$  value of -0.3 is observed. For higher fields, the dependency changes to  $\alpha = -0.71$ , suggesting a crossover from plastic to collective pinning at around  $\mu_0 H \sim 8 \text{ T}$  [166]. For  $H||c$  above 10 T, an  $\alpha$  value of -1.26 is extracted. The lower field regions have not yet been measured. The  $\ln \rho$  in dependence on the activation energy,  $U_0$ , has been evaluated and plotted in Fig. 6.7d. The analysis using the Arrhenius plot gives the before-measured  $T_c$  with a value of 46.4 K (determined from the slope of the fit) reassuring a reasonable criterion was taken for  $H_{c2}$ .



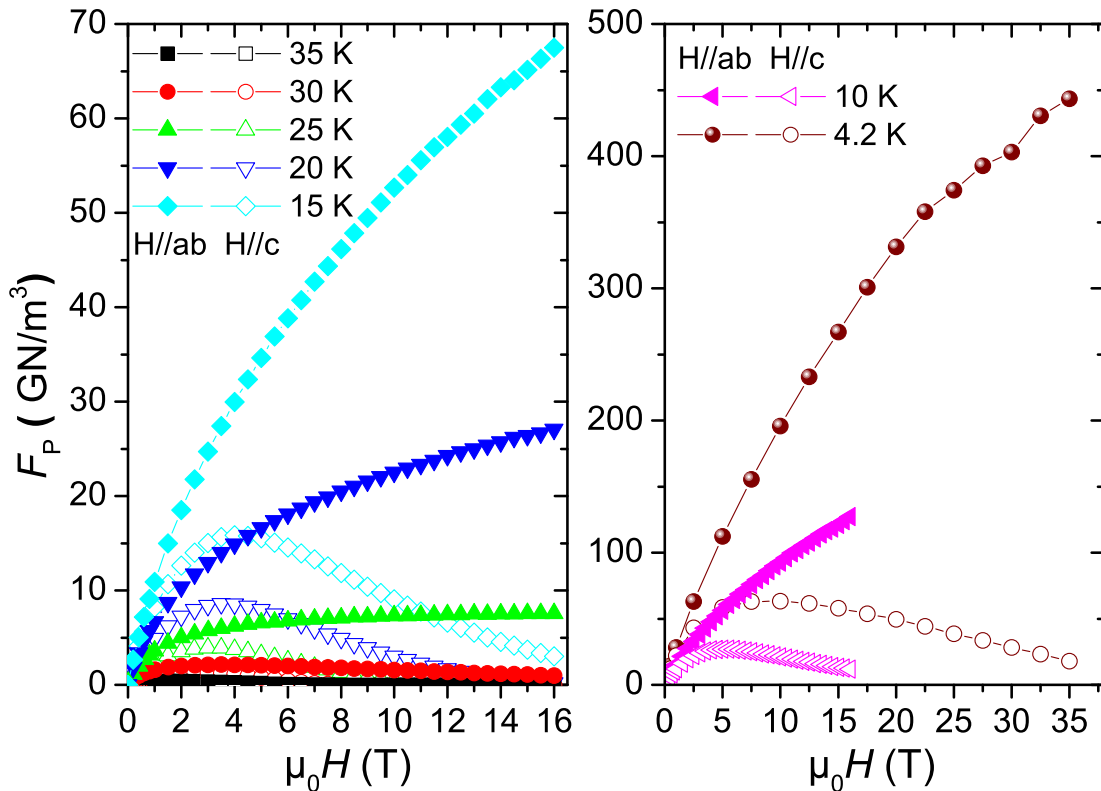
**Figure 6.7:** Arrhenius plot of  $\rho$  at various magnetic fields (a) parallel to the  $ab$ -plane and (b) parallel to the  $c$ -axis. (c) Field dependence of the activation energy. The slope of the fit in  $H \parallel ab$  direction changes around 8 T, suggesting a different dominant pinning mechanism. (d) Relationship of  $\ln \rho_0$  and  $U_0$  for both main directions.



**Figure 6.8:** (a) Field and its orientation dependence of  $J_c$  for Nd-1111 measured at various temperatures. (b) Field dependence of  $J_c$  at 4.2 K in both major crystallographic directions for the Nd-1111 thin film in comparison to P-doped Ba-122 and Sm-1111 thin films which are presented in this work in Chapter 4 and Chapter 5.



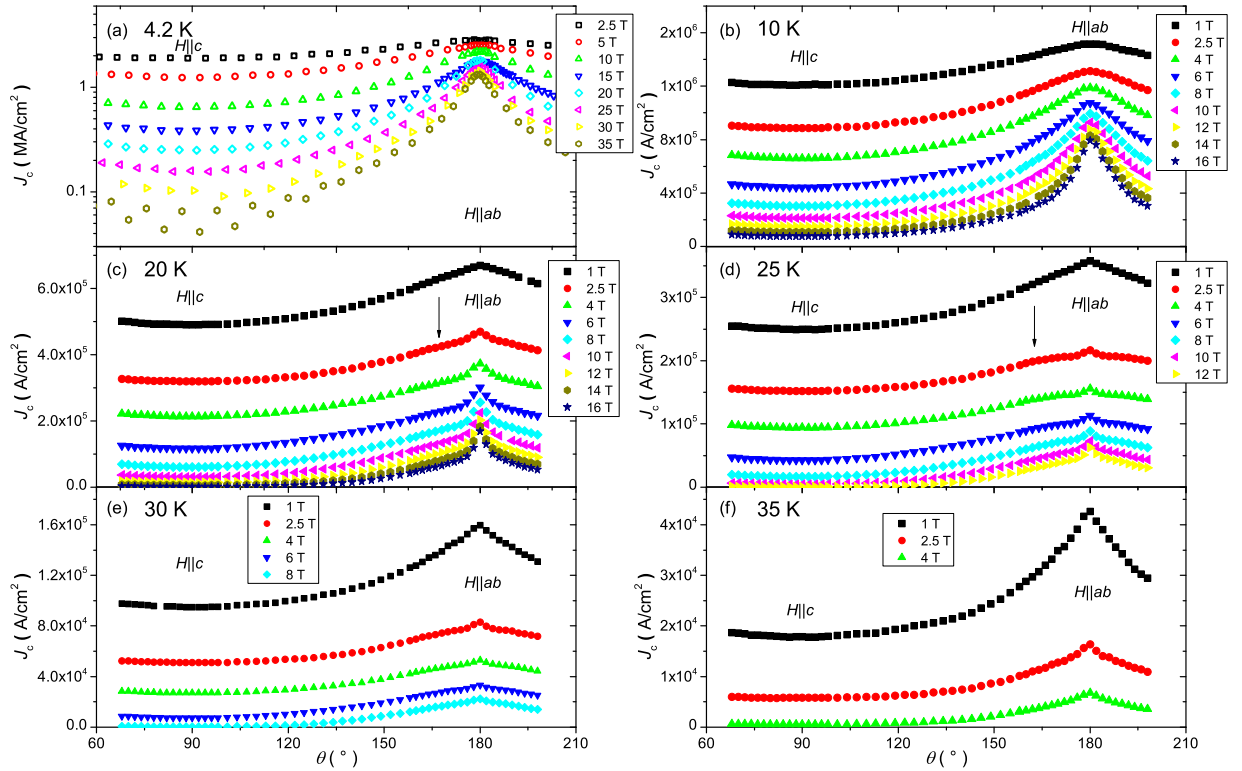
The field and its orientation dependence of  $J_c$  for Nd-1111 at various temperatures is displayed in Fig. 6.8a. The resulting pinning force density is shown in Fig. 6.9. For comparison, the field dependence of  $J_c$  for various FBS (discussed in Chapter 4 and Chapter 5) for both principle crystallographic directions measured up to 45 T and 35 T, respectively, is displayed in Fig. 6.8b [147, 195]. The self-field  $J_c$  of the NdFeAs(O,F) thin film is about  $3.5 \text{ MA/cm}^2$ . For an applied field in  $H\parallel ab$  direction, Nd-1111 has a very stable, nearly field-independent  $J_c$ . The  $J_c$  at 35 T exceeds  $1.2 \text{ MA/cm}^2$ . The shape of the curve is very similar to Sm-1111, despite its higher values, which makes it interesting for applications. For  $H\parallel c$ , the values decrease more rapidly, but still,  $J_c$  at 35 T is higher than  $5 \times 10^4 \text{ A/cm}^2$ . The behaviour for  $H\parallel ab$  can be explained by the presence of intrinsic pinning similar to Sm-1111: A combination of extrinsic and intrinsic pinning, where, at a certain field strength, the intrinsic pinning dominates  $J_c$  (see Fig. 5.8).



**Figure 6.9:** Field dependence of the pinning force density,  $F_p$ , at various temperatures. Because of the immense strength of the pinning force density for 4.2 K and 10 K, the data are shown in its own scaling on the right side.

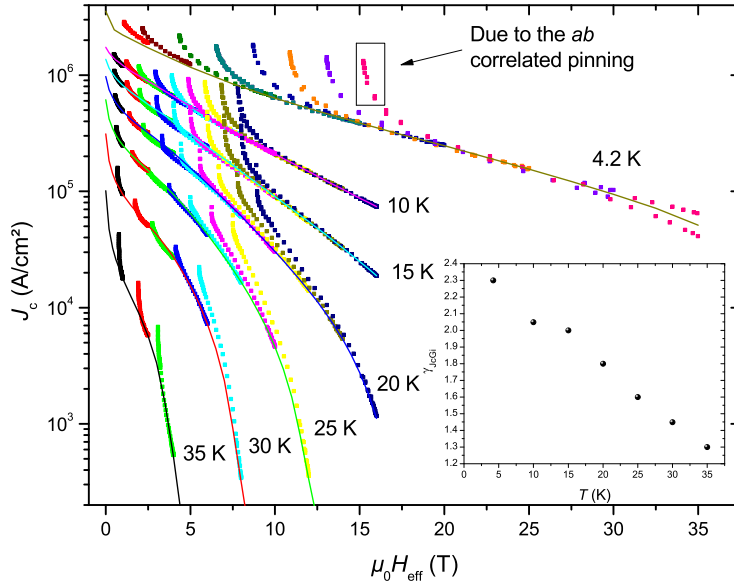
The resulting pinning force density,  $F_p$ , at various temperatures reveals very high values for  $H\parallel ab$ , increasing with increasing applied magnetic field, and moderate values for  $H\parallel c$  exhibiting a maximum around 10 T decreasing with increasing field (see Fig. 6.9). In

Fig. 6.10, the angular dependence of  $J_c$  at various temperatures is shown for different applied magnetic fields. A maximum of  $J_c$  was measured in  $H\parallel ab$  direction, decreasing for a closer proximity to  $H\parallel c$ . No  $c$ -axis peaks in  $J_c(\theta)$  are visible. With increasing temperature, the shape of the  $ab$  peak changes, indicating a change of the pinning mechanism at a certain temperature similar to the results found in Sm-1111. For 20 K (Fig. 6.10c) and 25 K (Fig. 6.10d), a small shoulder is forming close to the  $H\parallel ab$  direction, indicating the existence of extrinsic pinning.



**Figure 6.10:** Angle dependence of  $J_c$  at various temperatures: (a) 4.2 K, due to the measurement in the high-field magnet, the scale is different. (b) 10 K (c) 20 K, the shape of the  $ab$  peak seems to change with high fields, getting more pronounced for (d) 25 K, (e) 30 K and (f) 35 K. At 20 K (c) and 25 K (d) a small shoulder seems to form, indicated by the arrows.

Figure 6.11 shows the anisotropic Ginzburg Landau scaling where the  $J_c$  as a function of the effective field,  $\mu_0 H_{\text{eff}}$ , in  $c$ -direction is plotted. This scaling is described in more detail in Chapter 5. This is calculated with the  $J_c$  anisotropy ( $\gamma_{J_c G_i}$ ) as a free parameter. The resulting  $\gamma_{J_c G_i}$  values depend on the temperature and are different from the  $H_{c2}$  anisotropy near  $T_c$ , reaching from 1.4 for high temperatures up to 2.3 for low temperatures (see inset of Fig. 6.11). The correlated pinning for the  $ab$  plane is clearly visible by the upturn of  $J_c$  at low  $H_{\text{eff}}$ . Extrinsic pinning seems to dominate this field and temperature region.



**Figure 6.11:** Ginzburg Landau scaling of the angle dependence of  $J_c$  for different temperatures. The inset shows the temperature dependence of the  $J_c$  anisotropy  $\gamma_{J_c G_i}$ . The solid lines present the measured data [ $J_c(H)$ ] for  $H||c$  (see Fig. 6.8).

## 6.5 Summary of the chapter

NdFeAs(O,F) thin films have been grown epitaxially with high phase purity on MgO (001) substrates by MBE, achieving a high  $T_c$  value of 46.6 K. The field dependence of  $\rho(T)$  has been measured up to 35 T. A significant broadening of the transition in  $H||c$  direction was found and nearly no change in the normal state resistivity due to the observation of magnetoresistance.  $H_{c2}$  shows an anisotropy of  $\gamma_{H_{c2}} = 3.6$  at high temperatures, which is different from the  $J_c$  anisotropy  $\gamma_{J_c G_i} = 2.3$  at low temperatures. The extrapolated  $\mu_0 H_{c2}(0)$  was found to be 270 T for the  $H||ab$  direction and 74 T for the  $H||c$  direction. NdFeAs(O,F) behaves like a single-band superconductor. The Arrhenius plots of the  $\rho(T)$  and the following calculation of the activation energy indicate a change of the pinning mechanism around 8 T for  $H||ab$  from plastic to collective pinning.

The field and angle dependence of  $J_c$  was measured up to 35 T, as well as in a PPMS up to 16 T for higher temperatures. The self-field  $J_c$  at 4.2 K was found to be 3.5 MA/cm<sup>2</sup>. With applied magnetic field, the  $J_c$  in  $H||ab$  direction showed record values and a very stable in-field behaviour up to 35 T: The  $J_c$  at 35 T is higher than 1.2 MA/cm<sup>2</sup>. For  $H||c$ ,  $J_c$  is still higher than  $5 \times 10^4$  A/cm<sup>2</sup> at 35 T. The  $F_p$  shows very high values, for  $H||ab$  and temperatures below 30 K, the  $F_p$  is still rising for increasing magnetic field. For  $H||c$ , a temperature depending maximum is visible, decreasing with increasing temperature. The

angular dependence of  $J_c$  exhibits a changing shape of the  $ab$ -peak above 20 K, indicating a change of the dominant pinning mechanism in the film. A small contribution of  $c$ -axis correlated pinning is assumed in the anisotropy scaling investigations.

## 7 Summary

In this thesis, fluoride substrates were introduced for the efficient epitaxial growth of superconducting Co-doped Ba-122. The first successful growth of Co-doped Ba-122 on single-crystalline SrF<sub>2</sub> (001), BaF<sub>2</sub> (001) and CaF<sub>2</sub> (001) substrates by PLD has been shown [96]. All films have been grown epitaxially and without impurity phases, confirmed by XRD and TEM investigations. A small interfacial layer was observed in TEM investigations which is assumed to be BaF<sub>2</sub> rich. The best quality could be achieved for thicker films grown on CaF<sub>2</sub> at slightly higher temperature. The high in-field  $J_c$  is nearly isotropic for lower temperatures up to 9 T which can also be seen in the angle dependence of  $J_c$ . The fluoride substrates, therefore, offer a great opportunity to improve the investigations of Co-doped Ba-122 because of the relatively easy way of fabrication, especially for transport measurements that can be done without the hindering shunting effect of the before-used Fe buffer layer [79] [110].

Investigations of unusually high critical currents found during first high-field measurements in P-doped Ba-122 thin films grown by MBE onto MgO (001) substrates have been undertaken [195]. Both films have been grown epitaxially proven by XRD and TEM investigations. Although the P content of both, Sample A and Sample B, measured by EPMA, is rather small around 0.2, the samples show a high  $T_c$  of around 30 K. The exponent  $n$ -value evaluated from the equation  $\rho = \rho_0 + AT^n$  in the normal state resistivity is close to unity, suggesting a non-Fermi-liquid state. Those results support the idea that both samples are optimally doped resulting from tensile strain transferred from the MgO substrates. The field and angular dependence of  $J_c$  was measured up to 35 T in static fields at 4.2 K; its temperature dependence was investigated using a PPMS up to 16 T. From the anisotropic Ginzburg Landau-scaling approach for the angle dependent  $J_c$  data of Sample B, the  $\gamma_{J_c G_1}$ -value was observed to increase with increasing temperature, which follows the  $H_{c2}$  anisotropy. These results are similar to Co-doped Ba-122 [78] [172] as well as LaFeAs(O,F) [196]. Sample A, a high quality film without any visible defects, exhibited a self-field  $J_c$  of 6.3 MA/cm<sup>2</sup> at 4.2 K. Sample B, also of high quality, presents even larger  $J_c$  of 8.5 MA/cm<sup>2</sup> at 4.2 K. It can be stated that in optimally P-doped Ba-122, a very small amount of structural defects results in a very strong pinning of the flux lines due to

a sharp enhancement of the vortex core energy, resulting in  $\delta l$  pinning. Therefore, these new results offer valuable information about the intrinsic material properties of P-doped Ba-122. Further investigations of the quantum critical point and the possible existence of two nematic transitions in the superconducting phase diagram are underway and provide new ideas about the physical working mechanism of superconductivity in P-doped Ba-122. Due to its high  $J_c$ , this material may be a good candidate for wire and tape applications. Bicrystal experiments, which have already been conducted, suggest a low dependence of the  $J_c$  on the grain boundary angle. At a grain boundary angle of  $24^\circ$ ,  $J_c$  still provides values above  $10^6$  A/cm<sup>2</sup> demonstrating the high potential of P-doped Ba-122 and the need for further efforts in investigating its properties.

The transport properties of an epitaxial Sm-1111 thin film grown onto a CaF<sub>2</sub> (001) substrate by MBE have been studied for the first time [147]. The field and angular dependence of  $J_c$  have been measured in static fields up to 45 T. The competition of the extrinsic and intrinsic pinning in the sample is discussed and reveals a transition around 28 T. In the temperature range from 30 K  $\sim$  40 K the intrinsic pinning starts being effective. These investigations stimulate further work in the direction of applications. PIT Sm-1111 wire preparation which necessitate bicrystal experiments would be a next step for obtaining important information in this material class.

A first report on high-field measurements of an epitaxial Nd-1111 thin film grown on MgO (001) by MBE is presented. The field and angular dependence of  $J_c$  was measured up to 35 T in static fields at 4.2 K, its temperature dependence was investigated in a PPMS up to 16 T. Pinning investigations revealed a competition of extrinsic and intrinsic pinning similar to the Sm-1111 thin films. The field dependence of  $J_c$  was found to be very stable, at 35 T and 4.2 K the  $J_c$  still exceeds 1 MA/cm<sup>2</sup>. The high  $T_c$  as well as the investigated high-field properties are very promising for using this material class in applications.

Each investigated superconducting material provides its advantages and disadvantages in high magnetic fields: Low anisotropy and very high self-field  $J_c$  for P-doped Ba-122 with very interesting possibilities for flux pinning due to strong variations of the vortex core energy. The Sm-1111 film provides a very stable field dependence of high  $J_c$  in both major field directions. Hereby the Nd-1111 film offers the highest values for the field dependence of  $J_c$  in  $H\parallel ab$  direction, resulting in extremely high pinning force densities as well as high  $J_c$  for  $H\parallel c$ , despite exhibiting anisotropy values around 3. These measurements provide knowledge for further investigations in the direction of applications. The preparation of thin films on IBAD-MgO substrates, which in some cases has already been done, is a necessary step. Grain boundary studies of the materials which can be investigated via the

preparation of thin films on bicrystal substrates can provide an outlook for wires and tapes applications.





# Bibliography

- [1] J.G. Bednorz and K.A. Müller. Possible high  $T_c$  superconductivity in the Ba-La-Cu-O system. *Z Phys B Cond Mat*, 64(2):189–193, 1986.
- [2] J. Nagamatsu, N. Nakagawa, T. Muranaka, Y. Zenitani, and J. Akimitsu. Superconductivity at 39 K in magnesium diboride. *Nature*, 410(6824):63–64, 2001.
- [3] Y. Kamihara, H. Hiramatsu, M. Hirano, R. Kawamura, H. Yanagi, T. Kamiya, and H. Hosono. Iron-Based Layered Superconductor: LaOFeP. *Journal of the American Chemical Society*, 128(31):10012–10013, 2006. PMID: 16881620.
- [4] Y. Kamihara, T. Watanabe, M. Hirano, and H. Hosono. Iron-based layered superconductor La[O<sub>1-x</sub>F<sub>x</sub>]FeAs (x=0.05-0.12) with  $T_c=26$  K. *J. Am. Chem. Soc.*, 130(11):3296, 2008.
- [5] D. C. Johnston. The puzzle of high temperature superconductivity in layered iron pnictides and chalcogenides. *Advances in Physics*, 59(6):803–1061, 2010.
- [6] I.I. Mazin and J. Schmalian. Pairing symmetry and pairing state in ferropnictides: Theoretical overview. *Physica C*, 469(9–12):614–627, 2009.
- [7] P. Richard, T. Qian, and H. Ding. ARPES measurements of the superconducting gap of Fe-based superconductors and their implications to the pairing mechanism. *ArXiv e-prints*, 1503.07269, 2015.
- [8] M. D. Lumsden and A. D. Christianson. Magnetism in Fe-based superconductors. *J. Phys-Condens. Mat.*, 22(20):203203, 2010.
- [9] G. R. Stewart. Superconductivity in iron compounds. *Rev. Mod. Phys.*, 83:1589–1652, 2011.
- [10] A. Chubukov. Pairing Mechanism in Fe-Based Superconductors. *Annu. Rev. Cond. Matt. Phys.*, 3(1):57–92, 2012.
- [11] S. Haindl, M. Kitzun, S. Oswald, C. Hess, B. Büchner, S. Kölling, L. Wilde, T. Thersleff, V. V. Yurchenko, M. Jourdan, H. Hiramatsu, and H. Hosono. Thin film growth of Fe-based superconductors: from fundamental properties to functional devices. A comparative review. *Rep. Prog. Phys.*, 77(4):046502, 2014.
- [12] A. K. Ganguli, J. Prakash, and G. S. Thakur. The iron-age of superconductivity: structural correlations and commonalities among the various families having -Fe-Pn-slabs (Pn = P, As and Sb). *Chem. Soc. Rev.*, 42:569–598, 2013.

- [13] H. Gosh and S. Sen. Iron based superconductors: A brief overview. *ArXiv e-prints*, 1408.3244, 2014.
- [14] H. Hosono and K. Kuroki. Iron-based superconductors: Current status of materials and pairing mechanism. *Physica C: Superconductivity and its Applications*, 514(0):399 – 422, 2015. Superconducting Materials: Conventional, Unconventional and Undetermined.
- [15] W. Buckel and R. Kleiner. *Supraleitung: Grundlagen und Anwendungen*. Lehrbuch Physik. Wiley-VCH, 1994.
- [16] J. Bardeen, L. N. Cooper, and J. R. Schrieffer. Theory of Superconductivity. *Phys. Rev.*, 108(5):1175–1204, 1957.
- [17] M. Tinkham. *Introduction to superconductivity*. Dover books on physics and chemistry. Dover Publications, 1996.
- [18] M. Yi, D. H. Lu, J. G. Analytis, J.-H. Chu, S.-K. Mo, R.-H. He, R. G. Moore, X. J. Zhou, G. F. Chen, J. L. Luo, N. L. Wang, Z. Hussain, D. J. Singh, I. R. Fisher, and Z.-X. Shen. Electronic structure of the  $\text{BaFe}_2\text{As}_2$  family of iron-pnictide superconductors. *Phys. Rev. B*, 80(2):024515, 2009.
- [19] D. J. Singh. Electronic structure and doping in  $\text{BaFe}_2\text{As}_2$  and  $\text{LiFeAs}$ : Density functional calculations. *Phys. Rev. B*, 78(9):094511, 2008.
- [20] L. Boeri, O. V. Dolgov, and A. A. Golubov. Is  $\text{LaFeAsO}_{1-x}\text{F}_x$  an electron-phonon superconductor? *Phys. Rev. Lett.*, 101(2):026403, 2008.
- [21] G. Blatter, M. V. Feigel'man, V. B. Geshkenbein, A. I. Larkin, and V. M. Vinokur. Vortices in high-temperature superconductors. *Rev. Mod. Phys.*, 66:1125–1388, 1994.
- [22] K. Matsumoto and P. Mele. Artificial pinning center technology to enhance vortex pinning in YBCO coated conductors. *Supercond. Sci. Technol.*, 23(1):014001, 2010.
- [23] S. Awaji, K. Watanabe, and N. Kobayashi. Crossover from intrinsic to extrinsic pinning for  $\text{YBa}_2\text{Cu}_3\text{O}_7$  films. *Cryogenics*, 39(7):569 – 577, 1999.
- [24] H. K pfer, I. Apfelstedt, R. Fl kiger, C. Keller, R. Meier-Hirmer, B. Runtsch, A. Turowski, U. Wiech, and T. Wolf. Intragrain junctions in  $\text{YBa}_2\text{Cu}_3\text{O}_{7-x}$  ceramics and single crystals. *Cryogenics*, 29(3, Supplement):268 – 280, 1989. International Conference on Critical Currents in High-Temperature Superconductors.
- [25] M. Putti, I. Pallecchi, E. Bellingeri, M. R. Cimberle, M. Tropeano, C. Ferdeghini, A. Palenzona, C. Tarantini, A. Yamamoto, J. Jiang, J. Jaroszynski, F. Kametani, D. Abraimov, A. Polyanskii, J. D. Weiss, E. E. Hellstrom, A. Gurevich, D. C. Larbalestier, R. Jin, B. C. Sales, A. S. Sefat, M. A. McGuire, D. Mandrus, P. Cheng, Y. Jia, H. H. Wen, S. Lee, and C. B. Eom. New Fe-based superconductors: properties relevant for applications. *Supercond. Sci. Technol.*, 23(3):034003, 2010.

- [26] C. Buzea and T. Yamashita. Review of the superconducting properties of  $\text{MgB}_2$ . *Supercond. Sci. Technol.*, 14(11):R115, 2001.
- [27] B. T. Matthias, T. H. Geballe, S. Geller, and E. Corenzwit. Superconductivity of  $\text{Nb}_3\text{Sn}$ . *Phys. Rev.*, 95:1435–1435, 1954.
- [28] J. Paglione and R. L. Greene. High-temperature superconductivity in iron-based materials. *Nat. Phys.*, 6(9):645–658, 2010.
- [29] L. Shan, Y. Wang, X. Zhu, G. Mu, L. Fang, C. Ren, and Wen H.-H. Point-contact spectroscopy of iron-based layered superconductor  $\text{LaO}_{0.9}\text{F}_{0.1-\delta}\text{FeAs}$ . *EPL*, 83:57004, 2008.
- [30] H. Luetkens, H.-H. Klauss, R. Khasanov, A. Amato, R. Klingeler, I. Hellmann, N. Leps, A. Kondrat, C. Hess, A. Köhler, G. Behr, J. Werner, and B. Büchner. Field and Temperature Dependence of the Superfluid Density in  $\text{LaFeAsO}_{1-x}\text{F}_x$  Superconductors: A Muon Spin Relaxation Study. *Phys. Rev. Lett.*, 101(9):097009, 2008.
- [31] K. Kuroki, S. Onari, R. Arita, H. Usui, Y. Tanaka, H. Kontani, and H. Aoki. Unconventional Pairing Originating from the Disconnected Fermi Surfaces of Superconducting  $\text{LaFeAsO}_{1-x}\text{F}_x$ . *Phys. Rev. Lett.*, 101(8):087004, 2008.
- [32] D. J. Singh and M.-H. Du. Density Functional Study of  $\text{LaFeAsO}_{1-x}\text{F}_x$ : A Low Carrier Density Superconductor Near Itinerant Magnetism. *Phys. Rev. Lett.*, 100(23):237003, 2008.
- [33] Z.-A. Ren and Z.-X. Zhao. Research and Prospects of Iron-Based Superconductors. *Advanced Materials*, 21(45):4584–4592, 2009.
- [34] D. Mandrus, A. S. Sefat, M. A. McGuire, and B. C. Sales. Materials Chemistry of  $\text{BaFe}_2\text{As}_2$ : A Model Platform for Unconventional Superconductivity. *Chem. Mater.*, 22(3):715–723, 2010.
- [35] D. Johrendt, C. Felser, O. Jepsen, O.K. Andersen, A. Mewis, and J. Rouxel. LMTO Band Structure Calculations of  $\text{ThCr}_2\text{Si}_2$ -Type Transition Metal. *J. Solid State Chem.*, 130:254–265(12), 1997.
- [36] Z.-A. REN, W. LU, J. YANG, W. YI, X.-L. SHEN, Z.-C. LI, G.-C. CHE, X.-L. DONG, L.-L. SUN, F. ZHOU, and Z.-X. ZHAO. Superconductivity at 55K in Iron-Based F-Doped Layered Quaternary Compound  $\text{Sm}[\text{O}_{1-x}\text{F}_x]\text{FeAs}$ . *Chinese Physics Letters*, 25(6):2215, 2008.
- [37] H. Kito, H. Eisaki, and A. Iyo. Superconductivity at 54 K in F-Free  $\text{NdFeAsO}_{1-y}$ . *J. Phys. Soc. Jpn*, 77(6):063707, 2008.
- [38] M. Rotter, M. Tegel, and D. Johrendt. Superconductivity at 38 K in the Iron Arsenide  $(\text{Ba}_{1-x}\text{K}_x)\text{Fe}_2\text{As}_2$ . *Phys. Rev. Lett.*, 101(10):107006, 2008.

- [39] T. Katase, H. Hiramatsu, T. Kamiya, and H. Hosono. Magnetic scattering and electron pair breaking by rare-earth-ion substitution in  $\text{BaFe}_2\text{As}_2$  epitaxial films. *New J. Phys.*, 15(7):073019, 2013.
- [40] N. Ni, M. E. Tillman, J.-Q. Yan, A. Kracher, S. T. Hannahs, S. L. Bud'ko, and P. C. Canfield. Effects of Co substitution on thermodynamic and transport properties and anisotropic  $H_{c2}$  in  $\text{Ba}(\text{Fe}_{1-x}\text{Co}_x)_2\text{As}_2$  single crystals. *Phys. Rev. B*, 78:214515, 2008.
- [41] E. D. Mun, S. L. Bud'ko, N. Ni, A. N. Thaler, and P. C. Canfield. Thermoelectric power and Hall coefficient measurements on  $\text{BaFe}_{1-x}\text{T}_x)_2\text{As}_2$  ( $T = \text{Co}$  and  $\text{Cu}$ ). *Phys. Rev. B*, 80:054517, 2009.
- [42] N. Ni, A. Thaler, J. Q. Yan, A. Kracher, E. Colombier, S. L. Bud'ko, P. C. Canfield, and S. T. Hannahs. Temperature versus doping phase diagrams for  $\text{Ba}(\text{Fe}_{1-x}\text{TM}_x)_2\text{As}_2$  ( $\text{TM} = \text{Ni}, \text{Cu}, \text{Cu/Co}$ ) single crystals. *Phys. Rev. B*, 82:024519, 2010.
- [43] F. Rullier-Albenque, D. Colson, A. Forget, P. Thuéry, and S. Poissonnet. Hole and electron contributions to the transport properties of  $\text{Ba}(\text{Fe}_{1-x}\text{Ru}_x)_2\text{As}_2$  single crystals. *Phys. Rev. B*, 81:224503, 2010.
- [44] S. Jiang, H. Xing, G. Xuan, C. Wang, Z. Ren, C. Feng, J. Dai, Z. Xu, and G. Cao. Superconductivity up to 30 K in the vicinity of the quantum critical point in  $\text{BaFe}_2(\text{As}_{1-x}\text{P}_x)_2$ . *J. Phys.: Cond. Mat.*, 21(38):382203, 2009.
- [45] S. A. J. Kimber, A. Kreyssig, Y.-Z. Zhang, H. O. Jeschke, R. Valenti, F. Yokaichiya, E. Colombier, J. Yan, T. C. Hansen, T. Chatterji, R. J. McQueeney, P. C. Canfield, A. I. Goldman, and D. N. Argyriou. Similarities between structural distortions under pressure and chemical doping in superconducting  $\text{BaFe}_2\text{As}_2$ . *Nat Mater*, 8(6):471–475, 2009.
- [46] J. Engelmann, V. Grinenko, P. Chekhonin, W. Skrotzki, D.V. Efremov, S. Oswald, K. Iida, R. Hühne, J. Hänisch, M. Hoffmann, F. Kurth, L. Schultz, and B. Holzapfel. Strain induced superconductivity in the parent compound  $\text{BaFe}_2\text{As}_2$ . *Nat. Commun.*, 4:2877, 2013.
- [47] M. Rotter, M. Pangerl, M. Tegel, and D. Johrendt. Superconductivity and crystal structures of  $(\text{Ba}_{1-x}\text{K}_x)\text{Fe}_2\text{As}_2$  ( $x=0.1$ ). *Angew. Chem. Int. Edit.*, 47(41):7949–7952, 2008.
- [48] E. Colombier, S. L. Bud'ko, N. Ni, and P. C. Canfield. Complete pressure-dependent phase diagrams for  $\text{SrFe}_2\text{As}_2$  and  $\text{BaFe}_2\text{As}_2$ . *Phys. Rev. B*, 79:224518, 2009.
- [49] A. Ichimiya and P.I. Cohen. *Reflection high-energy electron diffraction*. Cambridge University Press, 2004.
- [50] H. Fukazawa, N. Takeshita, T. Yamazaki, K. Kondo, K. Hirayama, Y. Kohori, K. Miyazawa, H. Kito, H. Eisaki, and A. Iyo. Suppression of Magnetic Order by Pressure in  $\text{BaFe}_2\text{As}_2$ . *J. Phys. Soc. Jpn*, 77(10):105004, 2008.

- [51] K. Matsubayashi, N. Katayama, K. Ohgushi, A. Yamada, K. Munakata, T. Matsumoto, and Y. Uwatoko. Intrinsic Properties of  $\text{AFe}_2\text{As}_2$  ( $A = \text{Ba}, \text{Sr}$ ) Single Crystal under Highly Hydrostatic Pressure Conditions. *J. Phys. Soc. Jpn.*, 78(7):073706, 2009.
- [52] M.A. Herman, W. Richter, and H. Sitter. *Epitaxy: physical principles and technical implementation*. Springer, 2004.
- [53] L. B. Freund and S. Suresh. *Thin film Materials*. Cambridge University Press, 2003.
- [54] M. A. Herman and H. Sitter. *Molecular Beam Epitaxy - Fundamentals and Current Status*. Springer, 1996.
- [55] D. B. Chrisey and G. K. Hubler. *Pulsed Laser Deposition of Thin Films*. John Wiley & Sons, Inc., 1994.
- [56] J. Engelmann. Herstellung und Charakterisierung von  $\text{NbN}/\text{SmCo}_5$  Bilagen. Diploma thesis, TU Dresden, 2009.
- [57] J. A. Venables. Nucleation and growth processes in thin film formation. *Journal of Vacuum Science & Technology B*, 4(4):870–873, 1986.
- [58] C.J. Tsai and H.A. Atwater. Suppression of Island Formation During Initial Stages of  $\text{Ge}/\text{Si}(100)$  Growth by Ion-Assisted Molecular Beam Epitaxy. In *Symposium K – Materials Modification by Energetic Atoms and Ions*, volume 268 of *MRS Online Proceedings Library*, 1992.
- [59] E. Bellingeri, I. Pallecchi, R. Buzio, A. Gerbi, D. Marrè, M. R. Cimberle, M. Tropeano, M. Putti, A. Palenzona, and C. Ferdeghini.  $T_c=21\text{ K}$  in epitaxial  $\text{FeSe}_{0.5}\text{Te}_{0.5}$  thin films with biaxial compressive strain. *Appl. Phys. Lett.*, 96(10):102512, 2010.
- [60] M. Kidszun, S. Haindl, E. Reich, J. Hänisch, K. Iida, L. Schultz, and B. Holzapfel. Epitaxial  $\text{LaFeAsO}_{1-x}\text{F}_x$  thin films grown by pulsed laser deposition. *Supercond. Sci. Technol.*, 23(2):022002, 2010.
- [61] E. Backen, S. Haindl, T. Niemeier, R. Hühne, T. Freudenberger, J. Werner, G. Behr, L. Schultz, and B. Holzapfel. Growth and anisotropy of  $\text{La}(\text{O}, \text{F})\text{FeAs}$  thin films deposited by pulsed laser deposition. *Supercond. Sci. Technol.*, 21(12):122001, 2008.
- [62] S. Haindl, M. Kidszun, A. Kauffmann, K. Nenkov, N. Kozlova, J. Freudenberger, T. Thersleff, J. Hänisch, J. Werner, E. Reich, L. Schultz, and B. Holzapfel. High Upper Critical Fields and Evidence of Weak-Link Behavior in Superconducting  $\text{LaFeAsO}_{1-x}\text{F}_x$  Thin Films. *Phys. Rev. Lett.*, 104(7):077001, 2010.
- [63] T. Kawaguchi, H. Uemura, T. Ohno, R. Watanabe, M. Tabuchi, T. Ujihara, K. Takenaka, Y. Takeda, and H. Ikuta. Epitaxial Growth of  $\text{NdFeAsO}$  Thin Films by Molecular Beam Epitaxy. *Appl. Phys. Express*, 2(9):093002, 2009.

- [64] T. Kawaguchi, H. Uemura, T. Ohno, M. Tabuchi, T. Ujihara, K. Takenaka, Y. Takeda, and H. Ikuta. Epitaxial growth of LaFeAs(O,F) thin films by molecular beam epitaxy. *Physica C*, 471(21–22):1174–1176, 2011.
- [65] H. Uemura, T. Kawaguchi, T. Ohno, M. Tabuchi, T. Ujihara, Y. Takeda, and H. Ikuta. Substrate dependence of the superconducting properties of NdFeAs(O,F) thin films. *Solid State Commun.*, 152(8):735 – 739, 2012.
- [66] S. Ueda, S. Takeda, S. Takano, A. Mitsuda, and M. Naito. Molecular Beam Epitaxy Growth of Superconducting  $\text{Ba}_{1-x}\text{K}_x\text{Fe}_2\text{As}_2$  and SmFeAs(O,F) Films. *Jpn. J. Appl. Phys.*, 51(1R):010103, 2012.
- [67] S. Ueda, S. Takeda, S. Takano, A. Yamamoto, and M. Naito. High- $T_c$  and high- $J_c$  SmFeAs(O,F) films on fluoride substrates grown by molecular beam epitaxy. *Appl. Phys. Lett.*, 99(23):232505, 2011.
- [68] S. Ueda, T. Yamagishi, S. Takeda, S. Agatsuma, S. Takano, A. Mitsuda, and M. Naito. MBE growth of Fe-based superconducting films. *Physica C*, 471(21–22):1167 – 1173, 2011. The 23rd International Symposium on Superconductivity.
- [69] H. Hiramatsu, T. Katase, T. Kamiya, M. Hirano, and H. Hosono. Superconductivity in Epitaxial Thin Films of Co-Doped  $\text{SrFe}_2\text{As}_2$  with Bilayered FeAs Structures and their Magnetic Anisotropy. *Appl. Phys. Express*, 1(10):101702, 2008.
- [70] S. A. Baily, Y. Kohama, H. Hiramatsu, B. Maiorov, F. F. Balakirev, M. Hirano, and H. Hosono. Pseudoisotropic Upper Critical Field in Cobalt-Doped  $\text{SrFe}_2\text{As}_2$  Epitaxial Films. *Phys. Rev. Lett.*, 102:117004, 2009.
- [71] T. Katase, H. Hiramatsu, H. Yanagi, T. Kamiya, M. Hirano, and H. Hosono. Atomically-flat, chemically-stable, superconducting epitaxial thin film of iron-based superconductor, cobalt-doped  $\text{BaFe}_2\text{As}_2$ . *Solid State Commun.*, 149(47–48):2121 – 2124, 2009.
- [72] T. Katase, H. Hiramatsu, T. Kamiya, and H. Hosono. High Critical Current Density  $4\text{MA}/\text{cm}^2$  in Co-Doped  $\text{BaFe}_2\text{As}_2$  Epitaxial Films Grown on (La,Sr)(Al,Ta) $\text{O}_3$  Substrates without Buffer Layers. *Appl. Phys. Express*, 3(6):063101, 2010.
- [73] B. Maiorov, T. Katase, S. A. Baily, H. Hiramatsu, T. G. Holesinger, H. Hosono, and L. Civale. Liquid vortex phase and strong c -axis pinning in low anisotropy  $\text{BaCo}_x\text{Fe}_{2-x}\text{As}_2$  pnictide films. *Supercond. Sci. Technol.*, 24(5):055007, 2011.
- [74] K. Iida, J. Hänisch, R. Hühne, F. Kurth, M. Kitzun, S. Haindl, J. Werner, L. Schultz, and B. Holzapfel. Strong  $T_c$  dependence for strained epitaxial  $\text{Ba}(\text{Fe}_{1-x}\text{Co}_x)_2\text{As}_2$  thin films. *Appl. Phys. Lett.*, 95(19):192501, 2009.
- [75] S. Lee, J. Jiang, Y. Zhang, C. W. Bark, J. D. Weiss, C. Tarantini, C. T. Nelson, H. W. Jang, C. M. Folkman, S. H. Baek, A. Polyanskii, D. Abaimov, A. Yamamoto,

- J. W. Park, X. Q. Pan, E. E. Hellstrom, D. C. Larbalestier, and C. B. Eom. Template engineering of Co-doped  $\text{BaFe}_2\text{As}_2$  single-crystal thin films. *Nat. Mater.*, 9(5):397–402, 2010.
- [76] T. Thersleff, K. Iida, S. Haindl, M. Kidszun, D. Pohl, A. Hartmann, F. Kurth, J. Hänisch, R. Hühne, B. Rellinghaus, L. Schultz, and B. Holzapfel. Coherent interfacial bonding on the FeAs tetrahedron in Fe/Ba( $\text{Fe}_{1-x}\text{Co}_x$ ) $_2\text{As}_2$  bilayers. *Appl. Phys. Lett.*, 97(2):022506, 2010.
- [77] K. Iida, S. Haindl, T. Thersleff, J. Hänisch, F. Kurth, M. Kidszun, R. Hühne, I. Mönch, L. Schultz, B. Holzapfel, and R. Heller. Influence of Fe buffer thickness on the crystalline quality and the transport properties of Fe/Ba( $\text{Fe}_{1-x}\text{Co}_x$ ) $_2\text{As}_2$  bilayers. *Appl. Phys. Lett.*, 97(17):172507, 2010.
- [78] K. Iida, J. Hänisch, T. Thersleff, F. Kurth, M. Kidszun, S. Haindl, R. Hühne, L. Schultz, and B. Holzapfel. Scaling behavior of the critical current in clean epitaxial Ba( $\text{Fe}_{1-x}\text{Co}_x$ ) $_2\text{As}_2$  thin films. *Phys. Rev. B*, 81(10):100507, 2010.
- [79] F. Kurth, K. Iida, S. Trommler, J. Hänisch, K. Nenkov, J. Engelmann, S. Oswald, J. Werner, L. Schultz, B. Holzapfel, and S. Haindl. Electronic phase diagram of disordered Co doped  $\text{BaFe}_2\text{As}_{2-\delta}$ . *Supercond. Sci. Technol.*, 26(2):025014, 2013.
- [80] K. Iida, J. Hänisch, S. Trommler, V. Matias, S. Haindl, F. Kurth, I. Lucas del Pozo, R. Hühne, M. Kidszun, J. Engelmann, L. Schultz, and B. Holzapfel. Epitaxial Growth of Superconducting Ba( $\text{Fe}_{1-x}\text{Co}_x$ ) $_2\text{As}_2$  Thin Films on Technical Ion Beam Assisted Deposition MgO Substrates. *Appl. Phys. Express*, 4(1):013103, 2011.
- [81] J. Engelmann, K. Iida, F. Kurth, C. Behler, S. Oswald, R. Hühne, B. Holzapfel, L. Schultz, and S. Haindl. Fe/Ba( $\text{Fe}_{1-x}\text{Co}_x$ ) $_2\text{As}_2$  multilayers and quasi-multilayers with  $T_c=29$  K. *Physica C*, 494:185–188, 2013.
- [82] S. Lee, C. Tarantini, P. Gao, J. Jiang, J. D. Weiss, F. Kametani, C. M. Folkman, Y. Zhang, X. Q. Pan, E. E. Hellstrom, D. C. Larbalestier, and C. B. Eom. Artificially engineered superlattices of pnictide superconductors. *Nat Mater*, 12(5):392–396, 2013.
- [83] N. H. Lee, S.-G. Jung, D. H. Kim, and W. N. Kang. Potassium-doped  $\text{BaFe}_2\text{As}_2$  superconducting thin films with a transition temperature of 40 K. *Appl. Phys. Lett.*, 96(20):202505, 2010.
- [84] S. Takeda, S. Ueda, T. Yamagishi, S. Agatsuma, S. Takano, A. Mitsuda, and M. Naito. Molecular Beam Epitaxy Growth of Superconducting  $\text{Sr}_{1-x}\text{K}_x\text{Fe}_2\text{As}_2$  and  $\text{Ba}_{1-x}\text{K}_x\text{Fe}_2\text{As}_2$ . *Appl. Phys. Express*, 3(9):093101, 2010.
- [85] S. Adachi, T. Shimode, M. Miura, N. Chikumoto, A. Takemori, K. Nakao, Y. Oshikubo, and K. Tanabe. Pulsed laser deposition of  $\text{BaFe}_2(\text{As,P})_2$  superconducting thin films with high critical current density. *Supercond. Sci. Technol.*, 25(10):105015–105018, 2012.

- [86] A. Sakagami, T. Kawaguchi, M. Tabuchi, T. Ujihara, Y. Takeda, and H. Ikuta. Critical current density and grain boundary property of  $\text{BaFe}_2(\text{As,P})_2$  thin films. *Physica C*, 494(0):181 – 184, 2013.
- [87] M. Miura, S. Adachi, T. Shimode, K. Wada, A. Takemori, N. Chikumoto, K. Nakao, and K. Tanabe. Anisotropy and Superconducting Properties of  $\text{BaFe}_2(\text{As}_{1-x}\text{P}_x)_2$  Films with Various Phosphorus Contents. *Appl. Phys. Express*, 6(9):093101, 2013.
- [88] M. Miura, B. Maiorov, T. Kato, T. Shimode, K. Wada, S. Adachi, and K. Tanabe. Strongly enhanced flux pinning in one-step deposition of  $\text{BaFe}_2(\text{As}_{0.66}\text{P}_{0.33})_2$  superconductor films with uniformly dispersed  $\text{BaZrO}_3$  nanoparticles. *Nat Commun*, 4:2499, 2013.
- [89] H. Sato, H. Hiramatsu, T. Kamiya, and H. Hosono. High critical-current density with less anisotropy in  $\text{BaFe}_2(\text{As,P})_2$  epitaxial thin films: Effect of intentionally grown c-axis vortex-pinning centers. *Appl. Phys. Lett.*, 104(18):182603, 2014.
- [90] J.-F. Ge, Z.-L. Liu, C. Liu, C.-L. Gao, D. Qian, Q.-K. Xue, Y. Liu, and J.-F. Jia. Superconductivity above 100 K in single-layer FeSe films on doped  $\text{SrTiO}_3$ . *Nat Mater*, 14(3):285–289, 2015.
- [91] M. K. Wu, F. C. Hsu, K. W. Yeh, T. W. Huang, J. Y. Luo, M. J. Wang, H. H. Chang, T. K. Chen, S. M. Rao, B. H. Mok, C. L. Chen, Y. L. Huang, C. T. Ke, P. M. Wu, A. M. Chang, C. T. Wu, and T. P. Perng. The development of the superconducting PbO-type  $\beta$ -FeSe and related compounds . *Physica C*, 469(9–12):340 – 349, 2009. Superconductivity in Iron-Pnictides.
- [92] M. J. Wang, J. Y. Luo, T. W. Huang, H. H. Chang, T. K. Chen, F. C. Hsu, C. T. Wu, P. M. Wu, A. M. Chang, and M. K. Wu. Crystal Orientation and Thickness Dependence of the Superconducting Transition Temperature of Tetragonal  $\text{FeSe}_{1-x}$  Thin Films. *Phys. Rev. Lett.*, 103:117002, 2009.
- [93] S.-G. Jung, N. H. Lee, E.-M. Choi, W. N. Kang, S.-I. Lee, T.-J. Hwang, and D. H. Kim. Fabrication of  $\text{FeSe}_{1-x}$  superconducting films with bulk properties . *Physica C*, 470(22):1977 – 1980, 2010.
- [94] I. Tsukada, M. Hanawa, T. Akiike, F. Nabeshima, Y. Imai, A. Ichinose, S. Komiya, T. Hikage, T. Kawaguchi, H. Ikuta, and A. Maeda. Epitaxial Growth of  $\text{FeSe}_{0.5}\text{Te}_{0.5}$  Thin Films on  $\text{CaF}_2$  Substrates with High Critical Current Density. *Appl. Phys. Express*, 4(5):053101, 2011.
- [95] K. Chang, P. Deng, T. Zhang, H.-C. Lin, K. Zhao, S.-H. Ji, L.-L. Wang, K. He, X.-C. Ma, X. Chen, and Q.-K. Xue. Molecular beam epitaxy growth of superconducting LiFeAs film on  $\text{SrTiO}_3$  (001) substrate. *EPL*, 109(2):28003, 2015.
- [96] F. Kurth, E. Reich, J. Hänisch, A. Ichinose, I. Tsukada, R. Hühne, S. Trommler, J. Engelmann, L. Schultz, B. Holzapfel, and K. Iida. Versatile fluoride substrates for Fe-based superconducting thin films. *Appl. Phys. Lett.*, 102(14):142601, 2013.



- [97] J. Brandenburg, V. Neu, H. Wendrock, B. Holzapfel, H.-U. Krebs, and S. Fähler. Pulsed laser deposition of metals: consequences of the energy distribution within the laser spot on film growth. *Appl. Phys. A*, 79(4-6):1005–1007, 2004.
- [98] R. L. Webb, L. C. Jensen, S. C. Langford, and J. T. Dickinson. Interactions of wide band-gap single crystals with 248 nm excimer laser radiation. I. MgO. *J. Appl. Phys.*, 74(4):2323–2337, 1993.
- [99] A. K. Patra. *Crystal Structure, anisotropy and spin reorientation transition of highly coercive, epitaxial Pr-Co films*. PhD thesis, TU Dresden, 2008.
- [100] J. Klein. *Epitaktische Heterostrukturen aus dotierten Manganaten*. PhD thesis, Universität Köln, 2001.
- [101] J. B. Nelson and D. P. Riley. An experimental investigation of extrapolation methods in the derivation of accurate unit-cell dimensions of crystals. *P. Phys. Soc.*, 57(3):160, 1945.
- [102] The National High Magnetic Field Laboratory (NHMFL). *Cross-section of the 45 T.*, 02 2015.
- [103] T. Thersleff. *The Nanoscale Characterization of Functional Superconducting Thin Films*. PhD thesis, TU Dresden, 2011.
- [104] T. Katase, Y. Ishimaru, A. Tsukamoto, H. Hiramatsu, T. Kamiya, K. Tanabe, and H. Hosono. DC superconducting quantum interference devices fabricated using bicrystal grain boundary junctions in Co-doped BaFe<sub>2</sub>As<sub>2</sub> epitaxial films. *Supercond. Sci. Technol.*, 23(8):082001, 2010.
- [105] S. Schmidt, S. Döring, F. Schmidl, V. Tympel, S. Haindl, K. Iida, F. Kurth, B. Holzapfel, and P. Seidel. Bicrystalline Grain Boundary and Hybrid SNS Junctions Based on Ba-122 Thin Films. *IEEE T. Appl. Supercon.*, 23(3):7300104, 2013.
- [106] S. Schmidt, S. Döring, F. Schmidl, V. Grosse, P. Seidel, K. Iida, F. Kurth, S. Haindl, I. Mönch, and B. Holzapfel. BaFe<sub>1.8</sub>Co<sub>0.2</sub>As<sub>2</sub> thin film hybrid Josephson junctions. *Appl. Phys. Lett.*, 97(17):172504, 2010.
- [107] S. Döring, S. Schmidt, F. Schmidl, V. Tympel, S. Haindl, F. Kurth, K. Iida, I. Mönch, B. Holzapfel, and P. Seidel. Edge-type Josephson junctions with Co-doped Ba-122 thin films. *Supercond. Sci. Technol.*, 25(8):084020, 2012.
- [108] H. Hiramatsu, T. Katase, T. Kamiya, M. Hirano, and H. Hosono. Water-induced superconductivity in SrFe<sub>2</sub>As<sub>2</sub>. *Phys. Rev. B*, 80:052501, 2009.
- [109] S. Lee, J. Jiang, J. D. Weiss, C. M. Folkman, C. W. Bark, C. Tarantini, A. Xu, D. Abraimov, A. Polyanskii, C. T. Nelson, Y. Zhang, S. H. Baek, H. W. Jang, A. Yamamoto, F. Kametani, X. Q. Pan, E. E. Hellstrom, A. Gurevich, C. B. Eom, and D. C. Larbalestier. Weak-link behavior of grain boundaries in superconducting Ba(Fe<sub>1-x</sub>Co<sub>x</sub>)<sub>2</sub>As<sub>2</sub> bicrystals. *Appl. Phys. Lett.*, 95(21):212505, 2009.

- [110] S. Trommler, R. Hühne, J. Hänisch, E. Reich, K. Iida, S. Haindl, V. Matias, L. Schultz, and B. Holzapfel. The influence of the buffer layer architecture on transport properties for  $\text{BaFe}_{1.8}\text{Co}_{0.2}\text{As}_2$  films on technical substrates. *Appl. Phys. Lett.*, 100(12):122602, 2012.
- [111] M. Rotter, M. Tegel, D. Johrendt, I. Schellenberg, W. Hermes, and R. Pöttgen. Spin-density-wave anomaly at 140 K in the ternary iron arsenide  $\text{BaFe}_2\text{As}_2$ . *Phys. Rev. B*, 78(2):020503, 2008.
- [112] P. Peccio, D. Daghero, and R. Gonnelli. private communications.
- [113] S. Ueda, S. Takeda, S. Takano, A. Yamamoto, and M. Naito. High- $T_c$  and high- $J_c$   $\text{SmFeAs}(\text{O},\text{F})$  films on fluoride substrates grown by molecular beam epitaxy. *Appl. Phys. Lett.*, 99(23):232505, 2011.
- [114] F. Kurth. Untersuchung des elektronischen Phasendiagramms von Co-dotiertem  $\text{BaFe}_2\text{As}_2$  mittels PLD. Master's thesis, TU Dresden, 2011.
- [115] E. van Heumen, J. Vuorinen, K. Koepernik, F. Masee, Y. Huang, M. Shi, J. Klei, J. Goedkoop, M. Lindroos, J. van den Brink, and M. S. Golden. Existence, Character, and Origin of Surface-Related Bands in the High Temperature Iron Pnictide Superconductor  $\text{BaFe}_{2-x}\text{Co}_x\text{As}_2$ . *Phys. Rev. Lett.*, 106:027002, 2011.
- [116] K. Iida, J. Hänisch, S. Trommler, S. Haindl, F. Kurth, R. Huhne, L. Schultz, and B. Holzapfel. Thickness dependence of structural and transport properties of Co-doped  $\text{BaFe}_2\text{As}_2$  on Fe buffered MgO substrates. *Supercond. Sci. Technol.*, 24(12):125009–125013, 2011.
- [117] S. Takeda, S. Ueda, S. Takano, A. Yamamoto, and M. Naito. Growth of superconducting  $\text{SmFeAs}(\text{O}, \text{F})$  epitaxial films by F diffusion. *Supercond. Sci. Technol.*, 25(3):35007–35012, 2012.
- [118] A. Ichinose, F. Nabeshima, I. Tsukada, M. Hanawa, S. Komiya, T. Akiike, Y. Imai, and A. Maeda. Microscopic analysis of the chemical reaction between  $\text{Fe}(\text{Te},\text{Se})$  thin films and underlying  $\text{CaF}_2$ . *Supercond. Sci. Technol.*, 26(7):075002, 2013.
- [119] D. Daghero, P. Pecchio, F. Laviano, R.S. Gonnelli, F. Kurth, V. Grinenko, and K. Iida. Advanced surface characterization of  $\text{Ba}(\text{Fe}_{0.92}\text{Co}_{0.08})_2\text{As}_2$  epitaxial thin films. *Appl. Surf. Sci.*, 312(0):23–29, 2014.
- [120] C. Tarantini, F. Kametani, S. Lee, J. Jiang, J. D. Weiss, J. Jaroszynski, E. E. Hellstrom, C. B. Eom, and D. C. Larbalestier. Development of very high  $J_c$  in  $\text{Ba}(\text{Fe}_{1-x}\text{Co}_x)_2\text{As}_2$  thin films grown on  $\text{CaF}_2$ . *Sci. Rep.*, 4:7305, 2014.
- [121] S. Döring, M. Monecke, S. Schmidt, F. Schmidl, V. Tympel, J. Engelmann, F. Kurth, K. Iida, S. Haindl, I. Mönch, B. Holzapfel, and P. Seidel. Investigation of  $\text{TiO}_x$  barriers for their use in hybrid Josephson and tunneling junctions based on pnictide thin films. *J. Appl. Phys.*, 115(8):083901, 2014.

- [122] A. Ichinose, I. Tsukada, F. Nabeshima, Y. Imai, A. Maeda, F. Kurth, B. Holzapfel, K. Iida, S. Ueda, and M. Naito. Induced lattice strain in epitaxial Fe-based superconducting films on  $\text{CaF}_2$  substrates: A comparative study of the microstructures of  $\text{SmFeAs}(\text{O},\text{F})$ ,  $\text{Ba}(\text{Fe},\text{Co})_2\text{As}_2$ , and  $\text{FeTe}_{0.5}\text{Se}_{0.5}$ . *Appl. Phys. Lett.*, 104(12):122603, 2014.
- [123] R. Sobota, T. Plecenik, M. Gregor, M. Truchly, L. Satrapinsky, M. Vidis, K. Seicianska, F. Kurth, B. Holzapfel, K. Iida, P. Kus, and A. Plecenika. Surface properties of Co-doped  $\text{BaFe}_2\text{As}_2$  thin films deposited on MgO with Fe buffer layer and  $\text{CaF}_2$  substrates. *Appl. Surf. Sci.*, 312:182–187, 2014.
- [124] P. Pecchio, D. Daghero, G. A. Ummarino, R. S. Gonnelli, F. Kurth, B. Holzapfel, and K. Iida. Doping and critical-temperature dependence of the energy gaps in  $\text{Ba}(\text{Fe}_{1-x}\text{Co}_x)_2\text{As}_2$  thin films. *Phys. Rev. B*, 88(17):174506, 2013.
- [125] K. Tanabe and H. Hosono. Frontiers of Research on Iron-Based Superconductors toward Their Application. *Jpn. J. Appl. Phys.*, 51(1R):010005, 2012.
- [126] J. D. Weiss, C. Tarantini, J. Jiang, F. Kametani, A. A. Polyanskii, D. C. Larbalestier, and E. E. Hellstrom. High intergrain critical current density in fine-grain  $(\text{Ba}_{0.6}\text{K}_{0.4})\text{Fe}_2\text{As}_2$  wires and bulks. *Nat Mater*, 11(8):682–685, 2012.
- [127] Z. Gao, K. Togano, A. Matsumoto, and H. Kumakura. Achievement of practical level critical current densities in  $\text{Ba}_{1-x}\text{K}_x\text{Fe}_2\text{As}_2/\text{Ag}$  tapes by conventional cold mechanical deformation. *Sci. Rep.*, 4:4065, 2014.
- [128] T. Katase, Y. Ishimaru, A. Tsukamoto, H. Hiramatsu, T. Kamiya, K. Tanabe, and H. Hosono. Advantageous grain boundaries in iron pnictide superconductors. *Nat. Commun.*, 2:409, 2011.
- [129] K. Iida, S. Haindl, F. Kurth, J. Hänisch, L. Schultz, and B. Holzapfel.  $\text{BaFe}_2\text{As}_2/\text{Fe}$  Bilayers with [001]-tilt Grain Boundary on MgO and  $\text{SrTiO}_3$  Bicrystal Substrates. *Physics Procedia*, 45(0):189 – 192, 2013.
- [130] T. Kawaguchi, A. Sakagami, Y. Mori, M. Tabuchi, T. Ujihara, Y. Takeda, and H. Ikuta. The strain effect on the superconducting properties of  $\text{BaFe}_2(\text{As},\text{P})_2$  thin films grown by molecular beam epitaxy. *Supercond. Sci. Technol.*, 27(6):065005, 2014.
- [131] T. Shitara and K. Eberl. Electronic properties of InGaP grown by solid-source molecular-beam epitaxy with a GaP decomposition source. *Appl. Phys. Lett.*, 65(3):356–358, 1994.
- [132] W. Jansen and M. Slaughter. Elemental mapping of minerals by electron microprobe. *American Mineralogist*, 67:521–533, 1982.
- [133] K. Ploog. *Molecular beam epitaxy of III-V compounds III-V Semiconductors (Crystals: Growth, Properties and Applications vol 3)*. Berlin: Springer, 1980.

- [134] R. M. Langford. Focused ion beams techniques for nanomaterials characterization. *Microsc. Res. Techniq.*, 69(7):538–549, 2006.
- [135] S. Kasahara, T. Shibauchi, K. Hashimoto, K. Ikada, S. Tonegawa, R. Okazaki, H. Shishido, H. Ikeda, H. Takeya, K. Hirata, T. Terashima, and Y. Matsuda. Evolution from non-Fermi- to Fermi-liquid transport via isovalent doping in  $\text{BaFe}_2(\text{As}_{1-x}\text{P}_x)_2$  superconductors. *Phys. Rev. B*, 81:184519, 2010.
- [136] M. Ishikado, K. Kodama, R. Kajimoto, M. Nakamura, Y. Inamura, S. Wakimoto, A. Iyo, H. Eisaki, M. Arai, and S. Shamoto. Inelastic neutron scattering on iron-based superconductor  $\text{BaFe}_2(\text{As,P})_2$ . *Physica C*, 471(21-22):643–646, 2011.
- [137] C. Putzke, P. Walmsley, J. D. Fletcher, L. Malone, D. Vignolles, C. Proust, S. Badoux, P. See, H. E. Beere, D. A. Ritchie, S. Kasahara, Y. Mizukami, T. Shibauchi, Y. Matsuda, and A. Carrington. Anomalous critical fields in quantum critical superconductors. *Nat Commun*, 5:5679, 2014.
- [138] T. Shibauchi, A. Carrington, and Y. Matsuda. A Quantum Critical Point Lying Beneath the Superconducting Dome in Iron Pnictides. *Annu. Rev. Cond. Matt. Phys.*, 5(1):113–135, 2014.
- [139] J. G. Analytis, H-H. Kuo, R. D. McDonald, M. Wartenbe, P. M. C. Rourke, N. E. Hussey, and I. R. Fisher. Transport near a quantum critical point in  $\text{BaFe}_2(\text{As}_{1-x}\text{P}_x)_2$ . *Nat. Phys.*, 10(3):194–197, 2014.
- [140] J. Hänisch, K. Iida, S. Haindl, F. Kurth, A. Kauffmann, M. Kitzun, T. Thersleff, J. Freudenberger, L. Schultz, and B. Holzapfel.  $J_c$  Scaling and Anisotropies in Co-Doped Ba-122 Thin Films. *IEEE T. Appl. Supercon.*, 21(3):2887–2890, 2011.
- [141] C. Tarantini, A. Gurevich, J. Jaroszynski, F. Balakirev, E. Bellingeri, I. Pallecchi, C. Ferdeghini, B. Shen, H. H. Wen, and D. C. Larbalestier. Significant enhancement of upper critical fields by doping and strain in iron-based superconductors. *Phys. Rev. B*, 84:184522, 2011.
- [142] C. Chaparro, L. Fang, H. Claus, A. Rydh, G. W. Crabtree, V. Stanev, W. K. Kwok, and U. Welp. Doping dependence of the specific heat of single-crystal  $\text{BaFe}_2(\text{As}_{1-x}\text{P}_x)_2$ . *Phys. Rev. B*, 85:184525, 2012.
- [143] N. R. Werthamer, E. Helfand, and P. C. Hohenberg. Temperature and Purity Dependence of the Superconducting Critical Field,  $H_{c2}$ . III. Electron Spin and Spin-Orbit Effects. *Phys. Rev.*, 147:295–302, 1966.
- [144] V. Grinenko, K. Kikoin, S.-L. Drechsler, G. Fuchs, K. Nenkov, S. Wurmehl, F. Hammerath, G. Lang, H.-J. Grafe, B. Holzapfel, J. van den Brink, B. Büchner, and L. Schultz. As vacancies, local moments, and Pauli limiting in  $\text{LaFeAs}_{1-\delta}\text{O}_{0.9}\text{F}_{0.1}$  superconductors. *Phys. Rev. B*, 84(13):134516, 2011.

- [145] G. Fuchs, S.-L. Drechsler, N. Kozlova, M. Bartkowiak, J. E. Hamann-Borrero, G. Behr, K. Nenkov, H.-H. Klauss, H. Maeter, A. Amato, H. Luetkens, A. Kwadrin, R. Khasanov, J. Freudenberger, A. Köhler, M. Knupfer, E. Arushanov, H. Rosner, B. Büchner, and L. Schultz. Orbital and spin effects for the upper critical field in As-deficient disordered Fe pnictide superconductors. *New J. Phys.*, 11(7):075007, 2009.
- [146] H. Q. Yuan, J. Singleton, F. F. Balakirev, S. A. Baily, G. F. Chen, J. L. Luo, and N. L. Wang. Nearly isotropic superconductivity in (Ba,K)Fe<sub>2</sub>As<sub>2</sub>. *Nature*, 457(7229):565–568, 2009.
- [147] K. Iida, J. Hänisch, C. Tarantini, F. Kurth, J. Jaroszynski, S. Ueda, M. Naito, A. Ichinose, I. Tsukada, E. Reich, V. Grinenko, L. Schultz, and B. Holzapfel. Oxypnictide SmFeAs(O,F) superconductor: a candidate for high-field magnet applications. *Sci. Rep.*, 3:2139, 2013.
- [148] D. L. Sun, Y. Liu, and C. T. Lin. Comparative study of upper critical field  $H_{c2}$  and second magnetization peak  $H_{sp}$  in hole- and electron-doped BaFe<sub>2</sub>As<sub>2</sub> superconductor. *Phys. Rev. B*, 80:144515, 2009.
- [149] K. Hashimoto, M. Yamashita, S. Kasahara, Y. Senshu, N. Nakata, S. Tonegawa, K. Ikada, A. Serafin, A. Carrington, T. Terashima, H. Ikeda, T. Shibauchi, and Y. Matsuda. Line nodes in the energy gap of superconducting BaFe<sub>2</sub>(As<sub>1-x</sub>P<sub>x</sub>)<sub>2</sub> single crystals as seen via penetration depth and thermal conductivity. *Phys. Rev. B*, 81:220501, 2010.
- [150] B. Shabbir, X. L. Wang, S. R. Ghorbani, S. X. Dou, and F. Xiang. Hydrostatic pressure induced transition from  $\delta T_c$  to  $\delta l$  pinning mechanism in MgB<sub>2</sub>. *Supercond. Sci. Technol.*, 28(5):055001, 2015.
- [151] G. Ercolano, M. Bianchetti, S. C. Wimbush, S. A. Harrington, H. Wang, J. H. Lee, and J. L. MacManus-Driscoll. State-of-the-art flux pinning in YBa<sub>2</sub>Cu<sub>3</sub>O<sub>7- $\delta$</sub>  by the creation of highly linear, segmented nanorods of Ba<sub>2</sub>(Y/Gd)(Nb/Ta)O<sub>6</sub> together with nanoparticles of (Y/Gd)<sub>2</sub>O<sub>3</sub> and (Y/Gd)Ba<sub>2</sub>Cu<sub>4</sub>O<sub>8</sub>. *Supercond. Sci. Technol.*, 24(9):095012, 2011.
- [152] H. Matsui, H. Ogiso, H. Yamasaki, M. Sohma, I. Yamaguchi, T. Kumagai, and T. Manabe. Dimpling in critical current density vs. magnetic field angle in YBa<sub>2</sub>Cu<sub>3</sub>O<sub>7</sub> films irradiated with 3-MeV gold ions. *J. Appl. Phys.*, 114(23):233911, 2013.
- [153] S. Awaji, M. Namba, K. Watanabe, M. Miura, Y. Ichino, Y. Yoshida, Y. Takai, and K. Matsumoto.  $J_c$  and  $Bi$  properties of Sm<sub>1+x</sub>Ba<sub>2-x</sub>Cu<sub>3</sub>O<sub>y</sub> films with nano-particles. *Physica C*, 463-465(0):669–673, October 2007.
- [154] K. Hashimoto, K. Cho, T. Shibauchi, S. Kasahara, Y. Mizukami, R. Katsumata, Y. Tsuruhara, T. Terashima, H. Ikeda, M. A. Tanatar, H. Kitano, N. Salovich, R. W. Giannetta, P. Walmsley, A. Carrington, R. Prozorov, and Y. Matsuda. A

- Sharp Peak of the Zero-Temperature Penetration Depth at Optimal Composition in  $\text{BaFe}_2(\text{As}_{1-x}\text{P}_x)_2$ . *Science*, 336(6088):1554–1557, 2012.
- [155] C. J. van der Beek, M. Konczykowski, and R. Prozorov. Anisotropy of strong pinning in multi-band superconductors. *Supercond. Sci. Technol.*, 25(8):084010, 2012.
- [156] R. Griessen, Wen Hai-hu, A. J. J. van Dalen, B. Dam, J. Rector, H. G. Schnack, S. Libbrecht, E. Osquiguil, and Y. Bruynseraede. Evidence for mean free path fluctuation induced pinning in  $\text{YBa}_2\text{Cu}_3\text{O}_7$  and  $\text{YBa}_2\text{Cu}_4\text{O}_8$  films. *Phys. Rev. Lett.*, 72:1910–1913, 1994.
- [157] H.-S. Lee, M. Bartkowiak, J.-H. Park, J.-Y. Lee, J.-Y. Kim, N.-H. Sung, B. K. Cho, C.-U. Jung, J. S. Kim, and H.-J. Lee. Effects of two gaps and paramagnetic pair breaking on the upper critical field of  $\text{SmFeAsO}_{0.85}$  and  $\text{SmFeAsO}_{0.8}\text{F}_{0.2}$  single crystals. *Phys. Rev. B*, 80:144512, 2009.
- [158] Z. Gao, L. Wang, Y. Qi, D. Wang, X. Zhang, Y. Ma, H. Yang, and H. Wen. Superconducting properties of granular  $\text{SmFeAsO}_{1-x}\text{F}_x$  wires with  $T_c = 52$  K prepared by the powder-in-tube method. *Supercond. Sci. Technol.*, 21(11):112001, 2008.
- [159] C. Tarantini, S. Lee, F. Kametani, J. Jiang, J. D. Weiss, J. Jaroszynski, C. M. Folkman, E. E. Hellstrom, C. B. Eom, and D. C. Larbalestier. Artificial and self-assembled vortex-pinning centers in superconducting  $\text{Ba}(\text{Fe}_{1-x}\text{Co}_x)_2\text{As}_2$  thin films as a route to obtaining very high critical-current densities. *Phys. Rev. B*, 86:214504, 2012.
- [160] B. Maiorov, T. Katase, I. O. Usov, M. Weigand, L. Civale, H. Hiramatsu, and H. Hosono. Competition and cooperation of pinning by extrinsic point-like defects and intrinsic strong columnar defects in  $\text{BaFe}_2\text{As}_2$  thin films. *Phys. Rev. B*, 86:094513, 2012.
- [161] T. Katase, H. Hiramatsu, V. Matias, C. Sheehan, Y. Ishimaru, T. Kamiya, K. Tanabe, and H. Hosono. Biaxially textured cobalt-doped  $\text{BaFe}_2\text{As}_2$  films with high critical current density over  $1\text{ MA/cm}^2$  on MgO-buffered metal-tape flexible substrates. *Appl. Phys. Lett.*, 98(24):242510, 2011.
- [162] W. Si, J. Zhou, Q. Jie, I. Dimitrov, V. Solovyov, P. D. Johnson, J. Jaroszynski, V. Matias, C. Sheehan, and Q. Li. Iron-chalcogenide  $\text{FeSe}_{0.5}\text{Te}_{0.5}$  coated superconducting tapes for high field applications. *Appl. Phys. Lett.*, 98(26):262509, 2011.
- [163] W. Si, S. J. Han, X. Shi, S. N. Ehrlich, J. Jaroszynski, A. Goyal, and Q. Li. High current superconductivity in  $\text{FeSe}_{0.5}\text{Te}_{0.5}$ -coated conductors at 30 tesla. *Nat Commun*, 4:1347, 2013.
- [164] Z. Gao, Y. Ma, C. Yao, X. Zhang, C. Wang, D. Wang, S. Awaji, and K. Watanabe. High critical current density and low anisotropy in textured  $\text{Sr}_{1-x}\text{K}_x\text{Fe}_2\text{As}_2$  tapes for high field applications. *Sci. Rep.*, 2:998, 2012.

- [165] T. T. M. Palstra, B. Batlogg, L. F. Schneemeyer, and J. V. Waszczak. Thermally Activated Dissipation in  $\text{Bi}_{2.2}\text{Sr}_2\text{Ca}_{0.8}\text{Cu}_2\text{O}_{8+\delta}$ . *Phys. Rev. Lett.*, 61:1662–1665, 1988.
- [166] Y. Yeshurun and A. P. Malozemoff. Giant Flux Creep and Irreversibility in an Y-Ba-Cu-O Crystal: An Alternative to the Superconducting-Glass Model. *Phys. Rev. Lett.*, 60:2202–2205, 1988.
- [167] A. I. Larkin and Yu. N. Ovchinnikov. Pinning in type II superconductors. *Journal of Low Temperature Physics*, 34(3-4):409–428, 1979.
- [168] H. Yamasaki and Y. Mawatari. Current-voltage characteristics and flux creep in melt-textured  $\text{YBa}_2\text{Cu}_3\text{O}_{7-\delta}$ . *Supercond. Sci. Technol.*, 13(2):202, 2000.
- [169] L. Civale, B. Maiorov, J.L. MacManus-Driscoll, H. Wang, T.G. Holesinger, S.R. Foltyn, A. Serquis, and P.N. Arendt. Identification of intrinsic ab-plane pinning in  $\text{YBa}_2\text{Cu}_3\text{O}_7$  thin films and coated conductors. *IEEE T. Appl. Supercon.*, 15(2):2808–2811, 2005.
- [170] S. Awaji, M. Namba, K. Watanabe, M. Miura, M. Yoshizumi, T. Izumi, and Y. Shiohara. Flux pinning properties of TFA-MOD (Y,Gd) $\text{Ba}_2\text{Cu}_3\text{O}_x$  tapes with  $\text{BaZrO}_3$  nanoparticles. *Supercond. Sci. Technol.*, 23(1):014006, 2010.
- [171] S. Awaji, R. Ishihara, K. Watanabe, K. Shikimachi, N. Hirano, and S. Nagaya. Anisotropy of the Critical Current Density and Intrinsic Pinning Behaviors of  $\text{YBa}_2\text{Cu}_3\text{O}_y$  Coated Conductors. *Appl. Phys. Express*, 4(1):013101, 2011.
- [172] K. Iida, J. Hänisch, E. Reich, F. Kurth, R. Hühne, L. Schultz, B. Holzapfel, A. Ichinose, M. Hanawa, I. Tsukada, M. Schulze, S. Aswartham, S. Wurmehl, and B. Büchner. Intrinsic pinning and the critical current scaling of clean epitaxial Fe(Se,Te) thin films. *Phys. Rev. B*, 87:104510, 2013.
- [173] P. J. W. Moll, L. Balicas, V. Geshkenbein, G. Blatter, J. Karpinski, N. D. Zhigadlo, and B. Batlogg. Transition from slow Abrikosov to fast moving Josephson vortices in iron pnictide superconductors. *Nat Mater*, 12(2):134–138, 2013.
- [174] M. Tachiki and S. Takahashi. Anisotropy of critical current in layered oxide superconductors. *Solid State Commun.*, 72(11):1083 – 1086, 1989.
- [175] P. Schmitt, P. Kummeth, L. Schultz, and G. Saemann-Ischenko. Two-dimensional behavior and critical-current anisotropy in epitaxial  $\text{Bi}_2\text{Sr}_2\text{CaCu}_2\text{O}_{8+x}$  thin films. *Phys. Rev. Lett.*, 67:267–270, 1991.
- [176] A. Dubroka, K. W. Kim, M. Rössle, V. K. Malik, A. J. Drew, R. H. Liu, G. Wu, X. H. Chen, and C. Bernhard. Superconducting Energy Gap and  $c$ -Axis Plasma Frequency of (Nd,Sm)FeAsO<sub>0.82</sub>F<sub>0.18</sub> Superconductors from Infrared Ellipsometry. *Phys. Rev. Lett.*, 101:097011, 2008.

- [177] U. Welp, C. Chaparro, A. E. Koshelev, W. K. Kwok, A. Rydh, N. D. Zhigadlo, J. Karpinski, and S. Weyeneth. Anisotropic phase diagram and superconducting fluctuations of single-crystalline  $\text{SmFeAsO}_{0.85}\text{F}_{0.15}$ . *Phys. Rev. B*, 83:100513, 2011.
- [178] L. Ozyuzer, A. E. Koshelev, C. Kurter, N. Gopalsami, Q. Li, M. Tachiki, K. Kadowaki, T. Yamamoto, H. Minami, H. Yamaguchi, T. Tachiki, K. E. Gray, W.-K. Kwok, and U. Welp. Emission of Coherent THz Radiation from Superconductors. *Science*, 318(5854):1291–1293, 2007.
- [179] Y. Kubo, Y. Takahide, S. Ueda, Y. Takano, and Y. Ootuka. Macroscopic Quantum Tunneling in a  $\text{Bi}_2\text{Sr}_2\text{CaCu}_2\text{O}_{8+\delta}$  Single Crystalline Whisker. *Appl. Phys. Express*, 3(6):063104, 2010.
- [180] J. Lisenfeld, A. Lukashenko, M. Ansmann, J. M. Martinis, and A. V. Ustinov. Temperature Dependence of Coherent Oscillations in Josephson Phase Qubits. *Phys. Rev. Lett.*, 99:170504, 2007.
- [181] H. Kashiwaya, K. Shirai, T. Matsumoto, H. Shibata, H. Kambara, M. Ishikado, H. Eisaki, A. Iyo, S. Shamoto, I. Kurosawa, and S. Kashiwaya. C-axis critical current of a  $\text{PrFeAsO}_{0.7}$  single crystal. *Appl. Phys. Lett.*, 96(20):202504, 2010.
- [182] L. Fang, Y. Jia, V. Mishra, C. Chaparro, V. K. Vlasko-Vlasov, A. E. Koshelev, U. Welp, G. W. Crabtree, S. Zhu, N. D. Zhigadlo, S. Katrych, J. Karpinski, and W. K. Kwok. Huge critical current density and tailored superconducting anisotropy in  $\text{SmFeAsO}_{0.8}\text{F}_{0.15}$  by low-density columnar-defect incorporation. *Nat. Commun.*, 4:2655, 2013.
- [183] A. Xu, J. J. Jaroszynski, F. Kametani, Z. Chen, D. C. Larbalestier, Y. L. Viouchkov, Y. Chen, Y. Xie, and V. Selvamanickam. Angular dependence of  $J_c$  for YBCO coated conductors at low temperature and very high magnetic fields. *Supercond. Sci. Technol.*, 23(1):014003, 2010.
- [184] Y. Ma, L. Wang, Y. Qi, Z. Gao, D. Wang, and X. Zhang. Development of Powder-in-Tube Processed Iron Pnictide Wires and Tapes. *IEEE T. Appl. Supercon.*, 21(3):2878–2881, 2011.
- [185] M. Fujioka, T. Kota, M. Matoba, T. Ozaki, Y. Takano, H. Kumakura, and Y. Kamihara. Effective Ex-situ Fabrication of F-Doped  $\text{SmFeAsO}$  Wire for High Transport Critical Current Density. *Appl. Phys. Express*, 4(6):063102, 2011.
- [186] Z.-A. Ren, J. Yang, W. Lu, W. Yi, X.-L. Shen, Z.-C. Li, G.-C. Che, X.-L. Dong, L.-L. Sun, F. Zhou, and Z.-X. Zhao. Superconductivity in the iron-based F-doped layered quaternary compound  $\text{Nd}[\text{O}_{1-x}\text{F}_x]\text{FeAs}$ . *EPL*, 82(5):57002, 2008.
- [187] J. Jaroszynski, S. C. Riggs, F. Hunte, A. Gurevich, D. C. Larbalestier, G. S. Boebinger, F. F. Balakirev, A. Migliori, Z. A. Ren, W. Lu, J. Yang, X. L. Shen, X. L. Dong, Z. X. Zhao, R. Jin, A. S. Sefat, M. A. McGuire, B. C. Sales, D. K.



- Christen, and D. Mandrus. Comparative high-field magnetotransport of the oxypnictide superconductors  $R\text{FeAsO}_{1-x}\text{F}_x$  ( $R=\text{La}, \text{Nd}$ ) and  $\text{SmFeAsO}_{1-\delta}$ . *Phys. Rev. B*, 78:064511, 2008.
- [188] J. Jaroszynski, F. Hunte, L. Balicas, Y.-J. Jo, I. Raičević, A. Gurevich, D. C. Larbalestier, F. F. Balakirev, L. Fang, P. Cheng, Y. Jia, and H. H. Wen. Upper critical fields and thermally-activated transport of  $\text{NdFeAsO}_{0.7}\text{F}_{0.3}$  single crystal. *Phys. Rev. B*, 78:174523, 2008.
- [189] T. Yildirim. Origin of the 150 K Anomaly in  $\text{LaFeAsO}$ : Competing Antiferromagnetic Interactions, Frustration, and a Structural Phase Transition. *Phys. Rev. Lett.*, 101:057010, 2008.
- [190] C. Tarantini, A. Gurevich, D. C. Larbalestier, Z.-A. Ren, X.-L. Dong, W. Lu, and Z.-X. Zhao. Superconductivity and antiferromagnetic ordering in the high-field paramagnetic oxypnictide  $\text{NdFeAsO}_{0.94}\text{F}_{0.06}$ . *Phys. Rev. B*, 78:184501, 2008.
- [191] T. Kawaguchi, H. Uemura, T. Ohno, M. Tabuchi, T. Ujihara, K. Takenaka, Y. Takeda, and H. Ikuta. In situ growth of superconducting  $\text{NdFeAs}(\text{O},\text{F})$  thin films by molecular beam epitaxy. *Appl. Phys. Lett.*, 97(4):042509, 2010.
- [192] T. Kawaguchi, H. Uemura, T. Ohno, M. Tabuchi, T. Ujihara, Y. Takeda, and H. Ikuta. Molecular Beam Epitaxy Growth of Superconducting  $\text{NdFeAs}(\text{O},\text{F})$  Thin Films Using a F-Getter and a Novel F-Doping Method. *Appl. Phys. Express*, 4(8):083102, 2011.
- [193] A. Gurevich. Limits of the upper critical field in dirty two-gap superconductors. *Physica C*, 456(1–2):160 – 169, 2007.
- [194] Z. P. Yin, K. Haule, and G. Kotliar. Kinetic frustration and the nature of the magnetic and paramagnetic states in iron pnictides and iron chalcogenides. *Nat Mater*, 10(12):932–935, 2011.
- [195] F. Kurth, C. Tarantini, V. Grinenko, J. Hänisch, J. Jaroszynski, E. Reich, Y. Mori, A. Sakagami, T. Kawaguchi, J. Engelmann, L. Schultz, B. Holzapfel, H. Ikuta, R. Hühne, and K. Iida. Unusually high critical current of clean P-doped  $\text{BaFe}_2\text{As}_2$  single crystalline thin film. *Appl. Phys. Lett.*, 106(7):072602, 2015.
- [196] M. Kitzun, S. Haindl, T. Thersleff, J. Hänisch, A. Kauffmann, K. Iida, J. Freudenberger, L. Schultz, and B. Holzapfel. Critical Current Scaling and Anisotropy in Oxypnictide Superconductors. *Phys. Rev. Lett.*, 106:137001, 2011.



# List of publications

- [1] Yu A. Aleshchenko, A. V. Muratov, V. M. Pudalov, E. S. Zhukova, B. P. Gorshunov, **F. Kurth**, and K. Iida. Observation of Multiple Superconducting Gaps in the Infrared Reflectivity Spectra of  $\text{Ba}(\text{Fe}_{0.9}\text{Co}_{0.1})_2\text{As}_2$ . *Jetp Letters*, 94(9):719–722, 2012.
- [2] C. Barone, S. Pagano, E. Bellingeri, C. Ferdeghini, M. Adamo, E. Sarnelli, **F. Kurth**, B. Holzapfel, and K. Iida. Temperature-dependent electric noise level in different iron-based superconductors. *Journal of Physics: Conference Series*, 507(1):012002, 2014.
- [3] C. Barone, F. Romeo, S. Pagano, M. Adamo, C. Nappi, E. Sarnelli, **F. Kurth**, and K. Iida. Probing transport mechanisms of  $\text{BaFe}_2\text{As}_2$  superconducting films and grain boundary junctions by noise spectroscopy. *Sci. Rep.*, 4, 2014.
- [4] I.S. Blokhin, S.Yu. Gavrilkin, B.P. Gorshunov, V.A. Dravin, E.S. Zhukova, O.M. Ivanenko, K. Iida, S.I. Krasnosvobodtsev, **F. Kurth**, K.V. Mitsen, and A.Yu. Tsvetkov. Effect of radiation defects on the magnetotransport properties of  $\text{Ba}(\text{Fe}_{1-x}\text{Co}_x\text{As})_2$  high-temperature superconductor. *JETP Letters*, 101(4):247–250, 2015.
- [5] C. Bonavolontà, L. Parlato, C. de Lisio, M. Valentino, G. P. Pepe, I. Kazumasa, **F. Kurth**, E. Bellingeri, I. Pallecchi, M. Putti, C. Ferdeghini, G. A. Ummarino, and F. Laviano. Femtosecond spectroscopy in a nearly optimally doped Fe-based superconductors  $\text{FeSe}_{0.5}\text{Te}_{0.5}$  and  $\text{Ba}(\text{Fe}_{1-x}\text{Co}_x)_2\text{As}_2/\text{Fe}$  thin film. *Journal of Physics: Conference Series*, 507(1):012004, 2014.
- [6] C. Bonavolonta, C. de Lisio, M. Valentino, L. Parlato, G. P. Pepe, **F. Kurth**, and K. Iida. Evaluation of superconducting gaps in optimally doped  $\text{Ba}(\text{Fe}_{1-x}\text{Co}_x)_2\text{As}_2/\text{Fe}$  bilayers by ultrafast time-resolved spectroscopy. *Physica C*, 503:132–135, 2014.
- [7] D. Daghero, P. Pecchio, F. Laviano, R. S. Gonnelli, **F. Kurth**, V. Grinenko, and

- K. Iida. Advanced surface characterization of  $\text{Ba}(\text{Fe}_{0.92}\text{Co}_{0.08})_2\text{As}_2$  epitaxial thin films. *Appl. Surf. Sci.*, 312:23–29, 2014.
- [8] S. Döring, M. Monecke, S. Schmidt, F. Schmidl, V. Tympel, J. Engelmann, **F. Kurth**, K. Iida, S. Haindl, I. Mönch, B. Holzapfel, and P. Seidel. Investigation of  $\text{TiO}_x$  barriers for their use in hybrid Josephson and tunneling junctions based on pnictide thin films. *J. Appl. Phys.*, 115(8), 2014.
- [9] S. Döring, S. Schmidt, F. Schmidl, V. Tympel, S. Haindl, **F. Kurth**, K. Iida, I. Mönch, B. Holzapfel, and P. Seidel. Edge-type Josephson junctions with Co-doped Ba-122 thin films. *Supercond. Sci. Technol.*, 25(8), 2012.
- [10] S. Döring, S. Schmidt, F. Schmidl, V. Tympel, S. Haindl, **F. Kurth**, K. Iida, I. Mönch, B. Holzapfel, and P. Seidel. Planar hybrid superconductor-normal metal-superconductor thin film junctions based on  $\text{BaFe}_{1.8}\text{Co}_{0.2}\text{As}_2$ . *Physica C*, 478:15–18, 2012.
- [11] S. Döring, S. Schmidt, S. Gottwals, F. Schmidl, V. Tympel, I. Mönch, **F. Kurth**, K. Iida, B. Holzapfel, and P. Seidel. Influence of the spreading resistance on the conductance spectrum of planar hybrid thin film SNS' junctions based on iron pnictides. *Journal of Physics: Conference Series*, 507(1):012008, 2014.
- [12] S. Döring, S. Schmidt, F. Schmidl, V. Tympel, S. Haindl, **F. Kurth**, K. Iida, I. Mönch, B. Holzapfel, and P. Seidel. ISS2011 Development of iron-based superconducting devices. *Physics Procedia*, 27:296–299, 2011.
- [13] S. Döring, S. Schmidt, D. Reifert, M. Feltz, M. Monecke, N. Hasan, V. Tympel, F. Schmidl, J. Engelmann, **F. Kurth**, K. Iida, I. Mönch, B. Holzapfel, and P. Seidel. Hybrid Josephson Junctions with Iron-based and Conventional Superconductor Electrodes. *Journal of Superconductivity and Novel Magnetism*, pages 1–5, 2014.
- [14] J. Engelmann, V. Grinenko, P. Chekhonin, W. Skrotzki, D. V. Efremov, S. Oswald, K. Iida, R. Hühne, J. Hänisch, M. Hoffmann, **F. Kurth**, L. Schultz, and B. Holzapfel. Strain induced superconductivity in the parent compound  $\text{BaFe}_2\text{As}_2$ . *Nat Commun*, 4, 2013.
- [15] J. Engelmann, K. Iida, **F. Kurth**, C. Behler, S. Oswald, R. Hühne, B. Holzapfel, L. Schultz, and S. Haindl.  $\text{Fe}/\text{Ba}(\text{Fe}_{1-x}\text{Co}_x)_2\text{As}_2$  multilayers and quasi-multilayers with  $T_c=29\text{ K}$ . *Physica C*, 494:185–188, 2013.

- [16] T. Fischer, A. V. Pronin, J. Wosnitzer, K. Iida, **F. Kurth**, S. Haindl, L. Schultz, B. Holzapfel, and E. Schachinger. Highly anisotropic energy gap in superconducting  $\text{Ba}(\text{Fe}_{0.9}\text{Co}_{0.1})_2\text{As}_2$  from optical conductivity measurements. *Phys. Rev. B*, 82(22), 2010.
- [17] B. Gorshunov, D. Wu, A. A. Voronkov, P. Kallina, K. Iida, S. Haindl, **F. Kurth**, L. Schultz, B. Holzapfel, and M. Dressel. Direct observation of the superconducting energy gap in the optical conductivity of the iron pnictide superconductor  $\text{Ba}(\text{Fe}_{0.9}\text{Co}_{0.1})_2\text{As}_2$ . *Phys. Rev. B*, 81(6), 2010.
- [18] J. Hänisch, K. Iida, S. Haindl, **F. Kurth**, A. Kauffmann, M. Kidszun, T. Thersleff, J. Freudenberger, L. Schultz, and B. Holzapfel.  $J_c$  Scaling and Anisotropies in Co-Doped Ba-122 Thin Films. *IEEE Trans. Appl. Supercond.*, 21(3):2887–2890, 2011.
- [19] J. Hänisch, K. Iida, **F. Kurth**, T. Thersleff, S. Trommler, E. Reich, R. Hühne, L. Schultz, and B. Holzapfel. The effect of 45 deg grain boundaries and associated Fe particles on  $J_c$  and resistivity in  $\text{Ba}(\text{Fe}_{0.9}\text{Co}_{0.1})_2\text{As}_2$  thin films. *American Institute of Physics Conference Series*, 1574, 2014.
- [20] A. Ichinose, I. Tsukada, F. Nabeshima, Y. Imai, A. Maeda, **F. Kurth**, B. Holzapfel, K. Iida, S. Ueda, and M. Naito. Induced lattice strain in epitaxial Fe-based superconducting films on  $\text{CaF}_2$  substrates: A comparative study of the microstructures of  $\text{SmFeAs}(\text{O},\text{F})$ ,  $\text{Ba}(\text{Fe},\text{Co})_2\text{As}_2$ , and  $\text{FeTe}_{0.5}\text{Se}_{0.5}$ . *Appl. Phys. Lett.*, 104(12), 2014.
- [21] K. Iida, J. Hänisch, R. Hühne, **F. Kurth**, M. Kidszun, S. Haindl, J. Werner, L. Schultz, and B. Holzapfel. Strong  $T_c$  dependence for strained epitaxial  $\text{Ba}(\text{Fe}_{1-x}\text{Co}_x)_2\text{As}_2$  thin films. *Appl. Phys. Lett.*, 95(19), 2009.
- [22] K. Iida, J. Hänisch, T. Thersleff, **F. Kurth**, M. Kidszun, S. Haindl, R. Hühne, L. Schultz, and B. Holzapfel. Scaling behavior of the critical current in clean epitaxial  $\text{Ba}(\text{Fe}_{1-x}\text{Co}_x)_2\text{As}_2$  thin films. *Phys. Rev. B*, 81(10), 2010.
- [23] K. Iida, S. Haindl, **F. Kurth**, J. Hänisch, L. Schulz, and B. Holzapfel.  $\text{BaFe}_2\text{As}_2/\text{Fe}$  Bilayers with [001]-tilt Grain Boundary on  $\text{MgO}$  and  $\text{SrTiO}_3$  Bicrystal Substrates. *Physics Procedia*, 45:189–192, 2013.
- [24] K. Iida, S. Haindl, T. Thersleff, J. Hänisch, **F. Kurth**, M. Kidszun, R. Hühne, I. Mönch, L. Schultz, B. Holzapfel, and R. Heller. Influence of Fe buffer thickness on the crystalline quality and the transport properties of  $\text{Fe}/\text{Ba}(\text{Fe}_{1-x}\text{Co}_x)_2\text{As}_2$  bilayers. *Appl. Phys. Lett.*, 97(17), 2010.

- [25] K. Iida, J. Hänisch, E. Reich, **F. Kurth**, R. Hühne, L. Schultz, B. Holzapfel, A. Ichinose, M. Hanawa, I. Tsukada, M. Schulze, S. Aswartham, S. Wurmehl, and B. Büchner. Intrinsic pinning and the critical current scaling of clean epitaxial Fe(Se, Te) thin films. *Phys. Rev. B*, 87(10), 2013.
- [26] K. Iida, J. Hänisch, C. Tarantini, **F. Kurth**, J. Jaroszynski, S. Ueda, M. Naito, A. Ichinose, I. Tsukada, E. Reich, V. Grinenko, L. Schultz, and B. Holzapfel. Oxypnictide SmFeAs(O,F) superconductor: a candidate for high-field magnet applications. *Sci. Rep.*, 3, 2013.
- [27] K. Iida, J. Hänisch, S. Trommler, V. Matias, S. Haindl, **F. Kurth**, I. L. del Pozo, R. Hühne, M. Kidszun, J. Engelmann, L. Schultz, and B. Holzapfel. Epitaxial Growth of Superconducting Ba(Fe<sub>1-x</sub>Co<sub>x</sub>)<sub>2</sub>As<sub>2</sub> Thin Films on Technical Ion Beam Assisted Deposition MgO Substrates. *Appl. Phys. Express*, 4(1), 2011.
- [28] K. Iida, J. Hänisch, S. Trommler, S. Haindl, **F. Kurth**, R. Hühne, L. Schultz, and B. Holzapfel. Thickness dependence of structural and transport properties of Co-doped BaFe<sub>2</sub>As<sub>2</sub> on Fe buffered MgO substrates. *Supercond. Sci. Technol.*, 24(12):125009–125013, 2011.
- [29] K. Iida, **F. Kurth**, M. Chihara, N. Sumiya, V. Grinenko, A. Ichinose, I. Tsukada, J. Hänisch, V. Matias, T. Hatano, B. Holzapfel, and H. Ikuta. Highly textured oxypnictide superconducting thin films on metal substrates. *Appl. Phys. Lett.*, 105(17), 2014.
- [30] **F. Kurth**, K. Iida, S. Trommler, J. Hänisch, K. Nenkov, J. Engelmann, S. Oswald, J. Werner, L. Schultz, B. Holzapfel, and S. Haindl. Electronic phase diagram of disordered Co doped BaFe<sub>2</sub>As<sub>2-δ</sub>. *Supercond. Sci. Technol.*, 26(2), 2013.
- [31] **F. Kurth**, E. Reich, J. Hänisch, A. Ichinose, I. Tsukada, R. Hühne, S. Trommler, J. Engelmann, L. Schultz, B. Holzapfel, and K. Iida. Versatile fluoride substrates for Fe-based superconducting thin films. *Appl. Phys. Lett.*, 102(14), 2013.
- [32] **F. Kurth**, C. Tarantini, V. Grinenko, J. Hänisch, J. Jaroszynski, E. Reich, Y. Mori, A. Sakagami, T. Kawaguchi, J. Engelmann, L. Schultz, B. Holzapfel, H. Ikuta, R. Hühne, and K. Iida. Unusually high critical current of clean P-doped BaFe<sub>2</sub>As<sub>2</sub> single crystalline thin film. *Appl. Phys. Lett.*, 106(7):–, 2015.
- [33] E. G. Maksimov, A. E. Karakozov, A. A. Voronkov, B. P. Gorshunov, S. S. Zhukov, E. S. Zhukova, V. S. Nozdrin, S. Haindl, B. Holzapfel, L. Schultz, D. Wu, M. Dressel,

- K. Iida, P. Kallina, and **F. Kurth**. Two-Band BCS Mechanism of Superconductivity in a  $\text{Ba}(\text{Fe}_{0.9}\text{Co}_{0.1})_2\text{As}_2$  High-Temperature Superconductor. *Jetp Letters*, 93(12):736–742, 2011.
- [34] V. Mishev, W. Seeböck, M. Eisterer, K. Iida, **F. Kurth**, J. Hänisch, E. Reich, and B. Holzapfel. One-dimensional pinning behavior in Co-doped  $\text{BaFe}_2\text{As}_2$  thin films. *Appl. Phys. Lett.*, 103(23), 2013.
- [35] P. Pecchio, D. Daghero, G. A. Ummarino, R. S. Gonnelli, **F. Kurth**, B. Holzapfel, and K. Iida. Doping and critical-temperature dependence of the energy gaps in  $\text{Ba}(\text{Fe}_{1-x}\text{Co}_x)_2\text{As}_2$  thin films. *Phys. Rev. B*, 88(17), 2013.
- [36] T. Plecenik, M. Gregor, R. Sobota, M. Truchly, L. Satrapinsky, **F. Kurth**, B. Holzapfel, K. Iida, P. Kus, and A. Plecenik. Surface transport properties of Fe-based superconductors: The influence of degradation and inhomogeneity. *Appl. Phys. Lett.*, 103(5), 2013.
- [37] D. Rall, K. Il'in, K. Iida, S. Haindl, **F. Kurth**, T. Thersleff, L. Schultz, B. Holzapfel, and M. Siegel. Critical current densities in ultrathin  $\text{Ba}(\text{Fe},\text{Co})_2\text{As}_2$  microbridges. *Phys. Rev. B*, 83(13), 2011.
- [38] D. Rall, L. Rehm, K. Il'in, M. Siegel, K. Iida, S. Haindl, **F. Kurth**, B. Holzapfel, L. Schultz, J. Yong, and T. Lemberger. Penetration and de-pinning of vortices in sub-micrometer  $\text{Ba}(\text{Fe},\text{Co})_2\text{As}_2$  thin film bridges. *Physica C*, 479:164–166, 2012.
- [39] L. Rehm, D. Henrich, M. Hofherr, S. Wünsch, P. Thoma, A. Scheuring, K. Il'in, M. Siegel, S. Haindl, K. Iida, **F. Kurth**, B. Holzapfel, and L. Schultz. Infrared Photo-Response of Fe-Shunted Ba-122 Thin Film Microstructures. *IEEE Trans. Appl. Supercond.*, 23(3), 2013.
- [40] S. Schmidt, S. Döring, F. Schmidl, V. Grosse, P. Seidel, K. Iida, **F. Kurth**, S. Haindl, I. Mönch, and B. Holzapfel.  $\text{BaFe}_{1.8}\text{Co}_{0.2}\text{As}_2$  thin film hybrid Josephson junctions. *Appl. Phys. Lett.*, 97(17), 2010.
- [41] S. Schmidt, S. Döring, F. Schmidl, V. Tympel, S. Haindl, K. Iida, **F. Kurth**, B. Holzapfel, and P. Seidel. Bicrystalline Grain Boundary and Hybrid SNS Junctions Based on Ba-122 Thin Films. *IEEE Trans. Appl. Supercond.*, 23(3), 2013.
- [42] R. Sobota, T. Plecenik, M. Gregor, M. Truchly, L. Satrapinsky, M. Vidis, K. Se-cianska, **F. Kurth**, B. Holzapfel, K. Iida, P. Kus, and A. Plecenika. Surface prop-

- erties of Co-doped  $\text{BaFe}_2\text{As}_2$  thin films deposited on MgO with Fe buffer layer and  $\text{CaF}_2$  substrates. *Appl. Surf. Sci.*, 312:182–187, 2014.
- [43] T. Thersleff, K. Iida, S. Haindl, M. Kieszun, D. Pohl, A. Hartmann, **F. Kurth**, J. Hänisch, R. Hühne, B. Rellinghaus, L. Schultz, and B. Holzapfel. Coherent interfacial bonding on the FeAs tetrahedron in Fe/Ba( $\text{Fe}_{1-x}\text{Co}_x$ ) $_2\text{As}_2$  bilayers. *Appl. Phys. Lett.*, 97(2), 2010.
- [44] S. Trommler, J. Hänisch, K. Iida, **F. Kurth**, L. Schultz, B. Holzapfel, and R. Hühne. Investigation of the strain-sensitive superconducting transition of  $\text{BaFe}_{1.8}\text{Co}_{0.2}\text{As}_2$  thin films utilizing piezoelectric substrates. *Journal of Physics: Conference Series*, 507(1):012049, 2014.
- [45] G. A. Ummarino, S. Galasso, P. Pecchio, D. Daghero, R. S. Gonnelli, **F. Kurth**, K. Iida, and B. Holzapfel. Resistivity in  $\text{Ba}(\text{Fe}_{1-x}\text{Co}_x)_2\text{As}_2$ : Comparison of thin films and single crystals.



## Acknowledgments

This work has been conducted at the Leibniz Institute for Solid State and Materials Research Dresden (IFW Dresden) and would not have been possible without the support of many people and institutions.

Primal I would like to thank Prof. Dr. Ludwig Schultz for the possibility to realise this PhD thesis at the IFW Dresden. In addition to outstanding scientific support, I would like to emphasise the permanent backing and encouragement. In this regard, I got the possibility to travel to numerous conferences, schools, and countries to present results or enrich my experience by working in cooperation with leading scientists in my field.

I would also like to give great thanks to Prof. Dr. Paul Seidel, not only for the interest in my work and the willingness to give the second opinion to this thesis, but also for his incredibly impressive way of scientific working. I was enriched by a lot of discussions which have been about much more than scientific topics.

For unbelievably great support in all fields and for the great opportunity to work with him in his Japan-EU project "IRON-SEA", I would like to thank Prof. Dr. Kazumasa Iida. He is not only a brilliant scientific advisor, but also a great friend, with whom it is a great pleasure to work, travel (in first class), discuss, or end up in bars drinking. In this respect, he gave me a great welcome in his home country Japan to get to know the fascinating Japanese culture as well as the MBE chambers, and he introduced me to numerous bright scientists all over the world. His way of free teaching and handling my ups and downs during my time at the IFW has been outstanding and is hard putting into words.

A great thanks, I would like to give to Prof. Dr. Bernhard Holzapfel, for great scientific advice, the teaching scientific survey and the nice atmosphere he created working in his group.

Massive thanks Dr. Vadim Grinenko who helped me in numerous scientific problems and was a great office colleague, and friend over my whole time in the IFW Dresden. Discussions with him have always been immense fun, pleasure and thrill.

I wish to thank Dr. Ruben Hühne for the great support, the scientific discussions, and the nice atmosphere we had in our Thursday discussions. Whatever problem occurred, I could ask Ruben and he tried to solve it.

For the warm welcome in Japan and the enormous support in all fields, I would like to thank Prof. Dr. Hiroshi Ikuta who took care of every little problem I was bothered with. It was very impressive and a great honour for me to get the opportunity to work in his group and to experience the Japanese culture. In this tenor, I would like to thank my

other Japanese colleagues Dr. Takahiko Kawaguchi, Dr. Takafumi Hatano, Naoki Sumiya, Yasuhiro Mori, and Masashi Chihara who easily invited me to work, having sushi, drinking in bars, and who unsuccessfully tried to teach me Japanese.

My colleagues Dr. Chiara Tarantini and Dr. Jan Jaroszynski on the other side of the world in Tallahassee, Florida, USA, whose helping support made it possible to measure in the high magnetic field laboratory using the strongest available dc magnets, deserve a great thank. Especially the work with Chiara in its effectiveness and brilliance has been an enriching pleasure for me.

I am also very grateful to my collaborators from all over the world who contributed to this work, namely, Stefan Schmidt, Dr. Sebastian Döring, Dr. Paola Pecchio, Dr. Dario Daghero, Prof. Dr. Renato Gonnelli, Dr. Ataru Ichinose, and Dr. Ichiro Tsukada.

The experiments in this work would not have been possible without the helping hands of plentiful colleagues at the IFW Dresden. In this context, I would like to thank my colleagues Dr. Sebastian Fähler, Dr. Jan Engelmann, Dr. Elke Reich, Dr. Jens Hänisch, Feifei Yuan, Stefan Richter, Dr. Sascha Trommler, Patrick Pahlke, Marco Langer, Juliane Scheiter, Svea Fleischer, Michael Kühnel, and Ulrike Besold who attributed not only in a scientific way but also in a nice atmosphere, a lot of coffee, barbecue events, and soccer matches.

I would like to give big thanks to my office colleagues Diana Pohl, Dr. Veronika Hähnel and Dr. Vadim Grinenko for the nice time and atmosphere, the relaxing talks together with countless shared coffee cups (or tea in Vadim's case), cakes, cookies, and fruit baskets.

For the financial support, I thank the European Union's Seventh Framework Programme (FP7/2007-2013) under the project IRON-SEA (Agreement No. 283141).

Last but not least, I thank my friends, in particular Julia Hebecker who did proof reading of this work, and my family for all the support and the uncounted and priceless shared time I experienced over the years.

# Erklärung

Hiermit versichere ich, dass ich die vorliegende Arbeit ohne unzulässige Hilfe Dritter und ohne Benutzung anderer als der angegebenen Hilfsmittel angefertigt habe. Die aus fremden Quellen direkt oder indirekt übernommenen Gedanken sind als solche kenntlich gemacht. Die Arbeit wurde bisher weder im Inland noch im Ausland in gleicher oder ähnlicher Form einer anderen Prüfungsbehörde vorgelegt.

Die vorliegende Dissertation wurde am Institut für Festkörperphysik und Werkstoffforschung unter der wissenschaftlichen Betreuung von Prof. Dr. Ludwig Schultz angefertigt.

Es haben keine früheren erfolglosen Promotionsverfahren stattgefunden.

Ich erkenne die Promotionsordnung der Fakultät Mathematik und Naturwissenschaften an der Technischen Universität Dresden vom 23.02.2011 an.

Dresden, den 13.07.2015

Fritz Kurth, Diplom-Physiker